LBL-5129
c.1

THE STRUCTURE AND ELECTRICAL PROPERTIES OF GLASSY CARBON

Ram Raghuvir Saxena
(Ph. D. thesis)

June 19, 1976

Prepared for the U. S. Energy Research and
Development Administration under Contract W-7405-ENG-48

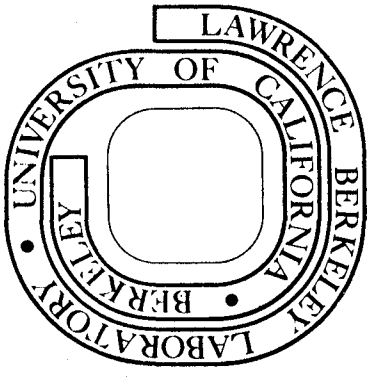

LBL-5129
c.1

DISCLAIMER

THE STRUCTURE AND ELECTRICAL PROPERTIES OF GLASSY CARBON

Ram Raghuvir Saxena

ABSTRACT

The structure and electrical properties of Glassy Carbon (GC) have been studied using various techniques. Glassy Carbon samples were heat treated in a graphite furnace at temperatures in the range 1000-2800^{o}C for different time intervals in order to produce structural changes.

Scanning electron microscope studies indicate that the GC used in this work is comparable to the best material produced and is thus a good representation of hard carbons. Comparison of the K-Emission bands of graphite, diamond and GC heat treated at different temperatures shows that the experimental observations are best explained in terms of a structure model of GC, which consists of both trigonally and tetrahedrally bonded C atoms; the tetrahedrally bonded C content reducing with heat treatment temperature. Single crystal patterns are seen in transmission electron microscope studies, and a new explanation is proposed to account for these observations. It is proposed that bulk GC does not contain micron size single crystals and that these come about in the process of specimen preparation as built-in stresses are relieved.

X-ray techniques have been used to characterize the structure of GC. The interlayer spacing d_{002} is reduced only to 3.40A^{o} (compared to 3.35A^{o} for graphite) for GC heat treated at 2800^{o}C for two hours (GC 2800-2), confirming the "hard to graphitize" nature of GC. The

crystallite size parameters L_c, L_a, perpendicular and parallel to graphitic layers respectively, grow only to 28 and 50A^{o} respectively for GC 2800-2. Based upon the heat treatment variation of d_{002}, L_c and L_a of the isochronally heat treated specimens for two hours each, three different regions of temperature are found. It is suggested that the first region is over when dehydrogenation is completed. The second region is characterized by a constant d_{002}, and the increase in L_c, L_a in this region may be due to stress relief. The kinetics of change in the third region can be analyzed using the "superposition method" to give an activation energy of 200-225 ($\pm$ 30) K cal/mole.

The electrical properties studied extensively in this work are conductivity, σ, and magnetoresistance, $\frac{\Delta\rho}{\rho}$. The temperature dependence of σ is explained as a sum of a temperature independent contribution due to a boundary scattering mechanism, and a contribution due to the hopping conduction among localized states varying as $A.\exp(-B/T^{1/4})$. For GC isochronally heat treated at HTT < 2000^{o}C an anamolous contribution to σ is found. This drop in conductivity at low temperatures becomes more pronounced for lower HTT material. It is suggested that this may be due to the lath like structure of lower HTT material. The magnitude of negative $\frac{\Delta\rho}{\rho}$ increases with H and as T is reduced. For HTT > 2000^{o}C the negative $\frac{\Delta\rho}{\rho}$ is found to follow a $f(H/T^{1/2})$ functional dependence. For HTT < 2000^{o}C the behavior of $\frac{\Delta\rho}{\rho}$ becomes more complex, although the general features remain the same. An energy band model is proposed to explain the observed electrical properties, which consists of a

pseudo-gap (with mobility shoulders) arising from localization of states due to disorder. The fermi level is pinned down near the top of the extended states inside the valence band due to localized states in the inhomogeneous part of the structure.

ACKNOWLEDGEMENTS

The author wishes to express his sincere appreciation to Professor R. H. Bragg for introducing the author to the fascinating fields of carbons, for suggesting this problem, and for his valuable guidance and stimulating discussions that the author had with him from time to time. The author also wishes to thank Professor L. M. Falicov for helpful discussions regarding interpretation of data; Professors J. Washburn and S. Wang for serving on the Thesis Committee; Mr. Tom Mowles for his invaluable service in setting up th low temperature facility; Members of MMRD support staff, Mr. Julien Patenaude, Mr. Duane Newhart, Mr. Jack Wodei, and Mr. Jim Severens for their technical assistance; Mrs. Lois Fernander for typing the thesis; Mrs. Gloria Pelatowski for drawing the figures; the Energy and Research Development Agency for the financial support; and all my friends at Building 62 for the congenial atmosphere.

The author gratefully acknowledges continued support and encouragement from his parents, sisters and brothers; inspiration and advice from a dear friend, Arvind; and patience and encouragement from my wife, Uma, during the most crucial stages of this work.

TABLE OF CONTENTS

I. INTRODUCTION

Carbon, in its elemental or allotropic and manufactured or fabricated forms, aside from its use as fuel, plays a very important part in our everyday existence. Its value in industry may be better realized through the fact that carbon and its related products are produced annually in the United States to the value of billions of dollars. As diamond, it is the hardest material known to man, whereas in the graphite form it is one of the softest materials available naturally. No other material can substitute for graphite electrodes used in numerous industries (including steel and aluminum). The favorable high temperature properties have led to the use of various carbon materials (natural and synthetic, which are graphite-like in structure) in the aerospace industry. Carbon black is indispensible in printing processes, in the rubber trade and as a pigment. Activated carbon is used as a catalyst in many chemical processes.

Although carbon materials have been in use for a long period of time, their properties were not well understood, and the industry itself was considered a "black art." In the last few decades considerable progress has been made toward understanding the properties of carbon materials. Thorough characterization in the industry coupled with basic research at academic institutions has demystified "carbon materials" to a large extent. Although many aspects are still not understood, the structure of various forms of carbon and their gross physical and chemical properties are quite clear. Based upon their response to heat treatment, carbon materials are classified into two categories - soft

carbons and hard carbons. Soft carbons are those which develop a graphitic structure or graphitize. Hard carbons retain a disordered form of graphite-like structure upto the heat treatment temperature ca. 3200^{o}C.

Glassy carbon (GC) is a hard carbon discovered about fifteen years ago. Its availability in bulk form (as opposed to powder) has made it possible to study seriously the physical properties of hard carbons. Whereas it has already found use in many applications, the properties are still not completely understood. The structure continues to be a matter of debate and considerably more work is needed to delineate its properties.

In this work various techniques have been used to study the structure of glassy carbon. Various structural parameters have been used to characterize the material and the effect of heat treatment has been investigated. The electronic properties (primarily conductivity, σ, and magnetoresistance $\frac{\Delta\rho}{\rho}$) have been studied with two goals in mind. (i) to characterize the material and how it is affected by heat treatment, and (ii) to understand the properties on a first principle basis. Like the amorphous forms of (two later members of the same group in the periodic table of elements) Si and Ge, glassy carbon is a model material to study electronic properties of disordered systems.

Chapter II provides a summary of the published literature relevant to this study. Initial scanning electron microscope work is described in Chapter III. Chapter IV describes the heat treatment procedures used. Transmission electron microscope studies to understand the structure of GC are discussed in Chapter V. Chapter VI discusses the bonding in GC

in terms of the observed K-emission bands from graphite, diamond and GC. The x-ray characterization of GC is the subject of Chapter VII. The kinetics of change in GC, in terms of x-ray structure parameters, is also discussed in this chapter. Chapter VIII gives the description of low temperature apparatus (including a superconducting magnet) used for measuring the electrical properties and the measurement procedures are detailed in Chapter IX.

Chapter X constitutes the main thrust of this work. The electrical properties σ and $\frac{\Delta\rho}{\rho}$ are used to characterize GC, and correlations are made with x-ray observations discussed in Chapter VII. The temperature dependence of σ, and the magnetic field and temperature dependence of $\frac{\Delta\rho}{\rho}$ are analyzed in detail and attempts are made to understand the properties on a first principle basis. Recommendations for future work are also made in this chapter. Chapter XI summarizes the results of this study of the properties of GC.

CHAPTER II

Literature Review

II. 1 Structure of Carbons

II. 1.1. Crystalline Forms: The structure of the various forms of carbon has been reviewed in great detail by Fischbach[1], Ergun[2] and Ruland.[3] A brief account of the important aspects is presented here.

The two well-known crystalline forms of carbon are diamond and graphite. Graphite is the thermodynamically stable form of carbon at ordinary pressures. It has a layered structure, and within each layer each carbon atom is covalently bonded to three other atoms forming a hexagonal network. The $2s^2 2p^2$ electrons in each carbon atom are considered to undergo sp^2 hybridisation producing 3 planar orbitals which are covalently bonded in "σ bonds," with an interatomic distance of 1.415 A^{o}. The fourth remaining electron has a p_z wave function with lobes perpendicular to the layer. This is called a π electron. These π electrons are responsible for the weak bonding between the layers and give rise to the extreme anisotropy in the physical properties of graphite.

The structure of hexagonal graphite is shown in Fig. II. 1. The hexagonal layers are arranged in an ABAB stacking. ABCABC stacking gives rise to metastable rhombohedral graphite as shown in Fig. II.2. Rhombohedral graphite has never been isolated but extreme mechanical treatment, e.g grinding of hexagonal graphite can produce up to 33% rhombohedral graphite by changing the stacking sequence. Pauling[4] has proposed a quinoidal structure for the layers of hexagonal graphite

which consists of alternating single and double bonds as shown in Fig. II. 3. This causes only small changes in bond lengths and angles so that the effect on x-ray diffraction patterns is subtle.[7] Its effect on electronic band structure is not clear.[7]

In the diamond form each carbon atom has four sp^3 hybridised electron orbitals. These are tetragonally bonded to give rise to a three dimensional network as shown in Fig. II. 4. The interatomic distance is 1.544Å, thus the bonds are slightly weaker than the C-C bonds in the graphite layer. The specific gravity of diamond is 3.52 g/cm^3 compared to 2.27 g/cm^3 of graphite. Thus diamond is the stable form at high pressures. Another form of diamond known as hexagonal diamond was first proposed by Ergun and Alexander.[5] This was subsequently found in Canyon Diablo and Goalpara meteorites and can be synthesized at high pressures. This variant has a Wurtzite (Zns) structure with C atoms at all positions as shown in Fig. II. 5. This is also called Lonsdalite - after the distinguished crystallographer Lonsdale.

Chaoite and Carbon VI are among the more recently discovered[6] allotropic forms. These have large unit cells and diamond like properties. These are apparently metastable forms at low pressures and high temperatures.[7]

II. 1.2. Synthetic Carbons: Most of the artificial carbons used industrially are not regarded as being crystalline. On heat treating at high temperatures they tend to develop a graphitic structure. This process called "graphitization" has been reviewed in detail by

Fischbach[1] and Pacault[8] and will be discussed in a later chapter. The graphitization behavior of these carbons is decided early in the history of carbon processing when their basic structure is determined. The x-ray diffraction pattern of these carbons show broad symmetrical (00l) type peaks arising from parallel layer stacking and asymmetric (hk) bands from internal layer disorder and faults in the stacking sequence. These carbons are divided into two broad groups. Those carbons which develop a three dimensional graphitic structure are called "soft carbons" or "graphitizing carbons". The other class of carbons do not exhibit any evidence of a three dimensional graphitic structure up to the highest heat treatment temperature (ca. 3200^{o}C). There are no traces of (hkl) ($l \neq 0$) lines in their x-ray patterns. These are called "hard carbons" or "non-graphitizing carbons".

Warren's turbostractic model[9] has been used extensively to describe the structure of soft carbons. In this model the layers have nearly perfect graphite layer structures, but there is little registry in the stacking of these layers. The structure is characterized mainly by the mean interlayer spacing, c, determined from the (00l) peaks. The increase in c, compared to the graphite interlayer spacing, is attributed to layer disorder. The other parameters used to characterize the structure are L_a, the mean diameter and L_e, the mean height of parallel layer stacks. These are determined from the widths of appropriate x-ray diffraction peaks. When the graphitization has gone far enough to justify speaking of crystallites - L_a, L_c become crystallite parameters.

II. 1.3. Glassy Carbons: In the last decade or so it has been possible to carefully decompose cross-linked polymers to obtain what have been called "glassy", "glass-like" or "vitreous" carbons.[10] The nonmenclature comes from a shiny black glass appearance and a glass-like (concoidal) fracture of these carbons. The typical properties of glassy carbon (GC) as compared to graphite are listed in Table II.1. The distinguishing properties of GC are high strength, low density, high hardness, and resistance to corrosion and oxidation. It was seriously considered as the nose cone material for re-entry vehicles. Recently it has found considerable use as a bio-material. Its compatibility with human bone has led to its use in dental implants. With its corrosion resistance it makes an excellent heart valve. Many crucible container forms are now commercially available. Depending upon the original polymer composition (phenol-formaldehyde resin and poly-furfural alcohol being the most common) and processing variables a wide range of properties have been reported for these glassy carbons.[11]

The structure of glassy carbon has been studied using a variety of techniques, but the structure is not well understood. High resolution electron microscopy studies[12] have shown that GC has an entangled thin lath-like structure and "Jenkins Nightmare" (Fig. II.6) was proposed as a model.

The bonding in GC has been a subject of considerable debate. Ergun and Tiensuu[13] showed that clusters of tetrahedrally bonded carbon atoms give rise to diffraction peaks in the same region where (10) and (11) reflections of the graphite-like structure occur. Noda and Inagaki[14]

have interpreted their radial distribution data in terms of a model that consists of both trigonally and tetrahedrally bonded carbon atoms. Furukawa[15] has suggested that GC has tetrahedrally, triple and double bonded C atoms. Kakinoki[16] has added an oxygen bridge to Noda and Inagaki's trigonally and tetrahedrally bonded C atoms. Laser raman spectroscopy studies[17-18] have not given any conclusive evidence either. Later we shall discuss our attempt to understand bonding in GC using K-emission bands.

Transmission electron microscopic studies have not been to successful in understanding the structure of GC. Whittaker[19] has found evidence for various allotropic forms of carbon in GC. Our work in this area is in agreement with his results, but our interpretation differs from his. Whereas Whittaker has suggested that large single crystals of various forms of carbon exist in GC, we believe that the sample preparation process has a large part to play, as will be described later.

Parameters c, L_a, L_c as derived from x-ray diffraction patterns have been used quite extensively to characterize GC. These parameters are found to change with HTT, showing quite clearly that some ordering and crystallite growth does take place. In the absence of a model it is difficult to assign meanings to these parameters. It is common to call c - the mean interlayer distance and L_a, L_c mean defect free distances parallel and perpendicular to the layers respectively.

Glassy carbon has a large volume (about 40%) of voids which account for the reduced density. These voids are not connected, because glassy carbon has very low permeability to gases. They are an important part of the structure and have already been shown to affect the properties of GC.[11]

These voids have been reported to be spherical, ellipsoid of revolution and needle-like by different workers. The void growth with HTT has been shown in the work of Bragg[20], Biswal and Bragg[21] and others.[22]

II. 2. Electronic Properties of Carbons: Whereas extensive review articles have been published on the electronic properties of single crystal graphite[23] and graphitizing carbons[24], comparatively little work has been done on non-graphitizing carbons. The electronic properties are relatively well-understood for near single crystal graphites, but even for soft carbons the understanding is far from complete. In the case of hard carbons there are contradictions in the literature regarding the trends of the experimental data. We begin with a summary of electronic band structure calculations for single crystal graphite.

For two dimensional single graphite layer in the tight binding scheme, the wave function is made up of a linear combination of sp^2 hydridised orbitals and is of the σ type, while a linear combination of $2p_z$ orbitals yields a wave function of the π type. With this rigorous classification $\sigma - \pi$ mixing can be excluded. By treating σ and π bands independently it is found that occupied and unoccupied π bands are found to be degenerate in energy at the six Brillonin zones corners and in the vicinity of the corners the energy is a linear function of wave vector measured from a zone corner. In the tight binding scheme there is no overlap of π bands. The estimated spin-orbit interaction splitting of the degeneracy of the π bands is less than 10^{-4} eV.

For three dimensional hexagonal graphite the π bands remain the main features of the band structure, but now the considerations of $\sigma - \pi$ mixing

and other neighbour interactions become important. This results in the overlap of the two π bands and the existence of electron and hole pockets around E_f at the Brillonin zone edges. The Slonczewski-Weiss model is now well accepted and a consistent value of the parameters of this model is available to explain most of the observed properties.[23] The electronic properties along c-axis are still not understood. The calculated mobilities of carriers are too small to be valid, and it has been suggested that localization may take place along the c-direction.[23]

The electrical properties of soft carbons have been studied in considerable detail. Although elegant solutions and explanations have not always been possible, the work of Mrozowski[26] and others following him has been thorough. The temperature dependence of conductivity was studied in great detail by Mrozowski[26]. The most important result was that - "In contrast with the infinite single crystal, systems of benzene rings of finite dimensions possess a finite energy gap between the filled and the conduction bands, the energy gap steadily decreasing with molecular size - from about 1 eV for molecules several benzene rings wide to 0.2-0.3 eV for systems 30-40A° in diameter and to .05 eV for graphite crystallites with diameters of the order 1000A°." This in conjunction with reasonable hypotheses regarding excess carriers and scattering from crystallite boundaries can be considered to have explained $\sigma(T)$ in soft carbons.

Although all three, σ, R_H and $\frac{\Delta\rho}{\rho}$, have been used to characterize carbons, the understanding of R_H and $\frac{\Delta\rho}{\rho}$ is far from complete. Delhaes has written an excellent review article on the subject[27] and has investigated $\frac{\Delta\rho}{\rho}$ in soft carbons quite thoroughly.[28] A qualitative understand-

ing of R_H is possible and is usually presented in terms of the variations of E_F with HTT in a proposed band structure. For soft carbons $\frac{\Delta\rho}{\rho}$ is found to be both positive and negative. The explanation is as yet not satisfactory, although Delhaes has tried to employ all the available models to explain his data.

Only a few studies[29-31] of electronic properties of GC have been reported. The only two prior studies[29-30] of $\frac{\Delta\rho}{\rho}$ do not agree on the sign of $\frac{\Delta\rho}{\rho}$ over the range of HTT and ambient temperatures. No explanation of the magnetic field dependence of $\frac{\Delta\rho}{\rho}$ was offered in the one reported study.[31] The conductivity and Hall Effect have not been carefully investigated either. A recent ESR[32] study of GC over a range of HTT has shown that both localized and extended electron states of comparable density exist at all HTT's studied.

Some of the problems of interpretation come from a lack of theoretical understanding of electronic properties in this rather complex field. We next review some of the concepts to be used throughout this work.

II. 3. Electronic Properties of Non-Crystalline Materials:

It was first emphasized by Ioffe and Regel[33] that if the mean free path, L, of the carriers is such that L ca. a, the lattice parameter - then normal conduction is no longer possible. Their conclusions were:

(1) "The band structure has a wider basis than the periodicity of the crystal lattice." - in explaining the observed behavior of electronic properties of amorphous semiconductors.

(2) Instead of the free motion of electrons followed by scattering due to an instantaneous process of impact - sometimes the

mechanism of transfer comes closer to a series of individual jumps.

(3) "The short range order characterizing chemical forces of interaction between atoms has a decisive significance for the determination of the properties of semiconductors."

Since then, the considerable effort on the part of a large number of researchers has resulted in providing a plausible theoretical basis to these conclusions. A new set of mathematical tools, however, have not been invented and our understanding is limited by the fact that we are trying to apply techniques developed for periodic crystals. The accepted concepts in the study of non-crystalline materials are as follows:

(1) The density of states is a valid concept for non-crystalline as well as for crystalline materials and can, in principle, be determined experimentally, e.g., by photoemission investigations.

(2) Under certain conditions of disorder (random positions and/or random potentials) the electron wave function is localized.

It is possible then for an amorphous material to have a continuous density of states, although for some energy ranges the electron states are localized, so that an energy E_c can exist which has localized states on one side and extended states on the other side. The conduction among these localized states is by thermally activated hopping. Mott[34] also believes that at $0^{o}K$ there should be a discontinuity in the mobility at E_c - leading to the concept of the mobility shoulder. The basis is Anderson's paper on the "Absence of Diffusion in Certain Random Lattices." Based upon these concepts the schematic density of states for non-crystalline systems is shown in Fig. II.7.

The hopping conduction mechanism is a thermally activated process of an electron jumping from one center to another. In each jump a phonon is either emitted or absorbed. Processes in which a phonon is absorbed are rate controlling giving a conductivity of the form $\sigma = \sigma_o e^{-\varepsilon/kT}$. At low temperatures Mott predicts that hopping to farther than the nearest neighbour is possible and $\ln\sigma$ is linear with $1/T^{1/4}$. Whereas a $1/T^{1/4}$ law has been found to be true in many experiments, other dependences of $1/T^{1/n}$ form have been proposed, and it is often possible to fit the data to more than one of these dependences.[35]

For hopping conduction there is no generally accepted theory for the Hall Effect. The analysis of Hall Effect data is commonly done by using the simple expression $R_H = \frac{1}{n.e}$. The experimental evidence suggests:[34]

(1) The Hall mobility in semiconductors is one or two order of magnitude less than the conductivity mobility.

(2) The Hall Effect has often the same sign as for electrons, even if the current is carried by holes in a valence band.

(3) When the current is carried by electrons at E_F, R_H is sometimes greater than $\frac{1}{n.e}$.

(4) The activation energy for the Hall mobility is less than that for theconductivity mobility; in fact it can in some cases approach zero.

The magnetoresistance is often found to be negative in non-crystalline materials. The explanation is still not clear, although many models have been proposed.[28] It has been shown that the Boltzman Transport Eqn. can never give negative $\frac{\Delta\rho}{\rho}$.[36] Starting with $\sigma = n.e.\mu$ the

proposed mechanisms call for an increase in n and/or μ under the influence of a magnetic field. Delhaes[28] has given an excellent summary of the proposed models. Unfortunately, no model has been put forth to explain $\frac{\Delta\rho}{\rho}$ for the case of hopping conduction. Most models use extended states alone or extended and localized states together. Mott[34] has suggested that a localized state could create order in the surrounding spins - thus creating a self trap that increases the hopping activation energy by $\Delta\varepsilon$. A magnetic field would destroy this order, giving rise to negative $\frac{\Delta\rho}{\rho}$. Neither the details of the mechanism nor any magnetic field or measurement temperature dependence have been suggested.

For extended state, Fujitas' model[32], when mean free path is limited by boundary scattering, explains the sign and gives $\frac{\Delta\rho}{\rho} \propto H^2$ in first order. Toyozawa's[38] model calls for spin dependent scattering of extended states from localized states, giving $\frac{\Delta\rho}{\rho} \rightarrow$ const. for $H \rightarrow \infty$, and a Brillonin function dependence $(\frac{\Delta\rho}{\rho}) = - f(\frac{H}{T + \theta})$ for low H values. Toyozawa's model has been used extensively, being the only model worked out in detail. It has been tried even in cases when it was not clear that the basic tenets of the theory were in agreement with the experimental set-up. With adjustable parameters it has been possible to find a reasonable fit to the equations of this model. The problem has been the need to assume large values for the local moments, often many times larger than the Bohr magneton.[39] Other experiments such as magnetic susceptibility measurements have not confirmed the validity of these large assumed moments. However, the combined (H,T) dependence of $\frac{\Delta\rho}{\rho}$ may have a "not-yet-understood" basis which might account for the

possibility of fitting the observed data to Toyozawa's equation. Delhaes[28] has suggested a dependence $\frac{\Delta\rho}{\rho}$ vs $f(\frac{\lambda H}{T})$ with λ as an adjustable parameter and was able to successfully fit all of his data for one soft carbon at various temperatures (λ-function of the measurement temperature) to one single curve.

CHAPTER III

Material Selection - SEM Studies

Glassy Carbon (GC) samples were obtained from four different sources for initial studies. These are named here according to the source from which they were obtained; Tokai GC, Beckwith GC, Lockheed GC, and Poly Carbon GC. These samples were examined with a scanning electron microscope to decide which GC should be purchased for extensive studies. Typical fracture surfaces for these four kinds of GC are shown in Figures III.1, III.2, III.3 and III.4.* It is clearly seen that Beckwith GC has many large voids, whereas the other three GC exhibit a featureless surface characteristic of these hard carbons. From the available data on the physical properties of these GC specimens, Beckwith GC had poorer mechanical properties, and the other three were comparable.

Based upon the SEM study, bulk GC in plate form of size 8" x 2" x 1/16" was bought from Poly Carbon. Most of the GC was heat treated at 1000^{o}C for one hour. Two plates each of GC heat treated at 1800^{o}C and 2800^{o}C for one hour were also obtained. These were used for the transmission electron microscopic and K-emission studies described in Chapter V and VI. For the x-ray work and electrical properties measurement samples were heat treated as described in Chapter IV.

*These pictures were taken by Mr. Tom Mowles.

CHAPTER IV

Heat Treatment of Glassy Carbon Samples

IV. 1. Description

The heat treatments of Glassy Carbon (GC) samples were carried out in a graphite furnace. The schematic diagram of the furnace is shown in Fig. IV.1. This furnace was water-cooled and Ar gas was used to maintain an inert atmosphere. The space between the graphite heating element and the furnace walls was filled with insulating carbon black powder. The furnace was powered by a power supply of 20KVA rating, with provisions for six different "taps" saturating at increasing current levels. The GC samples were placed in a cylindrical graphite crucible 3" dia. x 2 1/2" size and surrounded with GC wool. This crucible was placed in the center of the hot zone by resting it on a PG disc. This PG disc was screwed onto a graphite rod which also supported insulating PG discs, and the whole assembly was screwed to the bottom of the furnace. For proper insulation these discs had carbon felt sewn with carbon fiber in a ring-form around them so that they touched the graphite element at all times. Similarly, insulation at the top was provided with insulating discs mounted on a hollow graphite rod. The top assembly is shown in Fig. IV. 2.

An optical pyrometer calibrated for the temperature range 1000°C - 3000°C was used to measure the temperature. Above 2000°C the precision was $\pm$ 20°C. The crucible top had a hole of size 3/16" diameter. Thus the crucible acted like a radiating black body. This radiation passed through the hollow graphite tube and quartz plate and was reflected from

the prism at the top to be observed by the pyrometer. Plate A could be pulled out to measure the temperature. This arrangement is also shown in Figure IV. 2. For a hole of length to diameter ratio of 4 in a material of emissivity 0.5, the effective emissivity of the bottom of the hole is 0.988.[40] Since the effective emissivity of graphite is greater than 0.5 between 0.65 - 0.6μ,[41] our experimental arrangement is an excellent approximation to a black body. The correction for shift in temperature due to the quartz plate was determined by placing another identical plate in the path of the observed ray.

For automatic temperature control, a hollow graphite tube was sealed on to the center of the furnace element with graphite cement (Fig. IV. 1). The top was covered with a glass disc and a cap screwed on to make it air tight. A rayo-tube heat-eye was placed in front of the hole and the signal generated was fed back to the power supply unit. The power supply unit was equipped with a strip chart recorder. The pen recorded heat-eye signal on a non-linear temperature scale. For automatic temperature control, a knob was available to set the desired temperature. This unit was calibrated for each desired temperature with the optical pyrometer. The temperature was maintained within $\pm$ 20°C with this feedback unit.

IV.2. Experimental Procedures: GC pieces (1/16" thick) cut in rectangular shapes (2" x 1") were placed in the crucible surrounded by GC wool. The crucible was lowered into the furnace using a long specially made clip (Fig. IV. 2) and placed on top of the PG disc of the bottom insulation assembly. The insulating assembly was screwed on at the top. For initial preparation the furnace was left with Ar gas flow of 5 ft^3/hr

for 10 minutes. Afterwards the gas flow was reduced to 1 ft^3/hr, and water flow at 2.0 gallons/min. was maintained. (the furnace had interlocks to shut itself off in case either of these flows were not maintained). Timer in-bypass switch was put at bypass. The proper heating rate was experimentally determined because high heating rates lead to cracks in GC samples. These are probably due to the evolution of gases trapped inside. The power-time relationship found suitable is given in Table IV. 1. This schedule did not give cracks upto the highest temperatures. For automatic temperature control at the desired temperature, the set point was calibrated using the optical pyrometer. The current was switched from manual to automatic and the timer IN-Bypass switch was changed to IN position after the timer had been started. After the lapse of the time set on the timer the power supply shut itself off and the furnace was allowed to cool for at least one hour with gas and water flow on before removing the specimens.

CHAPTER V

Transmission Electron Microscope Studies

V. 1. Sample Preparation: To prepare the samples small pieces of GC were crushed between two clean glass slides. Carbon film was evaporated on top of the glassy carbon dust or flakes on both the glass slides. The film was floated off the glass slides in distilled water, and samples were collected on 100-mesh grids. These were studied in a Siemens Elmsikop Microscope using selected area diffraction (SAD), bright field (BF) and dark field (DF) techniques. Polycrystalline gold SAD ring patterns were photographed to obtain the camera constant, and this value was used to calculate the d-spacings. GC 1000-1, GC 1800-1 and GC 2800-1 samples were studied in this work.

V. 2. Results: Based upon the SAD patterns, our results can be grouped in four categories. (i) Diffuse ring patterns, (ii) Spotty ring patterns, (iii) Single crystal patterns, and (iv) Double crystal patterns. Since each grid contained many small pieces of materials, which could separately be classed as samples, it was easy enough to find any of the four kinds of SAD patterns, for a few samples on each grid.

Diffuse ring patterns, characteristic of amorphous materials, were seen for all the three grades of GC studied. A representative example is shown in Fig. V.1 which shows SAD pattern for GC 2800-1. The d_{002} spacing is found to change from 3.65Å for GC 1000-1 to 3.44Å for GC 2800-1 in qualitative agreement with x-ray diffraction studies. The BF picture corresponding to Fig. V.1 is shown in Fig. V.2. Corresponding DF picture, taken with an aperture over the first ring of the

SAD pattern is shown in Fig. V.3. Fig. V.4 shows the typical BF picture for a GC 1800-1 sample. The tangled nature of the microstructure is quite clearly seen in these pictures.

An example of a spotty ring SAD pattern and the corresponding BF picture is shown in Fig. V.5 and Fig. V.6. The microstructure is difficult to pinpoint, but it bears more resemblance to the first group microstructure than the single crystal ones.

Single crystal patterns were seen with about the same frequency as reported by Whittaker and Tooper[19] in approximately ten percent of samples. These were always (001) patterns of a graphitic structure. No attempt was made to study minute changes in lattice parameters to determine whether or not various allotropic forms of carbon were seen in our work. An example of single crystal SAD pattern and the corresponding BF picture is shown in Fig. V.7 and V.8. The previous tangled microstructure has disappeared. Double crystal patterns were seen quite often corresponding to single crystals rotated with respect to each other. A double pattern and the corresponding BF picture are shown in Fig. V.9 and V.10. The faulted nature of the material is quite clearly seen and some boundaries are also apparent. In our studies, many angles of rotation were seen for double crystal patterns and no special significance can be attached to the angle of rotation as done by Whittaker and Tooper.[19] In one case a SAD pattern corresponding to many crystals slightly rotated with respect to each other with the possibility of the presence of various allotropic forms of carbon was seen. This is shown in Fig. V.11. The BF picture is shown in Fig. V.12. Regular Moire' patterns are clearly seen in Fig. V.12.

V. 3. Discussion: Although our results are quite similar to those of Whittaker and Tooper[19], we do not believe that micron size crystallites of graphite and various allotropic forms of carbon exist in bulk GC for the following reason. If micron size single crystals do exist in bulk GC-1000-1, then after heat treating at 2800°C for two hours these GC plates should have graphitized which was not observed. That such "seeding" does indeed take place is confirmed in the unpublished work of Bradshaw et al., who while attempting to modify the thermal conductivity of GC by the addition of powdered micron-sized graphite in the early stages of GC processing, found that after heat treatment at around 2600°C the material completely turned to graphite.[80]

In the author's opinion, the explanation for these observed single crystal patterns is to be found in the sample preparation procedure. Whittaker and Tooper[19] have used a procedure similar to ours. We believe that during sample preparation built-in strains are released. The straightening of stressed graphite layers always give rise to c-axis patterns in electron microscope investigations. This is inherent in the sample preparation procedure, because these straightened layers will always be parallel to the glass slides. The other possibility that crystallization took place due to the intense heating in the electron beam is discarded because the spot patterns were seen as soon as a particle was brought in the center of the electron beam.

The proposed explanation might be thought to be inconsistent with Jenkin's type model (Fig. II.6) for the structure of GC. It should be pointed out that Jenkin's model is merely a convenience and is not in agreement with the observed behavior of all the properties of GC.

For example, in a graphitic lath-like structure (Jenkin's model) the oxidation behavior (rate) of GC is expected to be between the two extremes (known to be markedly different in pyrolytic graphite) of that of the $\bar{a}$ and $\bar{c}$ direction oxidation behavior of the graphite structure. The observed rate is close to the c-direction oxidation behavior of pyrolytic graphite pointing to the possibility of a skin-like structure for GC. That the proposed arrangements are possible at room temperature is supported by the fact that mechanical grinding alone can change hexagonal graphite into the rhombohedral form.

The evidence for the presence of built-in strain in GC comes from various sources. Ergun[42] has done extensive theoretical and experimental work on the strain broadening of x-ray diffraction profiles, and has concluded that the calculated values of L_c and L_a based on simple line broadening formulae which do not take account of lattice curvature or strain may be too small by as much as 80%. Fischbach[43] in his creep studies of GC has noted that as a result of shrinkage (approximately 40%) during pyrolysis, GC probably has high internal stresses which are relieved slightly with higher heat treatment temperatures (greater than 2000°C). Also in an unpublished work Fischbach and Jenkins attempted to intercalate GC with K in a gaseous atmosphere, and the material was reduced to dust. Their explanation was the presence of intense frozen stresses in GC which were abruptly relieved.[44]

Built-in stresses could also account for the brittle nature of GC. Although the mathematical problem of calculating the internal stresses resulting from volume shrinkage of an anistropic material during pyrolysis is formidable, the internal stresses must be very near

the fracture stress of the material, because at room temperatures the fracture stress rarely exceeds 20,000 psi. Furthermore, increase in heat treatment temperature dramatically increases the gas permeability, suggesting the rupturing of bonds via the locally anisotropic thermal expansion in adjacent regions and consequent opening of some closed porosity.

Chard[45] et al have studied pressure graphitization of GC. It was found that GC-1000 could be partially graphitized under pressure, whereas GC-3000 showed no evidence of graphitization. The results were interpreted in terms of a model proposed by Noda and Kato.[46] The proposed model conceives completion of dehydrogenation around 1500^{o}C. The explanation of Chard et al was that hydrogen bonded atoms can provide the necessary mobility of atoms so that GC-1000 can be partially graphitized under pressure. The observations are, however, consistent with stress relief in GC with increasing HTT. It is interesting to note that as in our TEM studies, Chard et al[45] observed lamellar structure in micron size areas.

Even if the proposed explanation is shown to be incorrect, the single crystal regions comprise only a small percentage of the total volume. In our x-ray studies (Ch. VII) no sharp peaks corresponding to polycrystalline graphite were seen superimposed on the broad peaks due to the disordered structure of GC. It is estimated from a comparison of the x-ray intensity profiles of GC and polycrystalline graphite that superimposed peaks would be seen if the volume percentage of polycrystalline graphite was more than 2%.

V.4. Conclusions: Although TEM is an excellent technique for studying nearby single crystals, it does not seem suitable for studying highly disordered materials. Our TEM studies confirm the disordered nature of GC, but little useful information can be extracted to characterize GC. The occurrence of single crystal patterns is thought to be due to stress relief during sample preparation. Thus in this instance the properties of bulk GC cannot be reliably correlated with results obtained using TEM. X-ray diffraction techniques are much better for our purposes and they were used to characterize the material as discussed in later chapter.

CHAPTER VI

K-Emission Studies of Glassy Carbon

VI. 1. Introduction: Although many models of the structure and bonding of carbon atoms in GC have been put forth, as reviewed in Chapter II, the bonding in GC is not well understood. K-emission was used to study the bonding character of glassy carbon. K-emission bands are observed when valence band electrons fall into empty K orbitals. The use of K-emission bands to study bonding character is well established.[47] Assuming equal probability of transitions from all parts of the valence band, Coulson and Taylor[48] compared their calculated density states N(E) with Chalkin's observed K-emission band of graphite. Since then many studies of the graphite K-emission band have been reported. MacFarlane[49] has confirmed Coulson and Taylor's prediction of polarizability of π and σ bands in K-band emission of graphite. Both Holliday[50] and MacFarlane analyzed their data as a sum of gaussian and non-gaussian pekas. Holliday concluded that the shift in peak wavelength from diamond to graphite is due to the difference in weights assigned to various gaussian components.

VI. 2. Experimental: Carbon K-emission bands were measured with a MAC 400S electron microprobe. Second order reflection from a Lead Octadeconate crystal (2d = 100.5 Å) was used to analyze the x-rays and the detector was a flow proportional counter using methane gas and a 1000 Å polypropylene window. A 15kV electron beam was used in our experiment. We measured K-emission bands from diamond, pyrolytic graphite (parallel mounted, i.e., with c-axis parallel to the electron

beam) and three samples of glassy carbon heat treated at 1000, 1800 and 2800°C for 1 hr. The data is presented in normalized form in Fig. VI.1. The shift in peak position from diamond to pyrolytic graphite is clearly seen in the figure. The trend for glassy carbon is that with higher heat treatment temperature the peak shifts toward the pyrolytic graphite peak.

VI. 3. Results and Discussion: To facilitate the comparison peak position, half width, index of asymmetry (defined after Ref. 50 as the ratio of part of the full width at half maximum lying to the long wavelength side of maximum ordinate to that lying on the short wavelength side) and the shift in peak position relative to pyrolytic graphite are given in Table VI.1. Holliday's data on diamond is also given in the table. The diamond data compares well with Holliday's data. Minor difference of the detail of the emission band may be due to the use of an LOD analyzing crystal in this work as compared to Holliday's use of a grating analyzer.

The peak wavelength of glassy carbon lies in between those of diamond and pyrolytic graphite. This suggests two possibilities: (i) that in glassy carbon the local bonding character around each carbon atom is intermediate to the two extremes or (ii) that glassy carbon contains both trigonal and tetrahedral C-C bonds. In view of the layered structure observed in high resolution electron microscopy[51] the first possibility is excluded. The shift in peak wavelength of glassy carbon toward the pyrolytic graphite peak with higher heat treatment temperature shows that the amount of tetrahedrally bonded

carbon reduces with increasing heat treatment temperature.

The half width of glassy carbon is larger than that of either diamond or pytolytic graphite and does not change with heat treatment temperature. This also supports the contention that glassy carbon has both diamond and graphite characteristics. The large half width is the result of higher weight assigned to the gaussian component corresponding to the diamond peak in the graphite K-emission band. This is better demonstrated in Fig. VI.2, which shows diamond, pyrolytic graphite and glassy carbon bands superimposed on each other. The index of asymmetry also approaches the pyrolytic graphite value with increasing heat treatment temperature. The part of full width at half maximum lying to the long wavelength side of maximum ordinate is approximately constant. This is further evidence that the change in the glassy carbon K-emission band with heat treatment temperature changes the index of asymmetry by reducing part of the half width lying to the short wavelength side of the maximum ordinate.

VI. 4. Conclusions: The conclusion of the in between bonding in GC is supported by laser raman spectroscopy studies[17, 18] and photo electron emission studies[56]. It seems clear that with heat treatment temperature GC approaches graphitic bonding - but until comparisons with all the other kinds of c-c bonds could be made there is a certain incompleteness in conclusions regarding bonding in GC. Some evidence for the thermodynamic stability of diamond like bonds in GC is available in the recent work of S. Das on the Thermodynamic Properties of Graphite-GC Equilibrium.[54]

CHAPTER VII

X-Ray Studies of Glassy Carbon

VII. 1. Introduction: Wide angle x-ray diffraction was used to characterize the structure of heat treated glassy carbon samples. The range of samples studied included isochronal heat treatments for two hours each at 1100°C and from 1300 to 2800°C in 100°C increments. To study the kinetics of structural changes in GC, samples were heated at 1700, 2000, 2300, 2500 and 2700°C for various time intervals. The nomenclature for these samples is henceforth GC-HTT-Time, e.g., GC-1500-2 means GC heated at 1500°C for two hours.

VII. 2. Experimental Procedures: The x-ray data were obtained on a GE XRD-3 diffractometer. A 1° beam slit, MR Soller slit and 0.1° receiving slits were used in our experiments. The combination was decided upon to obtain sufficient intensity, usually quite low for GC samples. Our experiments[52] with varying slit sizes have determined that the effect of a large slit in distorting the diffraction pattern is mainly in the low angle ($2\theta < 15^{\circ}$) region. Reflection geometry was used for all data in this work because of the higher intensity available. CuK_{α} radiation was used at 45KV, 40 mA. Both a Ni filter and Pulse Height Analyzer were used to eliminate unwanted radiation.

For a few samples data were obtained in both point count and recorder modes. For the former, fixed counts of 10^4 were made at each value of 2θ. For the recorder mode, the goniometer was moved at 2°/min and chart speed was adjusted so that the chart absissae divisions corresponded to $0.1^{\circ}(2\theta)$ intervals. After applying all the corrections discussed

below, the two sets of data were found to be equivalent. Hence, the recorder technique was used for the majority of samples. For the isochronals, intensity data were recorded in the 2θ range $10 - 65^{\circ}$, and the base line was taken to be the intensity value at 65°. For the kinetic studies, data were recorded in the 2θ range $10 - 37^{\circ}$, and the minimum intensity value for $2\theta > 30^{\circ}$ was used as the base line. This minimum falls in the 2θ range $35 - 37^{\circ}$.

VII. 3. Data Analysis: The data were corrected by first subtracting the base line intensity and dividing out the L-P and f^2 factors. The data were then normalized to the maximum intensity value in each case. The computer program used for data reduction and plotting is included in Appendix I. Typical intensity profiles before and after correction are shown in Figures VII. 1 and VII. 2. For the isochronals three parameters were obtained from the intensity vs. sin θ plots.

1. d_{002} - from the (002) peak position using $\lambda = 2d\sin\theta$
2. L_c - from the width at half maximum of the (002) peak using Scherrer's formula $L_c = \frac{0.45\lambda}{\Delta(\sin\theta_c)}$
3. L_a - from the width at half maximum of the (hk) band using Warren's formula, $L_a = \frac{0.92\lambda}{\Delta(\sin\theta_a)}$

VII. 4. Results

VII 4. 1. Isochronal Studies: The variations of d_{002}, L_c and L_a for the isochronals are shown in Fig. VII. 3. The interlayer spacing d_{002} decreases initially, is approximated constant at 3.44Å from 1500°C to 2300°C and then decreases continuously to a value of 3.40Å for GC 2800-2. The peak position is difficult to determine precisely, even after all the corrections have been applied. These data are accurate to only $\pm$ .005Å. L_c increases with HTT, and there appear to be two shoulders - the first at ∿1600°C and the second at ∿2150°C. The variation in L_a follows the same general trend as in d_{002} and L_c.

Three regions can be separated in the HTT variation of L_c, L_a and d_{002}. Below a HTT of 1500°C, both L_c and L_a increase with HTT and d_{002} decreases with HTT. From 1500°C to 2100°C d_{002} is approximately constant at 3.44Å while L_c increases continuously, whereas L_a increases only slightly. The third region is above 2300°C, where both L_c and L_a increase with HTT and d_{002} decreases. This is seen quite clearly in Fig. VII. 4, where L_c and L_a are plotted against d_{002}.

VII. 4.2. Kinetic Studies: First the superposition technique[53] for graphitization studies is briefly described. If a property, P, follows first order kinetics,

$$P = P_f + (P_i - P_f) \exp(-kT)$$

where P_i, P_f are the initial and final values of the property P. For a thermally activated process the rate constant k is expected to follow,

$$k = k_o . \exp(-\Delta H/RT) = k_o . K(T)$$

Plotting the property vs lnt, if a translation along ln (time) axis superimposes curves for different HTT, then

$$\ln \frac{K(T)}{K(T_o)} = \ln to - \ln t = \frac{-\Delta H}{R}\left(\frac{1}{T} - \frac{1}{T_o}\right)$$

where the subscript "o" refers to an arbitrarily chosen reference curve of P vs lnt. Hence a plot of such shifts along lnt, needed to superimpose all the curves onto the reference curve, against 1/T gives the activation energy ΔH.

$$\text{Shift} = \ln \frac{K(T)}{K(T_o)}$$

$$\frac{K(T)}{K(T_o)} = \frac{\text{HTT time for a certain data point}}{\text{Equivalent HTT time for the same point from the master curve.}}$$

The plot of L_c vs lnt for five different HTT is shown in Fig. VII. 5. The curves for 1700 and 2000°C are seen to be superimposable but do not overlap the higher HTT curves. This seems to confirm that they belong to a different region and the kinetics of this region is rather slow. The curves for the other 3 HTT's do overlap and taking L_c for GC2700-2 as a reference point they can all be made to fall on one single curve as shown in Fig. VII. 6. The plot of the shifts vs. 1/T shown in Fig. VII. 7 gives an activation energy $\sim 200 \pm 30$ Kcal/mole.

Attempts to perform similar analysis on L_a and d_{002} were only partially successful because of the scatter in the data. A composite plot for d_{002}, using the translations from Fig. VII. 6 is shown in Fig. VII. 8. The variation is seen not to be inconsistent with the calculated activation energy. The inaccuracies in L_a arise from the

superimposition of (004) peak. It is difficult to substract out (004) because of the inherent breadth of the maxima. The width of (hk) band at 75% is not appreciably effected by (004), and this parameter, L_a', can be similarly analyzed. The composite profile and activation energy plots are shown in Figs. VII. 9. and VII. 10. The activation energy is found to be 225 $\pm$ 30 Kcal/mole.

VII. 5. Discussion: Whereas the interpretation of d_{002} is straightforward, L_c and L_a cannot be simply interpreted as crystalline dimensions. It is well known that L_c and L_a contain strain broadening effects, and the real crystallite broadening should be smaller, giving larger L_c, L_a.[42] Also, for a disordered material such as GC the definition of "crystallite" is not clear at all. These have usually been called mean defect free distances in c and a directions respectively. In principle, the strain component can be separated for L_c, if (00l) peaks (l = 2, 4, 6, 8) are available. For GC these peaks are extremely difficult to resolve because of the overlapping of (00l) and (hk) bands.

The separation into three regions and the appearance of two shoulders is in qualitative agreement with pressure graphitization studies[45] where shoulders were seen around 1500 and 2200°C.

The three regions can be understood on the following basis. Up to the HTT of 1500°C, the material is going through some sort of a "settling down" process, e.g., completion of dehydrogenation around 1500°C has been suggested by many workers[45, 46]. The increase in L_c from 1500-2100°C could be due to strain relief. At the end of this stage, we have a highly disorganized carbon with $d_{002} \simeq 3.44$Å and very

small crystallite size. In the third stage the structure slowly evolves towards the ideal graphite structure. But even at 2800°C the interlayer spacing of 3.40Å is much larger than the ideal 3.35Å. It seems that this material is metastable in its disordered form and thermodynamic evidence for this is given in the work of Das and Hücke.[54]

VII. 5.2. Kinetic Studies: In our kinetic data curves of L_c versus log t are seen to be superimposable for 1700°C and 2000°C heat treatment temperatures. It should be possible to study strain relief in this region, although rather long times are required to get small changes. The activation energy for structural change for HTT > 2300°C is found to be ∿200 Kcal/mole. It should be pointed out that no attempt has been made to remove strain broadening effects in this region. If these are large, the effect would be to increase the estimate of the activation energy.

Kinetics of graphitization has been reviewed in detail by Fischbach[1] and Pacault[8]. The activation energy values reported range from 90-270 Kcal/mole. For graphitizing carbons ∿260 Kcal/mole is the accepted value, and the mechanisms is considered to be vacancy diffusion. Unfortunately, estimates of activation energy for vacancy diffusion vary quite a bit and no reliable direct measurement of self diffusion has been made. It is accepted that the activation energy obtained for GC in this study of L_c is less than that for graphitizing carbons. This could be due to an excess concentration of point defects in the disordered structure. "This seems a reasonable assumption, and some experimental evidence is provided by the observation of Delhaes & Marchand on the relative ease

of introducing substitutional Boron into disordered graphitizing carbons compared with the difficulty of introducing it into graphite" (Fischbach).[1]

VII. 5.3. Structure Model for GC: Based upon our experimental observations, the model for structure of glassy carbon should be as follows: Up to 1500°C the precursor polymer decides the structure and Jenkins' interwound laths model would be the appropriate description. Above 2300°HTT, GC is more like a turbostractic carbon and a randomly oriented crystallites model seems to be the correct description. These crystallites would be surrounded by voids and tetrahedrally bonded carbon. The increase in permeability to gases with HTT would require presence of microcracks connecting increasing number of voids to each other. The in-between range description is probably closer to Jenkins' model than anything else.

CHAPTER VIII

Low Temperature Apparatus

VIII. 1. Description: The low temperature facility consists of a multi-chambered cryostat with a superconducting magnet and associated vacuum and electronic systems.

VIII. 1.1. Cryostat: The schematic diagram of the cryostat is shown in Fig. VIII. 1. The cryostat consists of five chambers. BATH is the chamber for liquid He. This is surrounded by an evacuated chamber which is connected to the vacuum chamber surrounding the liquid N_2 chamber. This combined vacuum chamber is called DEWAR. The other three chambers form an insert that fits inside the BATH. The innermost is the SAMPLE chamber. This chamber goes down into the cylindrical hole of the superconducting magnet. The SAMPLE chamber is surrounded by the POT chamber. This chamber is fitted with a needle valve which can be operated from outside to transfer liquid He from the BATH into the POT. POT and BATH are separated by an evacuated chamber called ISO (short for isolation).

The associated vacuum system is shown in Fig. VIII. 2. This system has the ability to evacuate any of the five chambers with the mechanical pump and the POT, ISO and DEWAR chambers can be evacuated with the diffusion pump as well. The pressure in each of the chambers can be read on an NRC thermocouple gauge having a 0-2000μ range. For POT pressures two extra gauges were provided for accurate pressure measurement in 50-800 mm and 0-50 mm range. Cryopumping is used for ISO and DEWAR to attain a vacuum better than 10^{-7} cm of Hg. These chambers are filled with N_2 gas, evacuated, refilled with N_2 gas and evacuated again. This

is repeated at least two times to make sure that only N_2 gas remains inside. The chambers are then diffusion pumped to better than 1μ of Hg pressure and sealed off. As liquid He is filled in the BATH, the N_2 gas liquifies to give an excellent vacuum. The vacuum system is fitted with He(g) and N_2(g) lines as well. He(g) can be introduced in all chambers. N_2 gas is used with DEWAR and ISO chambers only. The system has an automatic liquid N_2 fill relay to maintain liquid N_2 in the outer shield.

VIII. 1. 2. Superconducting Magnet: The superconducting magnet sits at the bottom of BATH chamber as shown in Fig. VIII. 1. It has a cylindrical hole in the center for the sample chamber. The superconducting magnet is wound with Nb 44% Ti filaments in a Cu matrix. It produces a maximum 50KG field with better than 1% homogeneity in a 1 1/2" diameter x 2" region in the center.

The superconducting magnet is powered by a 60A power supply. This is coupled to a sweep supply and interlocked with a He level detector. The He level detector has four resistance sensors approximately 4" apart from each other. When a sensor is immersed in liquid He a green light is lit up otherwise a red light is on. The interlock is such that if all four lights are red, the power supply will not send any current to the magnet. This is to protect the magnet from being operated without sufficient He. The sweep input to the power supply can raise the field from 0 to maximum in a minimum of one minute and maximum of 1000 minutes with choices in between. The maximum field can be set on the power supply by setting the appropriate limit on the current. The power supply has an analog output corresponding to the current being supplied. Thus the field value can be automatically recorded.

VIII. 1.3. Sample Probe: The sample probe used in our experiments is shown in Fig. VIII. 3. It consists of a hollow stainless steel tube with a Cu mounting block for samples and temperature sensors. A screw-on Cu cap is provided to maintain a thermal equipotential. [Copper discs are soft soldered onto the stainless steel tube to simplify alignment in the chamber (and possibly to reduce heat losses)]. The copper mounting block has a heater wire wrapped around it to control the temperature. The sample configuration is as shown in the figure. With this design of the probe, it was possible to study two samples at the same time. All the electrical connections are made with insulated copper wires. These wires were taken inside the stainless steel tube and connected to a 26 pin vacuum sealed connector. Another cable then took those wires to a box from where they were distributed as described in Chapter IX. To reduce noise, twisted pairs were used for current input to the sample, resistance leads and Hall leads. Three temperature sensors were fixed to the copper mount. The GaAs diode sensor was used in conjunction with the temperature controller (see VIII. 4). Pt and Ge resistance sensors were provided for automatic data collection. The Pt sensor was for 40-300^{o}K range and the Ge sensor for T < 40^{o}k.

VIII. 1. 4. Temperature Controller: A cryogenic temperature controller was used to control the sample temperature. This unit supplied a current to the GaAs sensor and the voltage developed was used to measure the temperature by obtaining a null deflection on the meter. With a calibrated sensor the poteniometer setting for a NULL deflection gave the temperature reading. This unit also supplied current to the 10Ω

heater. For automatic control the potentiometer was set at the desired temperature value and the unit was switched in Auto. To safeguard against burning of the heater wire, heater current was manually controlled until the temperature was close to the desired value.

VIII. 2. Operating Procedures: To prepare the system for a RUN the ISO and DEWAR systems were made ready for cryopumping as discussed in section VIII. 1. 1. The flexible liquid He transfer line was prepared in a similar manner. Once prepared, the two chambers and the transfer line remain good for at least five runs, when they should be reprepared. If water condenses on the outside of the cryostat or the transfer line before then, they must be reprepared. The samples were mounted on the sample probe and the probe was lowered into the sample chamber. BATH, POT and SAMPLE were filled with He(g) and evacuated a few times to make sure only He(g) remained in these chambers. These chambers are left with $\sim$2000μ of He, and the automatic liquid N_2 fill unit is left on overnight to cool the system. This precooling is necessary to avoid waste of liquid He. With properly prepared system the overnight precooling brings the system down to $\sim$120K. The magnet resistance is used to monitor magnet temperature. Its room temperature resistance is $\sim$1300Ω. After the overnight cooling it is brought down to $\sim$500Ω. Liquid He transfer is started the next morning with a very slow transfer rate to cool the magnet. As the magnet resistance drops to 0, the transfer rate is increased to fill the BATH with liquid He. As the level of liquid He rises above the magnet the first green light comes on. The transfer line extension going inside the cryostat is raised four inches each time

a green light comes on so that one is always transferring liquid He from above the He level. The transfer is stopped when all the four green lights are on. Now the magnetic field can be turned on. To lower the temperature of the sample liquid He is transferred into the POT. To do this the BATH vent is closed off which develops pressure of boiling He in the BATH. The needle transfer valve is opened and as the POT pressure comes to atm. pressure, the POT vent is opened. As the needle valve allows very slow liquid transfer, it is necessary to keep the BATH vent barely open to avoid popping of the BATH pressure relief valve. As the He gas rate increases at the POT vent, the transfer is complete. The needle valve is closed and BATH vent is opened. The sample He(g) pressure is adjusted for the proper temperature ranges.

4.2-20^{o}k	$\sim$Atm
20-50^{o}k	$\sim$1000μ
50-100^{o}k	200-500μ
100-300^{o}k	$\lesssim$50μ

Once the lowest temperature has been reached, data is recorded and the sample is slowly heated up to the room temperature. The He(g) pressures above were found to be most adequate for automatic temperature control. With too much cooling the heater current is high and with too little cooling the temperature tends to oscillate.

CHAPTER IX

Measurement of Electrical Properties

IX. 1. Description of the System: The schematic diagram of the electronics involved in the measurement of the electrical properties is shown in Fig. IX. 1. The internal oscillator source of a PAR 124 lock-in amplifier was used for the supply V. A 10KΩ resistor was used to generate a current source of ∿1 mA for the low resistance sample. The exact current was determined by measuring the voltage V_s.

$$I_s = V_s/R_s$$

The resistance signal was taken to the inputs of lock-in amplifier 1 and the difference voltage V was determined from the out of the out of the lock-in amplifier 1.

$$V = V_{LA1} \times \text{scale factor (determined by the sensitivity selector switch position)}$$

The Hall voltage leads were similarly taken to lock-in amplifier 2, and the output was used to determine V_H.

The conductivity, σ, was calculated as

$$\sigma = \frac{1}{\rho} = \frac{Rs}{Vs} \times V_\rho \times \frac{b \times t}{1}$$

l = length of the sample

b = width of the sample

t = thickness of the sample

The magnetoresistance was calculated as

$$\frac{\Delta\rho}{\rho} = \frac{\rho(H) - \rho(o)}{\rho(o)}$$

The Hall coefficient was calculated as

$$R_H = \frac{V_H \cdot t \cdot R_s}{V_s \cdot H \cdot 10^8} \qquad \text{(H in Gauss)}$$

To ensure accuracy and to eliminate spurious effects, the magnetoresistance was measured for both directions of the magnetic field H. No significant difference was found for any of the samples studied. All the measurements were done at a signal frequency of 100 c/s, with both the lock-in amplifiers in band-pass mode. The precision of the data was determined by taking many readings at the same temperature without and with the magnetic field. With H = 0 accuracy of $\pm$ .01% was obtained for signals $V_\rho \sim$ .5mV, typical for our samples. In presence of the magnetic field only $\pm$ .05% accuracy could be obtained. This was due to our inability to use the automatic control function of the cryogenic temperature controller, because the GaAs sensor is affected by the magnetic field, especially at low temperatures. Thus small changes in temperature due to changes in the pressure of the chamber and/or eddy current heating could not be automatically corrected for. The reproducibility of the system was checked by taking data on the same sample in different 'runs'. The data from two different 'runs' were within 0.1% of each other.

It was difficult to get accurate measurements of R_H, because the signal was typically $\sim 1\mu V$ and often the misalignment voltage was much larger than that.

IX. 2. Sample Shape: The sample shape was derived based upon the following considerations.

(1) to avoid shorting of the Hall Effect $l/b > 4$.[74]

(2) The side-arm l' was restricted by the smallest width of the available cutter of 30 mil size.

(3) The thickness of the sample was usually taken to be 20-30 mils. This was found to be satisfactory, whereas 10 mil samples gave poorer accuracy in the data because of Eddy current heating effects. It was desirable to have t as small as possible so that V_ρ would not become very small.

To achieve reliable contact to the sample various techniques were tried. Attempts to plate a contact metal were unsuccessful even when the contact face was sandblasted to increase surface roughness. The plated metal could always be peeled off with fingers. Similar failure was encountered with evaporation attempts. Normal tin solder would not wet the sample and was of no use. Some success was obtained with the use of In solder. Gold or Cu wires (15-20 mil) were rolled into a ball on a flame, hammered into a flat 'foot' and set at the contact with In solder. This could not stand the thermal shock and would come apart in a quick change of temperature and often at low temperatures ($<30^{o}K$). The technique found to be most successful was coating the contacts with silver paint and use a Be-Cu alloy strip as the pressure contact, screwed down into the Cu mounting block. This method was used for all the data replotted in this work.

The samples were prepared by grinding a 1" x 1/2" GC piece, cut with a diamond saw, to $\sim$20 mils. This was polished on a 400 grade paper to obtain thickness uniform within $\pm$ .1 mil. Next the sample was cut using

an ultrasonic cutter. This was made out of tool-steel and mounted on a steel block for proper resonance.

IX. 3. System Operation: The system preparation has already been discussed in Chapter VII. All the electrical units were turned on at least one half hour before any data were taken to stabilize the units. Although often enough data were taken as the temperature was going down, it was found best to first bring the sample to its lowest temperature and then slowly heat it up. Thus in the beginning all the major liquid helium use was dealt with. The BATH was left with at least two lights of liquid He and with properly prepared system each light would last at least three hours allowing a full day to collect data of the two samples inside.

The proper pressure ranges for sample chamber have already been mentioned in Chapter VII. To take a conductivity reading ($H = 0$), the automatic temperature control could stabilize the temperature in not much more than one minute. For $H \neq 0$ data it was necessary to stabilize the temperature for about 5 minutes, so that the constant current needed to maintain the temperature could be manually set for the time it took to take the data. This was necessary since automatic temperature control was not possible because of the magnetic field's effect on the GaAs sensor. At the lowest temperature heater current in the X.03 Amp range is sufficient and more should not be used. If more is needed, this would mean too much liquid He boiling off from a badly prepared system, and temperature stability is poor. From 20-50 the range should be X.1A and later X1 Amp. Above 100K, it is common to have .6 Amp current -

this is primarily determined by the best possible vacuum obtainable in the sample chamber.

The magnetic field takes about one minute to stabilize and data should be taken after that time. The liquid N_2 automatic relay is a big source of noise input to the system and data should not be taken during the time the relay changes its state.

In a typical 'run' the sample temperature was first brought down to the lowest temperature and σ readings were taken in steps of $1^{o}K$ up to $10^{o}k$. At $10^{o}k$ the current for constant temperature was determined and $H \neq 0$ readings were taken. The $H \neq 0$ sets were taken at 10, 20, 40, 60, 77.35^{o}, 100, 150, 200, 250, and $300^{o}k$. Conductivity readings were taken in steps of $2^{o}k$ from $10\text{-}20^{o}k$, 4^{o} steps from $20\text{-}40^{o}k$, in 5^{o} steps to $100^{o}k$ and 10^{o} steps from there on to $300^{o}k$.

CHAPTER X

Electrical Properties of Glassy Carbon

X. 1. Introduction: The electrical properties extensively studied were conductivity, σ, and magnetoresistance $\frac{\Delta\rho}{\rho}$. The experimental results are presented first, followed by a phenomenological analysis, comparison with theory, discussion and conclusion.

As described in Chapter IX, Hall Effect data were difficult to obtain due to the frequent presence of a large misalignment voltage. Reliable data could be obtained only for a few samples. Typical magnetic field and temperature dependence of the Hall Coefficient, R_H, is shown in Fig. X.1. A weak dependence on temperature can be seen at low fields. At high fields, R_H saturates and the temperature dependence disappears. The saturation R_H value is plotted against HTT for the isochronically heat treated specimens in Fig. X. 2. The general shape of the curve is in agreement with Yamaguchi's data on GC A. The variation in the number of carriers calculated from $n = \frac{1}{e.R_H}$ is shown in Fig. X.3. Although the numbers obtained are larger by a factor of 10, the general shape of the curve is in agreement with the variation in the number of spins with HTT seen in the ESR work of Orzeszko and Yang.[32] No further analysis of the Hall Effect data shall be presented.

X. 2. Experimental Results:

X. 2.1. Conductivity σ: The room temperature conductivity for the isochronally heat treated specimens is found to be $\sim 200\Omega^{-1}\text{-cm}^{-1}$. The change in σ at the lowest temperatures studied ($\lesssim 10^{\circ}K$) is found to be <25%. Typical dependence of σ on T in the high HTT region (HTT > $2000^{\circ}C$) is shown in Fig. X.4. For GC samples with HTT < $2000^{\circ}C$ the low

temperature behavior of σ is markedly different as shown in Fig. X.5. The temperature dependence of σ is analyzed in the following section.

X. 2.2. Magnetoresistance $\frac{\Delta\rho}{\rho}$: The magnetoresistance was found to be negative for all the samples studied. The magnitude of $\frac{\Delta\rho}{\rho}$ increases with the applied magnetic field H and as the measurement temperature, T, is lowered. The magnitude $|\frac{\Delta\rho}{\rho}|$ also increases with HIT. This is shown in Fig. X. 6 where $\frac{\Delta\rho}{\rho}$ at H = 50 KG is plotted against HIT for a few temperatures. Typical H, T dependence of the magnetoresistance is shown in Figure X. 7.

X. 3. Phenomenological Analysis:

X. 3.1. Conductivity: The initial attempts[75] (now considered inadequate) to analyze the temperature dependence of σ consisted of plotting $\ln\sigma$ vs $1/T$. The incentive came from the apparent semiconducting behavior of σ. A typical plot is shown in Fig. X. 8. A straight line dependence can be found at higher temperatures and the activation energy calculated from the slope gives a value $\sim$2 meV for all the samples. It was suspected that the major contribution to σ may come from hopping conduction among localized states, and a plot of $\ln\sigma$ vs $1/T^{1/4}$ was attempted to determine if variable range hopping is the right mechanism. The data of Fig. X. 8 are replotted in Fig. X. 9. A linear relationship is found only over a limited range of temperatures. This is suspicious since for other cases where hopping conduction is in fact observed, the dependence extends over a large range of temperatures.[34, 35]

The next attempt was prompted by the ESR study of Orszesko and Yang[32] who found a comparable density of localized and conduction spins over a broad range of HTT in GC. It was anticipated that due to the small crystallite size in GC (Chapter VII) a boundary scattering mechanism should dominate for extended states at all temperatures. To separate the two contributions $\ln\sigma$ was plotted against T. The curves were found to be straight lines over a long range of temperatures. At low temperatures, depending upon the HTT, two characteristics were evident. (i) saturation for HTT > 2000°C and (ii) a sharp decrease in σ for HTT < 2000°C. Typical plots are shown in Figs. X. 10 and X. 11. The intercept σ_o of the straight line $\ln\sigma = \ln\sigma_o + A.T$, is found to be equal to (within the measurement accuracy) the saturation value of higher HTT material. The plot of σ_o **vs** HTT is shown in Fig. X. 12.

Boundary scattering is expected to give rise to a temperature independent contribution to σ.[26] (see X. 4.1) Taking σ_o to be such a contribution, plots of $\ln(\sigma-\sigma_o)$ vs $1/T^{1/4}$ were found to be straight lines for all the samples, as shown in Fig. X. 13 and Fig. X. 14. The variation in the slopes of these plots is small, but the trend is toward somewhat increasing slope as the HTT is lowered.

The remaining contribution in σ is found to be HTT sensitive at low temperatures. As can be seen in Fig. X. 15, the decrease in σ becomes more pronounced as the HTT is lowered.

X. 3.2. Magnetoresistance: The first attempt to analyze $\frac{\Delta\rho}{\rho}$, consisted of determining the field dependence at a fixed T. Plotting $\frac{\Delta\rho}{\rho} \propto H^h$ on a log-log scale, a power relationship $\frac{\Delta\rho}{\rho} \alpha H^n$ was found to be applicable

at high fields. The HTT, T dependence of the exponent n is shown in Fig. X. 16. The behavior of n for HTT > 2000°C is quite consistent. It increases from ∿1.0 at 10°k to ∿2.0 at 100°k. There is also a slight increase in n as HTT is lowered. For HTT < 2000°C no generalizations can be made.

To analyze the combined (H,T) dependence $\left|\frac{\Delta\rho}{\rho}\right|^{1/2}$ was plotted against log H/T. This resulted in a series of parallel curves, as shown for one case in Fig. X. 17. Upon introducing a parameter $\lambda(T)$ in the absissae log $\lambda H/T$ these could be superimposed on a single curve, as shown in Fig. X. 18. The same analysis was applicable to all the samples, i.e. by an appropriate choice of λ's, $\left|\frac{\Delta\rho}{\rho}\right|^{1/2}$ could be plotted on a single curve as a function of log $\frac{\lambda H}{T}$. Furthermore, the curves for various HTT samples could be superimposed by a translation along the absissae.

To eliminate the arbitrariness in the choice of $\lambda = 1$ at 10°K in each case, the temperature dependence of λ was investigated. λ was found to be proportional to $T^{1/2}$ in most cases. The next step was to plot $\left|\frac{\Delta\rho}{\rho}\right|^{1/2}$ against $H/T^{1/2}$. In this plot all data automatically fall on a single curve. This plot was successful for all the higher HTT samples. An example is shown in Fig. X. 19. Below 2000°C HTT, the data do not behave as well and departure can be seen in Fig. X. 20 for 1800-2. The log $\left|\frac{\Delta\rho}{\rho}\right|^{1/2}$ versus log $(H/T^{1/2})$ curve can be compared to $B_{1/2}$ (x) function as shown in Fig. X. 21.

X. 4. Theory and Discussion:

X. 4.1. Conductivity: The conductivity is found to consist of three contributions. (i) A temperature independent σ_o, (ii) variable range

range hopping $\sigma_{hop} \propto \exp(-B/T^{1/4})$, and (iii) an anamolous part at low temperatures in lower HTT material.

A temperature independent contribution due to boundary scattering in carbon has been found earlier in the work of Mrozowski[26], who analyzed the temperature dependence of resistivity in terms of a model where an energy gap between valence and conduction bands was assumed. Excess holes were postulated which were considered to be the result of trapping of resonance π electrons by carbon atoms on the periphery of crystallites. The temperature dependence was successfully explained by assuming a temperature independent boundary scattering contribution and a phonon scattering term linear with T. An anamolous contribution was seen for small crystallite size materials which was called "contact resistance C(T)". Klein[24] also found a temperature independent boundary scattering contribution in his study of electrical properties of pyrolytic graphites.

To check the consistency of the assumption of a temperature independent contribution of boundary scattering to conductivity, we calculate σ_o using

$$\sigma = \frac{n.e^2.\tau}{m^*}$$

where n is the number of the carriers, τ is the mean scattering time given by

$$\tau = l/v$$

l = mean free path

v = velocity of carriers

and m^* is the effective mass of carriers.

We take n to be the value obtained from R_H in the high HTT range. The quantity n is not expected to change appreciably with temperature, as seen in the weak dependence of R_H on temperature in our data and that of Yamaguchi.[29] Other studies on carbons[30, 31] also seem to indicate that when $\frac{\Delta\rho}{\rho}$ similar to our is observed, R_H does not vary much with temperature. As will be discussed later, this is a natural consequence if the fermi level is pinned down by localized states. We take n to be $7.10^{19} cm^{-3}$.

The mean free path, l, would be of the order of the crystallite size L_a (Chapter VII). The value taken here is $30A^o$. The velocity of carriers is taken to be the same as in graphite. The justification comes from the observed closeness of GC and graphite K-emission bands in our work and the photoemission studies of Shirley et al.[56] Little change is expected in the velocity with regard to temperature, since the fermi level is pinned down by localized states. Klein[24] has also concluded that v is only weakly dependent on temperature. We take v to be 2×10^7 cm/sec (Ref. 76), and m* to be $\sim 0.5 \times m$, where m is the mass of the free electrons, for carbons with crystallites of about $30A^o$ diameter, as deduced by Mrozowski.[26] The calculated σ_o is 590Ω l-cm^{-1}. This value is about three times larger than measured which could be due to a too large value of n calculated from R_H. The order of magnitude comparison is satisfactory.

The contribution of the localized states to conductivity, , is via hopping conduction mechanism. At low temperatures, when tunnelling to farther than the nearest neighbour is possible, the conductivity varies as[34]

$$\ln\sigma = A - B/T^{1/4}$$

where

$$B = 2.1\left(\frac{\alpha^3}{k_B.N}\right)^{1/4}$$

α = decay parameter of localized wave function with distance $R(e^{-\alpha R})$

k_B = Boltzman's constant

N = Density of states per cm^3 per eV.

No attempt has been made to pinpoint the exact mechanism, because as discussed by Hill[25], a straight line fit to $1/T^{1/3}$ of $1/T^{1/7}$ would be equally possible. The trend of increasing slope B at lower HTT is consistent with stronger localization (larger α) expected in the structurally worse material.

The anamolous part is found to became more pronounced as HTT is lowered. Thus it is related to structural disorder. We believe that it arises from the lath-like structure of the lower HTT materials. Whereas at higher T the carriers are scattered at a distance, measured by L_a, at low T the carrier motion is impeded by the curvature of these laths. The curvature of these laths might present some sort of barrier increasingly difficult to surmount as T is lowered. There might be some correspondence between this anamolous part and the contact resistance C(T) in Mrozowski's[26] work.

The temperature dependence of σ found in this work is similar to that seen previously in other studies[24, 29, 20, 57], although the analysis has never been as thorough. Bucker[58] found only a $T^{1/4}$

dependence of $\ln\sigma$ for a glassy carbon upto HTT = 1200°C. This might be due to the poor crystallinity of his material. It seems that his material might have been like amorphous carbon films which have crystallites of size $\lesssim 10A^{o}$, and a $T^{-1/4}$ law is obeyed over a long range of temperatures.[59] A linear dependence of log σ on T or log T has been found by some workers for amorphous carbon films.[60] It seems likely that an analysis similar to ours might be applicable in these cases.

X. 4.2. Magnetoresistance: The theories of negative magnetoresistance have been summarized by Delhaes et al.[28] Based upon our understanding of the behavior of conductivity in GC, it is clear that the theories applicable are those which describe the effect of magnetic field on various scattering mechanisms. The magnetoresistance due to boundary scattering, scattering due to localized spins and hopping conduction mechanisms, is expected to be negative. Although the contribution of localized spin scattering to σ has been neglected in our discussion of the temperature dependence of σ, it does not affect our separation of σ into σ_o and a hopping part as discussed later in this section.

Negative magnetoresistance due to boundary scattering has been shown[37] to be proportional to H^2 for low fields. We have also shown (see Appendix II) that this negative $\frac{\Delta\rho}{\rho}$ is a strong function of crystallite size, and a L_a^2 dependence is expected. The estimated $\frac{\Delta\rho}{\rho}$ due to this mechanism at the highest value of H = 50 kG is < .2%. Thus it is not expected to be important for our case.

There is no widely accepted theory for magnetoresistance in the hopping conduction regime. Mott[65] has suggested that a localized spin

could form a self-trap energy for hopping conduction. Application of a magnetic field results in removing this extra activation energy giving negative $\frac{\Delta\rho}{\rho}$. This effect would be expected to be largest at high fields and low temperatures. Experimental studies indicate that maximum $\frac{\Delta\rho}{\rho}$ observed when conduction is solely by hopping is of the order of 1%. Since in our case the magnetoresistance is largest at low temperatures - where hopping conduction has negligible contribution - this mechanism is also not important in our case.

It is clear than that the negative magnetoresistance observed for GC must come from field dependent scattering from localized spins. The often quoted result is that $\frac{\Delta\rho}{\rho} \propto - m^2$, where m is the magnetization of the localized spins.[39, 73] We present a simple argument in terms of Kondo spin-flip scattering.* In this scattering mechanism a conduction electron (or hole; the argument is presented for electrons but is equally applicable to both the carriers) interacts with a localized anti-parallel spin resulting in spin reversal for both the conduction electron and the localized spin. If the total number of localized spins is N, then the number of "up" spins

$$n_{up} = N \times P_{up}$$

and similarly,

$$n_{down} = N \times P_{down}$$

where P's are the respective probabilities. Since the conduction electron interacts with a localized anti-parallel spin, the resistivity, ρ, can be written as

*The author is grateful to Professor L. M. Falicov for pointing out this simple agreement.

$$p_{up} \propto n_{down}$$

and

$$p_{down} \propto n_{up}$$

The total conductivity σ is given by,

$$\sigma = \sigma_{up} + \sigma_{down} = \frac{1}{p_{up}} + \frac{1}{p_{down}} = \frac{1}{\rho}$$

In the absence of the magnetic field (H = 0)

$$p_{up} = p_{down} = 1/2$$

since

$$p_{up} + p_{down} = 1$$

In the presence of the field the total magnetization is given by

$$M(H) = N(p_{up} - p_{down})$$

Again, since the probabilities should add to 1,

$$p_{up} = \frac{1 + m}{2} \qquad \text{where } m = M/N$$

and

$$p_{down} = \frac{1 - m}{2}$$

Therefore,

$$p(H = 0) \propto \frac{4}{N}$$

and

$$p(H) \propto \frac{4}{N} (1 - m^2)$$

The magnetoresistance is given by

$$\frac{\Delta\rho}{\rho} = \frac{\rho(H) - \rho(0)}{\rho(0)} \propto - m^2$$

The combination of the spin-flip scattering mechanism to σ is expected to be temperature independent in this approximation, and the affect is to change σ_o by at most a few percent.

Based upon similar ideas, Toyozawa[38] analyzed the case of impurity conduction on the metallic side of nonmetal-metal transition in semiconductors and concluded that if we define

$$S = \frac{1}{H^2}\left(\frac{\Delta\rho}{\rho}\right)$$

$$H \to 0$$

then $S^{-1/2}$ has a linear dependence $(T + \theta)$ characteristic of antiferromagnetically coupled moments. Mott[62] disagrees with Toyozawa's[38] assumption of free moments in metallic impurity conduction, but has pointed out that antiferromagnetic coupling will persist on the metallic side of the transition.[62]

Our observations indicate that m follows a $f(H/T^{1/2})$ dependence over a large range of temperatures and fields. Plots of $\left|\frac{\Delta\rho}{\rho}\right|^{1/2}$ with $H/T^{1/2}$ show a linear region for small values of $H/T^{1/2}$ as shown in Fig. X. 22. This implies a $T^{-1/2}$ dependence of the susceptibility χ, instead of the T^{-1} expected. Before completing this discussion it is appropriate to discuss metal-insulator transition in carbons and the band model for GC and other carbons. These are described in the next subsection, and this discussion will be concluded in the following one.

X. 4.3. Band Model for Carbons: The earliest band model for carbons is due to Mrozowski[26], who envisages a decreasing band gap with HTT, eventually resulting in the overlap of the valence and conduction bands.

A similar model has been suggested by Klein[24] for pyrolytic graphites. Recent work of Carmona, Delhaes et al[61] suggested a nonmetal-metal transition in carbons around a HTT of 700°C. This is also seen in Mrozowski's[26] work and the study of Bucker[58] on GC.

Whereas the possibility of nonmetal-metal transition in carbon seems to be quite clearly demonstrated by the change in conductivity by many orders of magnitude, it should be pointed out that it differs strongly from more common examples of metal-insulator transition, e.g., V_2O_3. For V_2O_3 the transition occurs as a function of temperature, T, and is reversible.[77] The transition in carbons is an irreversible process. Matters are further complicated by the inhomogeneous structure of carbons heat treated at lower temperatures. These carbons have small crystallite sizes and the C-C bonding at the boundaries of these crystallites is different from graphitic sp^2 bonding.

We believe that nonmetal-metal transition does take place in carbons, although considerably more work is needed to understand this phenomenon. On the insulator side of the transition the fermi level is expected to be in the middle of the energy gap (or at least a mobility gap), and it does not seem necessary to assume it to lie in the localized states as suggested in reference 61. On the metallic side of the transition the fermi level lies inside the valence band. That it is indeed so is supported by the positive sign of R_H found in many studies of transport properties of carbons.[28, 30]

On the metallic side an Anderson transition due to disorder is also expected. There would be localized states in the tails of valence and

conduction band. Thus, a mobility gap would exist[34], and these would be the energy gaps observed by Mrozowski.[26]

Based upon these ideas, the band model for carbons should be as shown in Fig. X. 23. The fermi level lies on the high mobility side of the mobility shoulder inside the valence band. As heat treatment progresses, the mobility gap is reduced. The fermi level moves closer to the center still situated near the top of the extended states inside the valence band. For soft carbons the mobility gap finally closes, the fermi level moves near the center, graphitic overlapping band structure is formed, and the conductivity becomes metallic. For hard carbons the structural disorder is preserved upto the highest HTT, and the conductivity retains its semi-conducting nature.

We believe that the fermi level is pinned down by defects characteristic to the material. These defects act as traps and can also be described as localized states. These states are expected to lie in the inhomogeneous part of the structure, most likely on the boundary of the crystallites. That E_f could be held down inside the valence band by localized states is supported by the work of Ball[64] who contends that localized and extended states are different in nature and could be infinitesimally apart in energy, and in the study of Inglis and Williams[78] where extended and localized states are found to exist in different regions in space for an inhomogeneous system.

These localized states trap electrons from the valence band leaving holes behind and would be responsible for the excess holes postulated by Mrozowski.[26] Thus, there should be a close correspondence between localized and conduction states, as can be seen in the ESR data

from Ref. 32, replotted in Fig. X. 24. Similar correspondence between localized and conduction spins has been seen in the studies of carbon films, and one localized state per crystallite is suggested which could also be true in our case.[59]

X. 4.4. Magnetoresistance - Further Discussion: From the band model it is clear that the magnetoresistance is closely related to the magnetic behavior of the localized spins. Antiferromagnetic coupling between these localized spins has been seen in the low temperature specific heat studies of Mrozowski and Vagh[67] on various carbons including Glassy Carbon.[68] They have also found a strong correlation between the density of spins as seen in ESR experiments and the parameters characterizing the excess specific heat.

On the metallic side, a strong antiferromagnetic interaction between conduction electrons and localized spins is expected.[77] The spin susceptibility of this "highly correlated" electron system is expected to be large at low T. Mott[77] has suggested a schematic dependence of the inverse of the spin susceptibility χ^{-1} on T which is antiferromagnetic at high T, i.e. linear with $(T + \theta)$. However at low T departure has been sketched and has been experimentally observed by Quirty and Marko[69] in Si:P. Their data when replotted gives a linear dependence of χ^{-1} on $T^{1/2}$ as seen in Fig. X. 25.

Heeger[79] has discussed Anderson's arguments for a $T^{-1/2}$ dependence of the change in the electronic susceptibility χ_Q due to correlations which exist because of the Kondo effect and the experimental evidence of such behavior. It is not clear whether or not this model is applic-

able to our case until an estimate of the Kondo temperature T_k can be made. The exact behavior of χ_Q is still not totally clear in any case.[79]

Thus, the magnetoresistance behavior for high HTT material can be understood qualitatively in terms of the highly correlated electron system. For the lower HTT, GC departure has been observed from $H/T^{1/2}$ behavior. The situation here is complicated by the presence of the anamolous term in σ at low temperatures.

The enhanced $\frac{\Delta\rho}{\rho}$ with HTT, as the spin concentration reduces, is in agreement with the experimental work of Ue and Maekawa[70] who found an increase in χ as the donor concentration reduces just on the metallic side of the transition. Mott[63] believes that this is possible in the Brinkman-Rice enhancement model.

X. 4.5. Comparison with Other Studies of $\frac{\Delta\rho}{\rho}$: Comparing with magnetoresistance data on other carbons, we find that whereas Komatsu's[31] data are comparable to ours, Delhaes[28] numbers for negative $\frac{\Delta\rho}{\rho}$ are much larger. This is thought to be due to an increased effect of boundary scattering ($\propto L_a^2$), because their crystallite sizes are 200-300 A^o compared to $L_a \sim 50A^o$ in our case. Komatsu's[31] data for two soft carbon are plotted in Fig. X. 26. The similarity to our data for GC 1800-2 in Fig. X.20 is quite evident. His data on hard carbon seem to be more like soft carbons. In the absence of structural information it is difficult to reach any definite conclusions. It should be pointed out that glassy carbons have a wide range of properties, as seen in the drastic difference between the two glassy carbons studied by Yamajuchi.[29]

Our GC is rather like GC A of Yamajuchi.[29] Komatsu's[31] data have been interpreted by Yugo[71] in terms of Toyozawa's model and reasonable success was obtained. However, the positive component is taken to be H^2 at all temperatures which is not justified because, as pointed out by Komatsu[31], the exponent decreases at lower temperatures.

Komatsu's[31] data are replotted on a log-log plot in Fig. X. 27, and the solid line corresponds to our 2700-2 data as shown in Fig. X. 28. The data of Halbo and Sladek[72] on InSb and Khosla and Fischer's[73] data on CdS are replotted in Fig. X. 29. Although Khosla and Fischer's[73] data seem to have a $H/T^{1/2}$ functional dependence, it is somewhat different from ours. Fig. X. 27 also shows Delhaes'[28] data of longitudinal $\frac{\Delta\rho}{\rho}$ on a soft carbon heat treated at 2300°C, where boundary scattering should have less effect. (The mechanism gives rise to a negative $\frac{\Delta\rho}{\rho}$ for the transverse case, as shown in Appendix II, but in the longitudinal case it should have a small effect, if any). The $H/T^{1/2}$ functional dependence is quite clear, and the solid line is found to be the same as for Khosla and Fischer's[73] data. Delhaes'[28] data for transverse $\frac{\Delta\rho}{\rho}$ on the same sample do not give a clear $H/T^{1/2}$ dependence, and the reason is thought to be the enhanced effect of the boundary scattering mechanism on $\frac{\Delta\rho}{\rho}$.

X. 5. Characterization of GC: The electrical properties point toward separation of the heat treatment behavior of GC into two regions, above and below HTT ca. 2000°C. From the study of x-ray structure parameters, a separation in the HTT range 2000-2300°C was indicated. The structure parameters also indicate a separation around a HTT of 1600°C. As seen

in Fig. X. 15, the drop in σ at lower temperature does become more pronounced below 1500°C HTT. Our Hall Effect data (Fig. X. 2) also confirm separation into three regions.

From our analysis of σ, the temperature independent contribution σ_o should be directly related to the number of carriers and L_a. A broad maximum is seen in our plot of σ_o vs. HTT (Fig. X. 12). Division of σ_o by L_a, shown in Fig. X. 30, does not reproduce the behavior seen in the ESR study of GC (Fig. X. 24). This could be due to errors in the estimate of L_a, but the decreasing concentration with HTT is not inconsistent with the general picture.

A parameter can be derived from the $H/T^{1/2}$ behavior of $\frac{\Delta\rho}{\rho}$ to characterize the HTT behavior of GC. This is taken to be the slope of the linear section of $\left|\frac{\Delta\rho}{\rho}\right|^{1/2}$ vs $H/T^{1/2}$ curve at low values of $H/T^{1/2}$. In absence of an exact functional form with which to compare our data, this parameter is expressed in arbitrary units. (We expect it to be directly related to an effective moment per site.) The HTT variation is shown in Fig. X. 31. A gradual increase above 2000°C HTT is consistent with the Brinkman-Rice enhancement model as discussed in X. 4.4.

Although insufficient samples were studied to provide a reliable value for the activation behavior of electrical properties, preliminary data using the slope as the property P (see Chapter VII) indicate an activation energy of $\sim$75 Kcal/mole. This is similar to values reported for spin annealing in carbon films.[59] The range of activation energies

in carbon films is 35-90 Kcal/mole. The mechanism is supposed to be irreversible clicking of defects at boundaries giving rise to annealing of spins.[59]

X. 6. Conclusions: The sensitivity of electrical properties to structural details is quite clearly demonstrated in our work. The temperature dependence of σ has been separated into a temperature independent boundary scattering part and a hopping part varying as $A.\exp(-B/T^{1/4})$. An anamolous contribution to σ at low temperatures for lower HTT material has been found. The magnetoresistance has been analyzed in terms of a localized spin scattering model. An empirical functional dependence on $H/T^{1/2}$ has been found. A qualitative explanation of the electrical properties in terms of a consistent model has been presented.

X. 7. Recommendations: To complete the understanding of the electrical properties of carbons theoretical work is needed to explain the $f(H/T^{1/2})$ dependence of $\frac{\Delta\rho}{\rho}$ and the anamolous contribution to the conductivity. Recent studies[28-30] fail to analyze the temperature dependence of σ. The separation of σ into its components should be tried along the line presented in this work. In carbons with large crystallite size the effect of boundary scattering $\frac{\Delta\rho}{\rho}$ is large, and its dependence on L_a should be studied to check whether or not it varies as L_a^2 for small H. For hopping conduction, it would be worthwhile to study $\frac{\Delta\rho}{\rho}$ in C films, where the conductivity comes only from hopping conduction. The effect of irradiation on the properties of GC should be studied to understand the nature of defects in GC.

CHAPTER XI

Conclusion

The major contribution of this work has been to provide a consistent picture of the structure and electrical properties of Glassy Carbon (GC). An activation energy for the graphitization behavior of GC, at high heat treatment temperatures, (>2300^{o}C) has been deduced from the x-ray parameters for the first time. The important new findings from the study of electrical properties are the demonstration of a $f(H/T^{1/2})$ functional dependence of the negative magnetoresistance and a unique separation of various contributions to explain the temperature dependence of electrical conductivity.

The scanning electron microscope studies indicate that the GC used in this work is comparable to the best material produced and is thus a good representation of hard carbons. The comparison of the K-emission bands of graphite, diamond and GC heat treated at different temperatures shows that the experimental observations are best explained in terms of a structure model of GC, which consists of both trigonally and tetrahedrally bonded C atoms; the tetrahedrally bonded C content reducing with heat treatment temperature. Single crystal patterns are seen in the transmission electron microscope studies, and a new explanation is proposed to explain these observations. It is proposed that bulk GC does not contain micron size single crystals and that these come about in the process of specimen preparation as built-in stresses are relieved.

X-ray techniques have been used to characterize the structure of GC. The interlayer spacing d_{002} is reduced only to 3.40A^{o} (compared to 3.35A^{o} for graphite) for heat treated at 2800^{o}C for two hours (GC 2800-2),

confirming the "hard to graphitize" nature of GC. The crystallite size parameters L_c, L_a, perpendicular and parallel to graphitic layers, grow only to 28 and 50A$^{\circ}$ respectively for GC 2800-2. Based upon the heat treatment variation of d_{002}, L_c and L_a of the isochronally heat treated specimens for two hours each, three different regions of temperature are found. It is suggested that the first region is over when dehydrogenation is completed. The second region is characterized by a constant d_{002}, and the increase in L_c, L_a in this region may be due to stress relief. The kinetics of change in the third region can be analyzed using the "superposition method" to give an activation energy of 200-225 ($\pm$ 30) K cal/mole. The decrease in d_{002}, the increase in L_c, L_a, and the familiar activation energy value found at high heat treatment temperatures in GC is usually seen at much lower heat treatment temperatures for graphitizing carbons. Thus the hard carbons are seen not to be basically different from soft carbons; the differences result from the different precursors used for these two types of carbons. The appropriate model of the structure of GC, except at high heat treatment temperatures, is the Jenkins' wound lath model. At high HTT a small crystallite model can be used where tetrahedral C-C bonding at the crystallite boundaries is expected.

The electrical properties studied extensively in this work are conductivity, σ, and magnetoresistance, $\frac{\Delta\rho}{\rho}$. The temperature dependence of σ is explained as a sum of a temperature independent contribution due to boundary scattering mechanism and a contribution due to the hopping conduction among localized states varying as A. exp $(-B/T^{1/4})$. For GC

isochronally heat treated at HTT < 2000°C an anamolous contribution to σ is found. This drop in conductivity at low temperatures becomes more pronounced for lower HTT material. It is suggested that this may be due to the lath like structure of lower HTT material. The magnitude of negative $\frac{\Delta\rho}{\rho}$ increases with H and as T is reduced. For HHT > 2000°C the negative $\frac{\Delta\rho}{\rho}$ is found to follow a f $(H/T^{1/2})$ functional dependence. Prior to the present work the explicit form of this functional dependence has not been recognized. Analysis of the possible mechanisms contributing to $\frac{\Delta\rho}{\rho}$ point out that the observed negative $\frac{\Delta\rho}{\rho}$ is due to scattering of conduction carriers from localized spins. The expected dependence of $\frac{\Delta\rho}{\rho}$ on the effective magnetic moment per site m for this mechanism is $\frac{\Delta\rho}{\rho} \propto - m^2$. The discussion points out that anamolous behavior of magnetic susceptibility is expected on the metallic side of the metal-insulator transition, which is observed in carbons around the heat treatment temperature of 700°C. Analysis of some published data of $\frac{\Delta\rho}{\rho}$ in carbons and other materials reveals a f$(H/T^{1/2})$ functional dependence as well. The experimental evidence is quite strong and theoretical work is now needed to complete the understanding of negative magnetoresistance. For HTT < 2000°C the behavior of $\frac{\Delta\rho}{\rho}$ becomes more complex, although the general features remain the same. An energy band model is proposed to explain the observed electrical properties which consists of a pseudo-gap (with mobility shoulders) arising from localization of states due to disorder. The fermi level is pinned down near the top of the extended states inside the valence band due to localized states in the inhomogeneous part of the structure.

APPENDIX I

Computer Program for X-ray Data Reduction

```
RAMXRAY
                PROGRAM RAMXRAY(INPUT,OUTPUT,PLOT,TAPE98,TAPE99=PLOT)
                DIMENSION TOTHETA(200),AI(200),X(200),DI(200),W(200)
                READ 400,RG
          400   FORMAT(A10)
       10       READ 500,N,AO
          500   FORMAT (I3,F6.1)
       20       READ 502,(AI(I),I=1,N)
          502   FORMAT(20(F3.0,1X))
       27       READ 501,(TOTHETA(I),I=1,N)
          501   FORMAT (13(F5.1,1X))
       36       BO=3.141593/360
       40       AIO=-1
       42       DO 40 I=1,N
       44       AI(I)=AI(I)-AO
       46       X(I)=SIN(TOTHETA(I)*BO)
       54       AI(I)=AI(I)*(1+2D*(X(I)**2))*((X(I)**2)*(COS(TOTHETA(I)*BO)))/
                118*(1+(COS(TOTHETA(I)*2*BO))**2)
      102       IF(AI(I) .GT. AIO) AIO=AI(I)
      106    40 CONTINUE
      111       DO 50 I=1,N
      116       AI(I)=100*AI(I)/AIO
      120    50 CONTINUE
      121       JO=0
      121       DIM=-1
      123       M=0
      123       J=0
      124       DO 60 I=1,N
      126       IF(X(I) .LT. 0.20)GO TO 60
      131       IF(X(I) .GT. 0.25)GO TO 61
      134       M=M+1
      136       J=J+1
      137       DI(J)=AI(I)
      141       W(J)=X(I)
      142       IF(DI(J) .GT. DIM)DIM=DI(J)
      146       IF(DIM .EQ. DI(J))JO=J
      151       WM=W(JO)
      153    60 CONTINUE
      156    61 CONTINUE
      156       PRINT 13,RG
          13    FORMAT(A10)
      164       PRINT 4,WM,DIM
          4     FORMAT(E12.5,E12.5)
      174       CALL CCGRAPH(X,AI,N,RG,2HX ,2HI )
      200       CALL CCNEXT
      201       CALL CCGRAPH(W,DI,M,RG,2HX ,2HI )
      205       CALL CCNEXT
      206       END

CCGRAPH
                SUBROUTINE CCGRAPH(X,Y,N,RG,RX,RY)
                COMMON/CCFACT/FACTOR
                COMMON/CCPOOL/XMIN,XMAX,YMIN,YMAX,CCXMIN,CCXMAX,CCYMIN,CCYMAX
                DIMENSION ROUND(4),X(N),Y(N)
                INTEGER RG,RX,RY
                DATA NROUND,PART,ROUND/3,10.,1.0,2.0,5.0/
                CCXMIN=70
       11       CCXMAX=1070
       12       CCYMIN=80
       14       CCYMAX=1080
       16       CALL LINEUP (X,N,ROUND,NROUND,PART,XMIN,XMAX)
       24       CALL LINEUP (Y,N,ROUND,NROUND,PART,YMIN,YMAX)
       36       CALL CCGRID(50,4,6HNOLBLS,50,4)
       42       CALL CCLBL(IFIX(PART),IFIX(PART))
       46       CALL CCPLOT(X,Y,N,4HJOIN,1236,1)
       54       CALL CCLTR(10.,10.,0,3,RG,10)
       64       CALL CCLTR(350.,10.,0,2,RX)
       73       CALL CCLTR(10.,350.,1,2,RY)
      102       RETURN
      103       END
```

APPENDIX II

Negative $\frac{\Delta\rho}{\rho}$ Due to Diffuse Boundary Scattering

Here we derive an expression for the negative magnetoresistance due to diffuse boundary scattering for the simple model used by Fujita.[37] In this model electrons are diffusely scattered at the crystallite boundaries. That is, once electrons arrive at the boundary surface from any direction within the crystallite, they may leave the surface in all possible directions within the crystallite with equal probability.

Consider for simplicity, a rectangular thin layer, a two dimensional model in which an electron moves freely. Let's take an electron starting from the point A in Fig. A. II.1, proceeding on the straight line AC in the absence of the magnetic field and hitting the wall at C. The length EC may be defined as the free path of the electron with respect to the charge transport in the upward direction. If a constant magnetic field of magnitude H is applied in the direction perpendicular to, and into the paper, the electron will describe a circular orbit of radius $R = \frac{m^*.v}{e.H}$. Thus, the same electron starting from the point A with the same velocity v will now travel on a circular arc AC' and hit the wall at C'.

In the absence of the magnetic field, for every process in which an electron leaves the surface with an angle θ with respect to the horizontal and hits the right wall, there exists a corresponding process in which an electron hits the left wall after leaving from the same angle θ and covering the same distance. In general, correspondent pairs can be found by looking at the reflexion symmetry with respect to the axis GG'

which bisects the layer vertically. The two processes indicated in Fig. A II.1 are just those with this correspondence. It is clear that processes in which an electron hits the upper wall KL need not be considered because the free path with respect to the charge transport remains El = FK in both the absence and the presence of a magnetic field.

The change in free path, when a magnetic field is applied is given by DD'-CC' for these correspondent processes. Constructing perpendicular CP and DQ as shown in Figure A. II.1,

$$CC' = CP.\ \sec\ (\theta - (\delta\theta)_1)$$

$$= \ell.\ \sin\ (\delta\theta)_1.\ \sec\ (\theta - (\delta\theta)_1)$$

where $\ell = AC = A'Q$

Similarly, $$DD' = DQ.\ \sec\ (\theta + (\delta\theta)_2)$$

$$= \ell.\ \sin\ (\delta\theta)_2.\ \sec\ (\theta + (\delta\theta)_2)$$

The angles $(\delta\theta)$ and $(\delta\theta)_2$ are angle CAC' and DA'D' respectively, as shown in the figure. Since OA is perpendicular to AC and OB is perpendicular to the line AC',

$$\text{angle AOB} = \text{angle CAC'} = (\delta\theta)_1$$

Similarly, $$\text{angle A'O'B'} = \text{angle DA'D'} = (\delta\theta)_2$$

We consider the situation for which R is large such that the angles subtended by arcs AC' and A'D' are small. In the first approximation

$$(\delta\theta)_1 = (\delta\theta)_2 = \tfrac{1}{2}.(\ell/R) = (\delta\theta),\ \text{and}$$

$$\sin\ (\delta\theta) = (\delta\theta)$$

Then $DD' - CC' = \ell . (\delta\theta) . \quad (\sec(\theta + (\delta\theta)) - \sec(\theta - (\delta\theta)))$

$$= \ell . (\delta\theta) . \sec\theta \tan\theta . 2 (\delta\theta)$$

$$= 2 . \ell . \sec\theta . \tan\theta . (\delta\theta)^2$$

The free path, L, in the absence of a magnetic field is given by

$$L = EC = RD = \ell . \sin\theta$$

The average increase in L is given by

$$L = \frac{DD' - CC'}{2} = \ell . \sec\theta . \tan\theta . \frac{\ell^2}{4R^2}$$

Since, as discussed by Fujita,

$$\frac{\Delta\rho}{\rho} = - \frac{\Delta L}{L}$$

we find that

$$\frac{\Delta\rho}{\rho} = \sec^2\theta . \frac{\ell^2}{4R^2}$$

Averaging over angles θ would give

$$\frac{\Delta\rho}{\rho} = - \frac{\langle\ell\rangle^2}{4R^2}$$

where $\langle\ell\rangle$ is an average of the order of the crystallite size.

To estimate the magnitued of $\frac{\Delta\rho}{\rho}$ due to boundary scattering in GC we take

$$v = 2.10^7 \text{ cm/sec}$$

$$m^* = 0.5\ m$$

$$H = 50kG$$

$$\langle\ell\rangle = 30A^{\circ}$$

With these values $R = 1140A^{\circ}$, and $\frac{\Delta\rho}{\rho} = - .0015 = - 0.15\%$.

REFERENCES

1. Fischbach, D. B., Chem. and Phys. of Carbon, 7, 1, Marcel Dekker, Inc., New York, 1971.

2. Ergun, S., Chem. and Phys. of Carbon, 3, 211, Marcel Dekker, Inc. New York, 1968.

3. Ruland, W., Chem. and Phys. of Carbon, 4, 1, Marcel Dekker, Inc. New York, 1968.

4. Pauling, L., Proc. National Academy of Science, 56, 1646, 1966.

5. Ergun, S. and Alexander, L. E., Nature, 195, 765, 1962.

6. Nelson, L. S., Whittaker, A. G. and Tooper, B., High Temp., Sci., 4, 445, 1972.

7. Fischbach, D. B., Structure of Carbon Materials II, The University of Washington, 1974.

8. Pacault, A., Chem. & Phys. of Carbon, 7, 107, Marcel Dekker, Inc., New York, 1971.

9. Warren, B. E., Phys. Rev., 59, 693, 1941.

10. Noda, T., Inagaki, M. and Yamada, S., J. Non-Crystalline Solids, 1, 285, 1969.

11. Hucke, E. E., "Glassy Carbons" Semi-Annual Reports, The University of Michigan, Ann Arbor, Mich., Contract No. DAHC15-71-C-0283, 1971-1974.

12. Ban, L. L. and Hess, W. M., Proceedings of the 10th Biennial Conference on Carbon, 1971.

13. Ergun, S. and Tiensuu, V. H., Acta. Crysta. 12, 1050, 1959.

14. Noda, T. and Inagaki, M., Bull. Chem. Soc. Japan, 37, 1534, 1964.

15. Furukawa, K., J. Cryst. Japan, 6, 101, 1964.

16. Kakinoki, J., Acta. Cryst., 18, 578, 1965.

17. Nakamizo, M. and Kammereck, R., Proceedings of the 11th Biennial Conference on Carbon, 1973.

18. Nathan, M. I., et al, IBM Research RC4674, 1974.

19. Whittaker, A. G. and Tooper, B., Proceedings of the 11th Biennial Conf. on Carbon, 1973.

20. Bragg, R. H. and Hammond, M. L., Seventh Conference on Carbon, Cleveland, June 1965; also Carbon, 3, 340, 1965.

21. Biswal, M. M. and Bragg, R. H., Proceedings of the 12th Biennial Conf. on Carbon, 1975.

22. Rothwell, W. S., J. Appl. Phys. 39, 1840, 1968.

23. Spain, I. L., Phys. & Chem. of Carbon, 8, 1, 1973.

24. Klein, C. A., Rev. Mod. Phys., 14, 56, 1962.

25. Haering, R. R. and Mrozowski, S., Prog. Semi-conductors, 5, 273, 1960.

26. Mrozowski, S., Phys. Rev., 85, 609, 1952.

27. Delhaes, P., Phys. and Chem. of Carbon, 7, 193, 1971.

28. Delhaes, P., et al, Phil. Mag. 29, 1301, 1974.

29. Yamaguchi, T., Carbon, 1, 47, 1963.

30. Inagaki, M., Komatsu, Y. and Zanchetta, J. V., Carbon, 7, 163, 1969.

31. Komatsu, Y., Carbon, 7, 229, 1969.

32. Orzeszko, S. and Yang, K. T., Carbon, 12, 493, 1974.

33. Ioffe, A. F. and Regal, A. R., Prog. Semi-conductors, 4, 237, 1960.

34. Mott, N. F. and Davis, E. A., Electronic Processes in Non-crystalline Materials, Claredon Press, Oxford, UK, 1971.

35. Hill, R. M., Phil. Mag., 24, 1307, 1971.

36. Wannier, G. H., Phys. Rev. B, 5, 3836, 1972.

37. Fujita, S., Carbon, 6, 746, 1968.

38. Toyozawa, Y. J., Phys. Soc. Japan, 17, 986, 1962.

39. Alexander, M. N. and Holcomb, D. F., Rev. Mod. Phys., 40, 815, 1968.

40. Sparrow, E. M., et al, J. Heat Transfer, Transactions of AIME C, 84, 73, 1962.

41. Autio, G. W. and Scala, E., AIAA Journal, 3, 738, 1962.

42. Ergun, S., Proc. of the 10th Biennial Conference on Carbon, 1971.

43. Fischbach, D. B., Technical Report 32-1228, Jet propulsion Lab., Cal. Tech., 1968.

44. Fischbach, D. B., Private Communication.

45. Chard, W. C., et al, Carbon, 6, 950, 1968.

46. Noda, T. and Kato, H., Carbon, 3, 289, 1965.

47. Fisher, D. W. and Baun, W. L., In "Spectroscopy in Inorganic Chemistry", Vol. 1, Academic Press, 1970.

48. Coulson, C. A. and Taylor, R., Proc. Phys. Soc., A65, 815- 1952.

49. MacFarlane, A. A., Carbon, 11, 73, 1973.

50. Holliday, J. E., J. Appl. Phys. 38, 4720, 1967.

51. Reference 12.

52. Bragg, R. H., Bose, S., and Saxena, R. R., UCLBL Report #5130.

53. Fischbach, D. B., Technical Report 32-532, Jet Propulsion Lab., Cal. Tech., 1966.

54. Das, S., Ph.D Thesis, "Thermodynamic Properties of GC-Graphite Equilibrium", Metallurgical Eng., Univ. of Michigan, Ann Arbor, 1974; also Carbon, 13, 33, 1975.

55. Reference 35.

56. Shirley, D. A., et al, UCLBL Report #1989, 1973.

57. Tsuzuko, T. and Saito, K., Japan J. Appl. Phys., 5, 738, 1966.

58. Bucker, W., J. Non-Crystalline Solids, 12, 115, 1973.

59. McClintock, I. S. and Orr, J. S., Phys. and Chem. of Carbon, 11, 243, 1973.

60. Ref. 139 of Ref. 59.

61. Carmona, F., Delhaes, P. et al, Solid State Comm., 14, 1183, 1974.

62. Mott, N. F., Comments Solid State, 2, 183, 1970.

63. Mott, N. F., Adv. Phys., 21, 785, 1972.

64. Ball, M. A., J. Phys. C.: Solid State Phys., 4, 1747, 1971.

65. P. 216, Reference 34.

66. Mell, H. and Stuke, J., J. Non-Crystalline Solids, 4, 304, 1970.

67. Vagh, A. S. and Mrozowski, S., Carbon, 13, 301, 1975.

68. Vagh, A. S. and Mrozowski, S., Carbon, 12, 645, 1974.

69. Quirt, J. D. and Marko, J. R., Phys. Rev. B, 7, 3842, 1973.

70. Ue, H. and Maekawa, S., Phys. Rev. B, 3, 4232, 1971.

71. Yugo, S., J. Phys. Soc. Japan, 34, 1421, 1973.

72. Halbo, L. and Sladek, R. J., Phys. Rev., 173, 794, 1968.

73. Khosla, R. P. and Fischer, J. R., Phys. Rev. B, 2, 4084, 1970.

74. Putley, E. H., The Hall Effect and Related Phenomena, Butterworths, London, 1960.

75. UCLBL Report #3530.

76. Table 19, Ref. 23.

77. Mott, N. F., Metal-Insulator Transitions, Taylor and Francis, London, 1974.

78. Inglis, G. B. and Williams, F., J. Non-Crystalline Solids, 5, 313, 1971.

79. Heeger, A. J., Solid State Physics, 23, 284, 1969.

80. Bradshaw, W., Private Communication.

TABLE II. 1

Property	Polycrystalline Graphite	GC 1000	GC 2000	GC 3000
Density (g/cc)	1.5-2.0	1.54	1.47	1.36 - 1.42
Gas Permeability (cm^2/sec)	0.10	$10^{-2} - 10^{-14}$	$10^{-10} - 10^{-12}$	$10^{-7} - 10^{-9}$
Tensile Strength (lb/in^2)	440-2000	13,000 - 14,000	17,000 - 29,000	15,000 - 29,000
Compressive Strength (lb/in^2)	1800-8500	110,000	130,000-200,000	86,000 - 150,000
Young's Modulus (10^{-6} lb/in^2)	0.5-1.8	4.0	4.0	3.4
Thermal Expansion ($10^{-6}/^{o}C$)	3.0	9.0	4.2	5.0
Thermal Conductivity ($Cal/cm/^{o}C/sec$)	0.19	---	.010	.012
Electrical Resistivity (10^{-4} ohm-cm)	3.0	---	60	40

TABLE IV. 1

Time. (mins.)	Power (KW) x 30	Temp^{o} C
0	.05	
6	.10	
12	.15	
18	.20	
24	.25	
30	.30	
36	.35	
42	.40	∿1100
57	.45	∿1700
77	.50	∿2100
102	.55	∿2500

TABLE VI. 1

Comparison of K-emission Band Parameters for Various Forms of Carbon

Material	Peak Position A^{O}	Half Width A^{O} (eV)	Index of Asymmetry	Shift in Peak Position from PG Δ(eV
PG[a]	44.90	1.375 (8.8)	0.75	0
GC(2800)[b]	44.80	1.5 (9.6)	0.75	0.64
GC(1800)	44.75	1.5 (9.6)	0.95	0.96
GC(1000)	44.70	1.5 (9.6)	1.00	1.28
Diamond	44.45	1.28 (8.0)	1.35	2.90
Diamond[c]	44.52	(8.1)	1.25	2.10

[a] PG = Pyrolytic Graphite

[b] GC = Glassy Carbon

[c] From Reference 50

FIGURE CAPTIONS

Figure II. 1. The structure of hexagonal graphite

II. 2. The structure of rhombohedral graphite

II. 3. Quinoidal vs. resonating bonds layer structure in graphite

II. 4. The structure of diamond

II. 5. The structure of hexagonal diamond

II. 6. Jenkins' model for the structure of Glassy Carbon

II. 7. Density of states in non-crystalline materials (schematic). E_F is the Fermi energy at the absolute zero of temperature; localized states are shaded. (a) Liquid or amorphous metal. (b) Semi-metal. (c) Semi-metal with deep pseudogap. (d) Insulator or intrinsic semiconductor. (e) Impurity band in heavily compensated n-type semi-conductor. (From Ref. 34.).

III. 1. Typical fracture surface of Tokai GC

III. 2. Typical fracture surface of Beckwith GC

III. 3. Typical fracture surface of Lockheed GC

III. 4. Typical fracture surface of Poly Carbon GC

IV. 1a. Schematic diagram of the graphite furnace

IV. 1b. Photograph showing the graphite furnace, the top assembly, the optical pyrometer and the power supply

IV. 1c. Photograph showing the rayo-tube heat-eye

IV. 2. Photograph showing the top assembly (Plate A is directly below the prism), the graphite crucible and the crucible clip.

V. 1. Diffuse SAD ring pattern from GC 2800-1

V. 2. BF picture corresponding to Fig. V. 1

V. 3. DF picture corresponding to Fig. V. 1

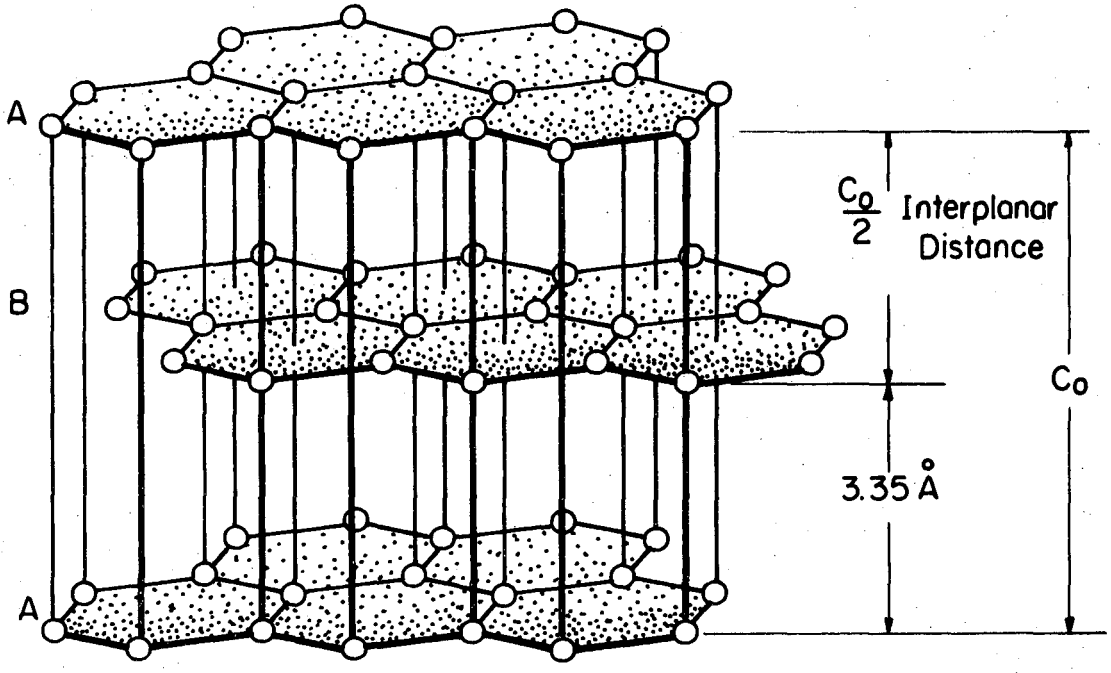

XBL 765-6890

Figure II. 1

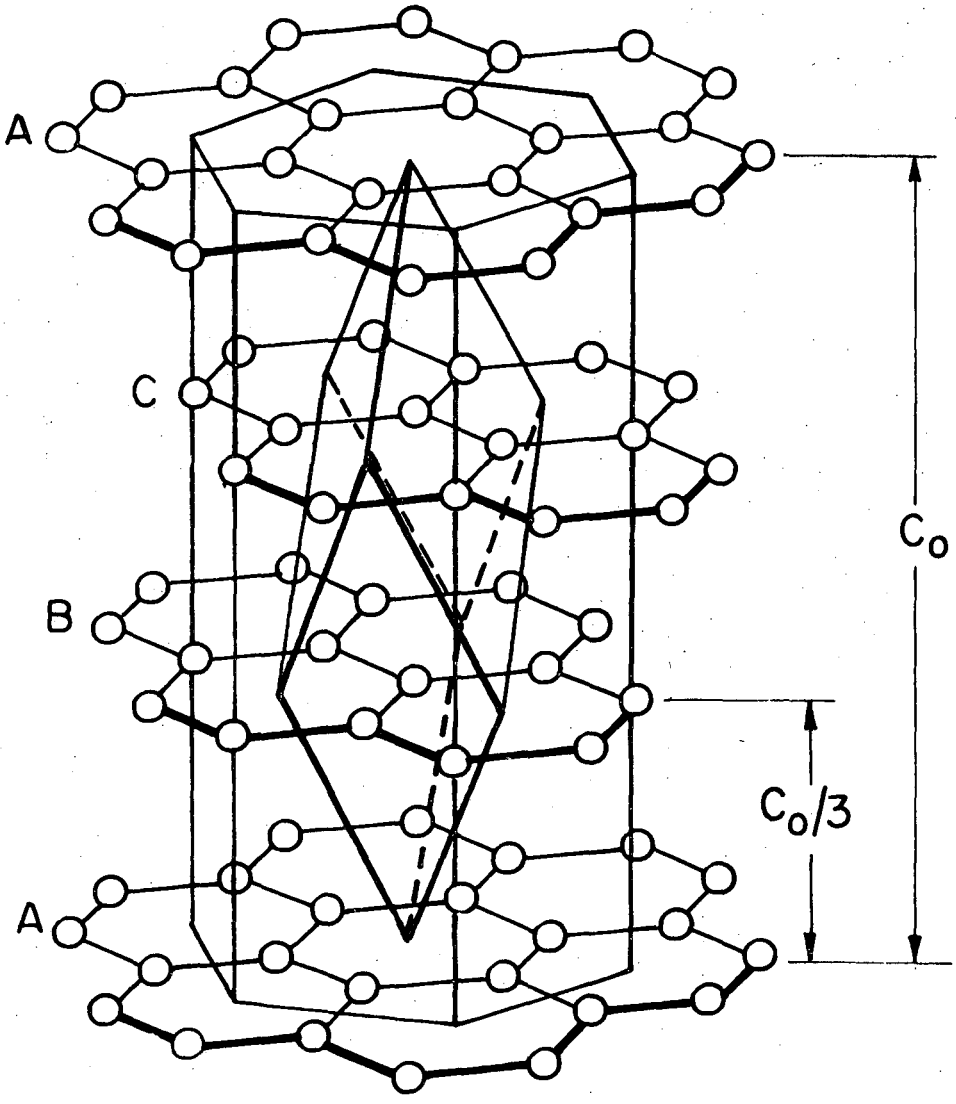

XBL765-6891

Figure II. 2

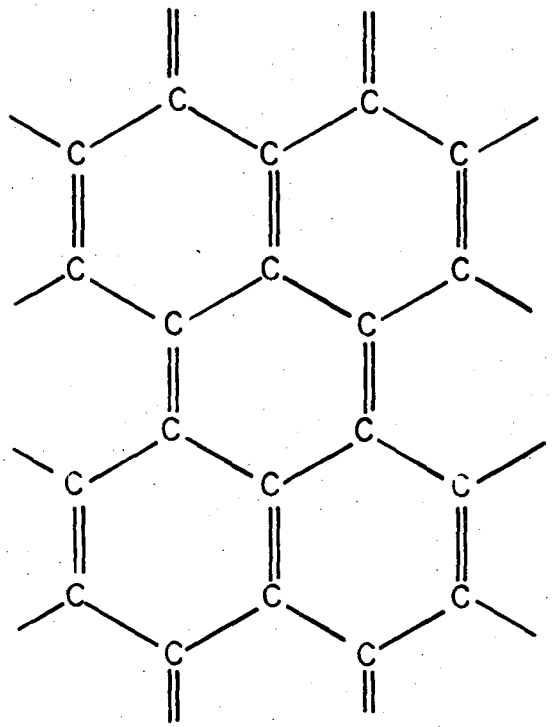

Quinoidal Layer Structure

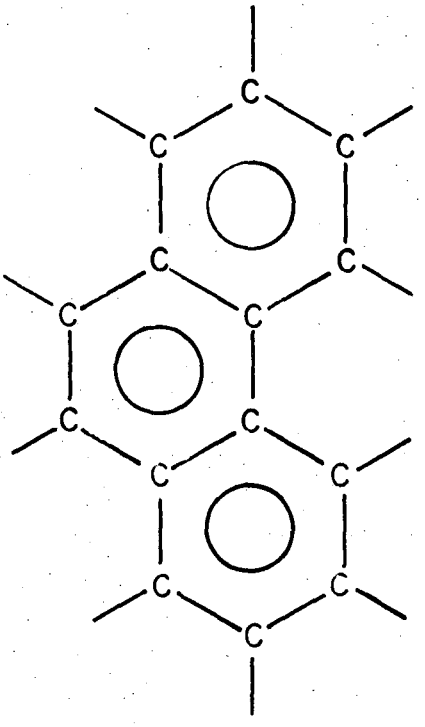

Resonating Bonds Layer Structure

XBL 765-6894

Figure II. 3

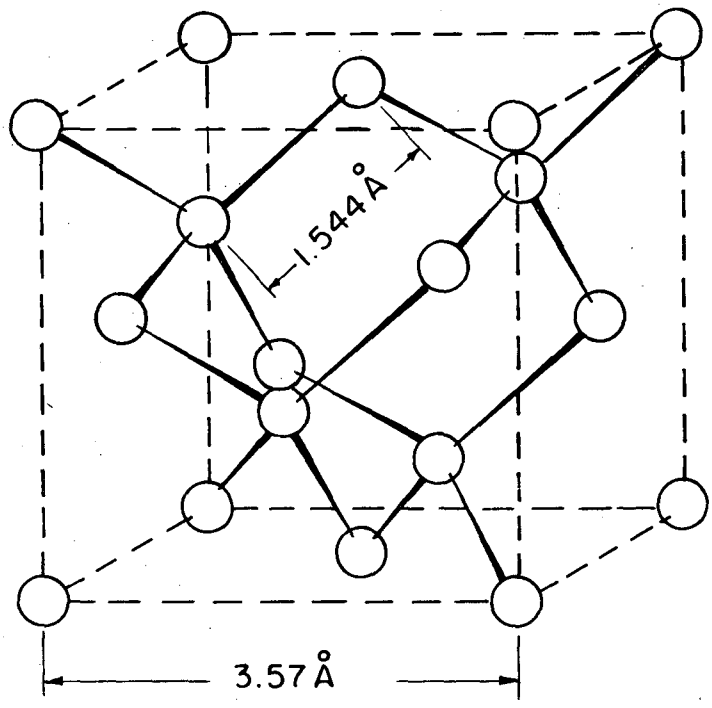

Figure II. 4

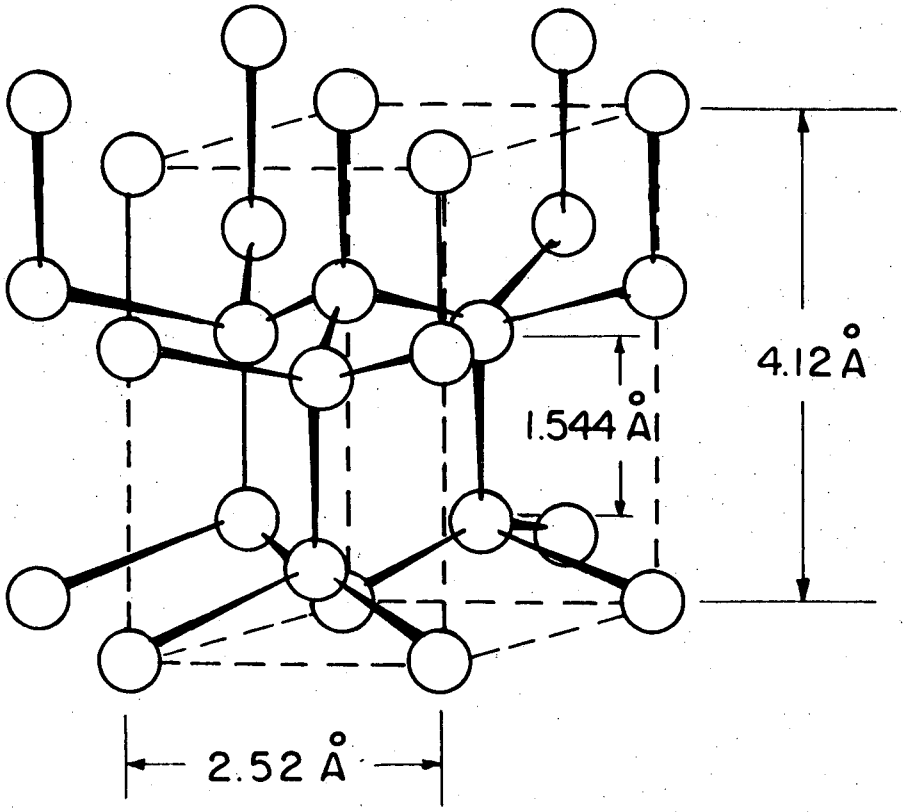

Figure II. 5

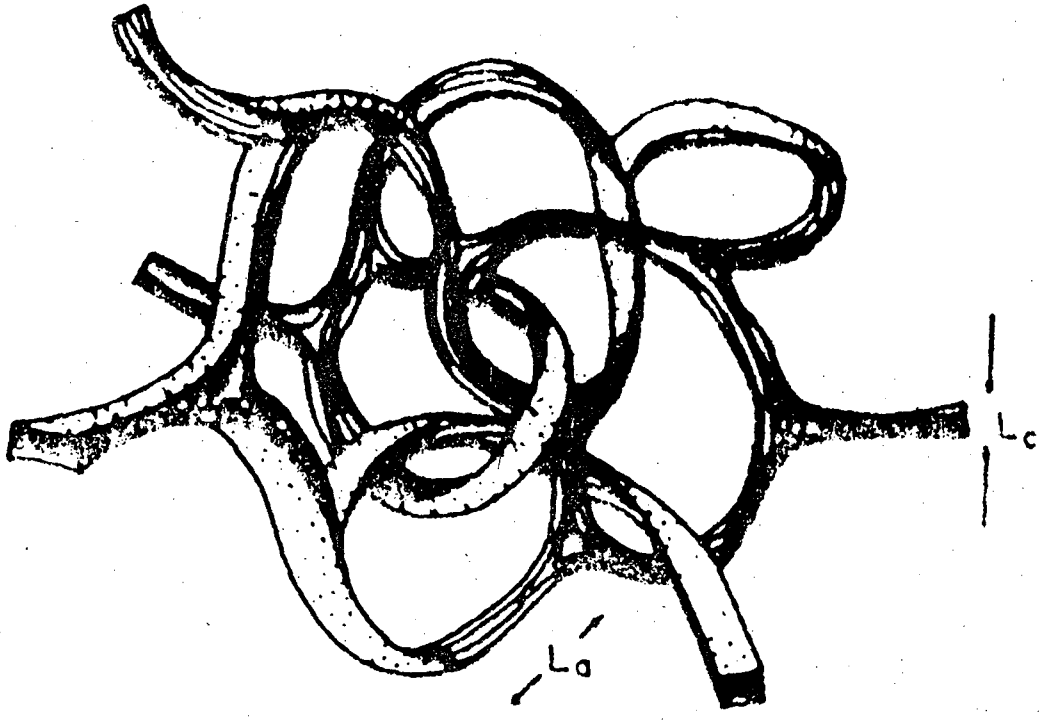

XBL 766-8079

Figure II. 6

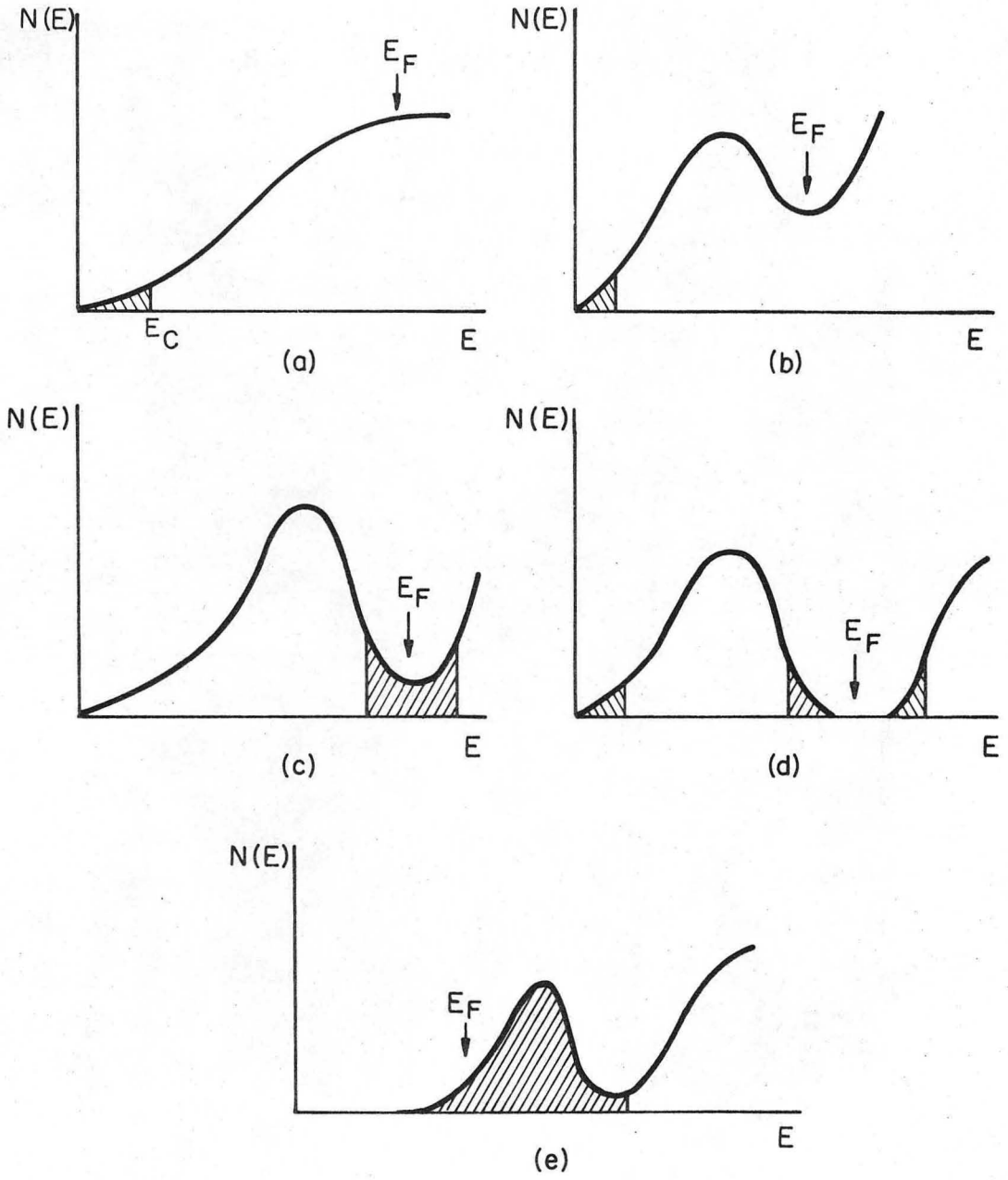

XBL 765-6895

Figure II. 7

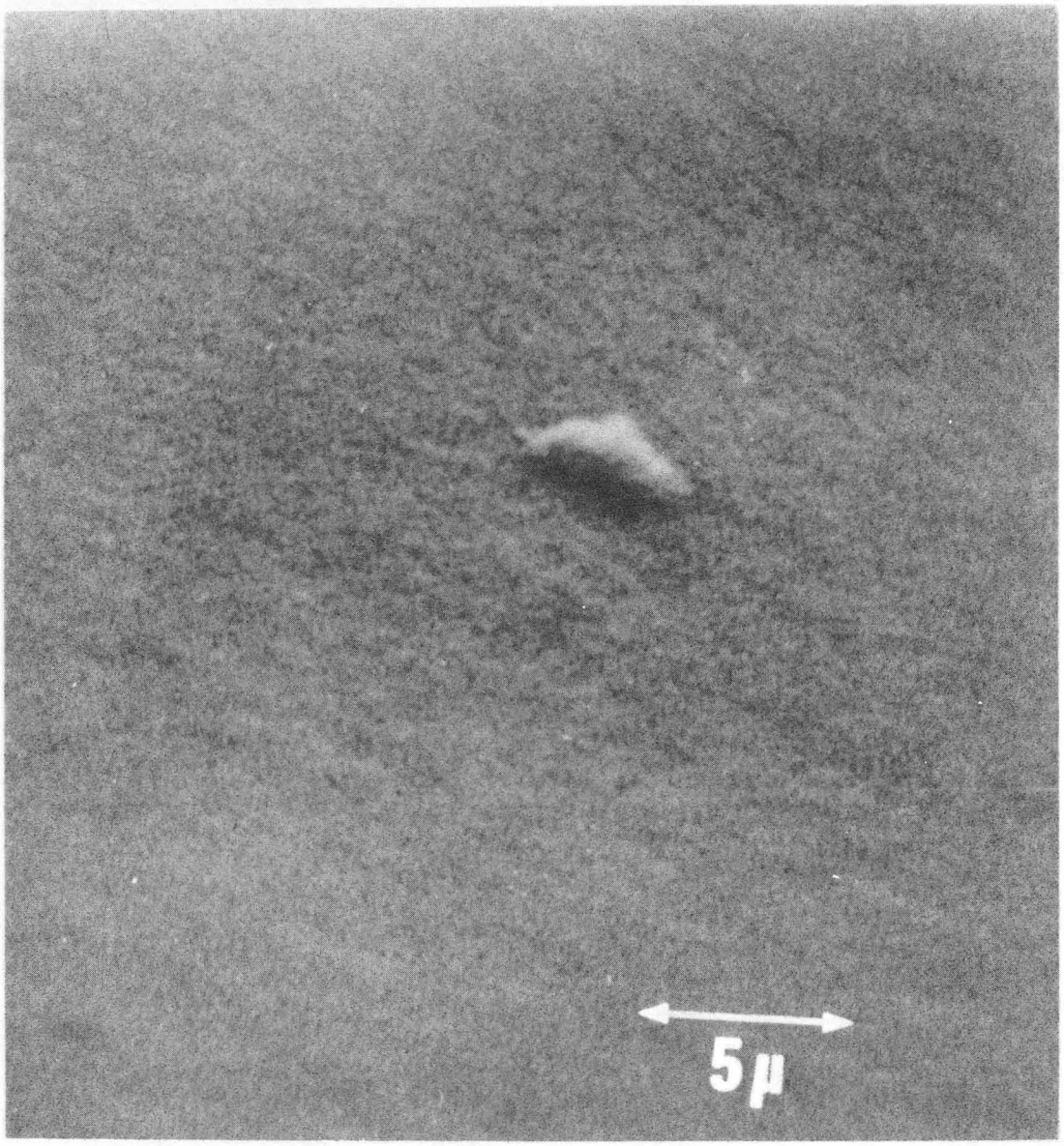

XBB 766-5210

Figure III. 1

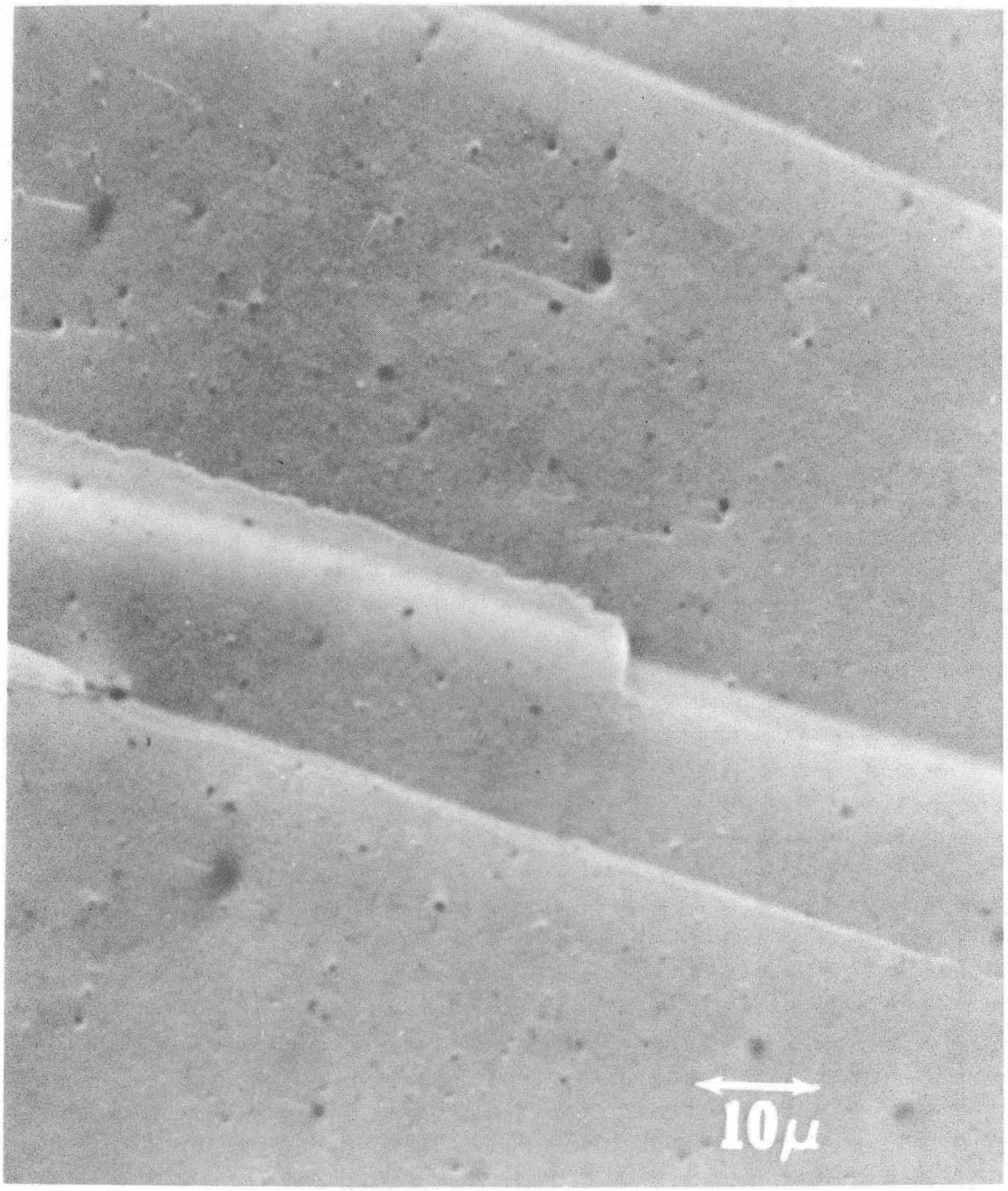

XBB 766-5213

Figure III. 2

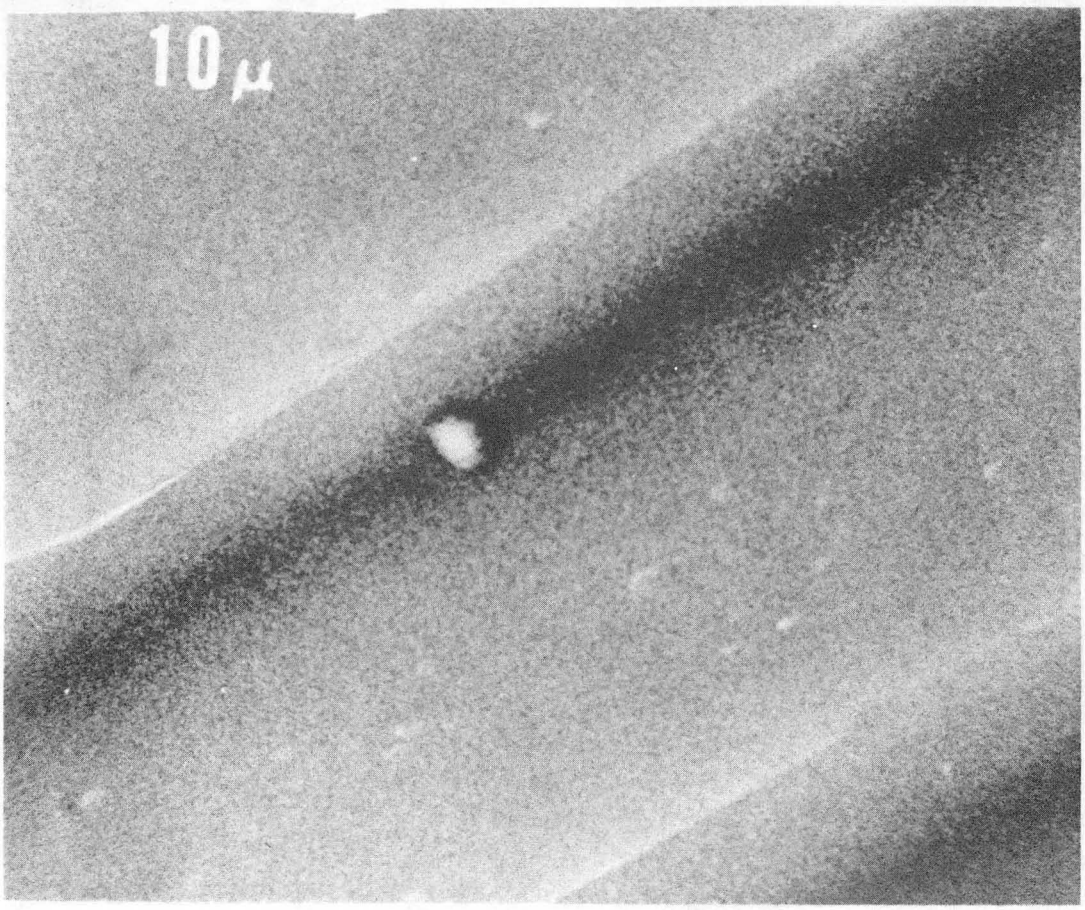

XBB 766-5211

Figure III. 3

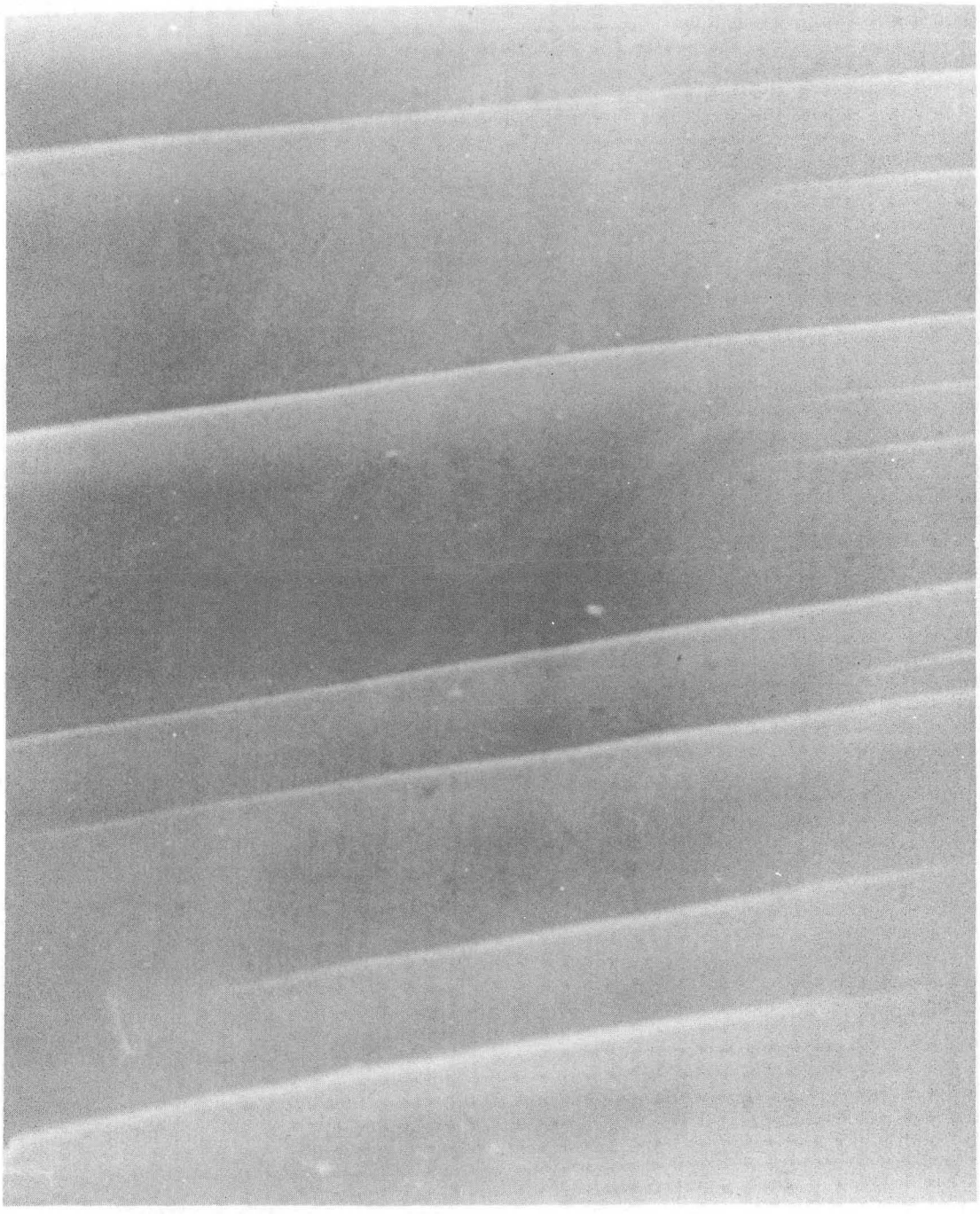

XBB 766-5212

Figure III. 4

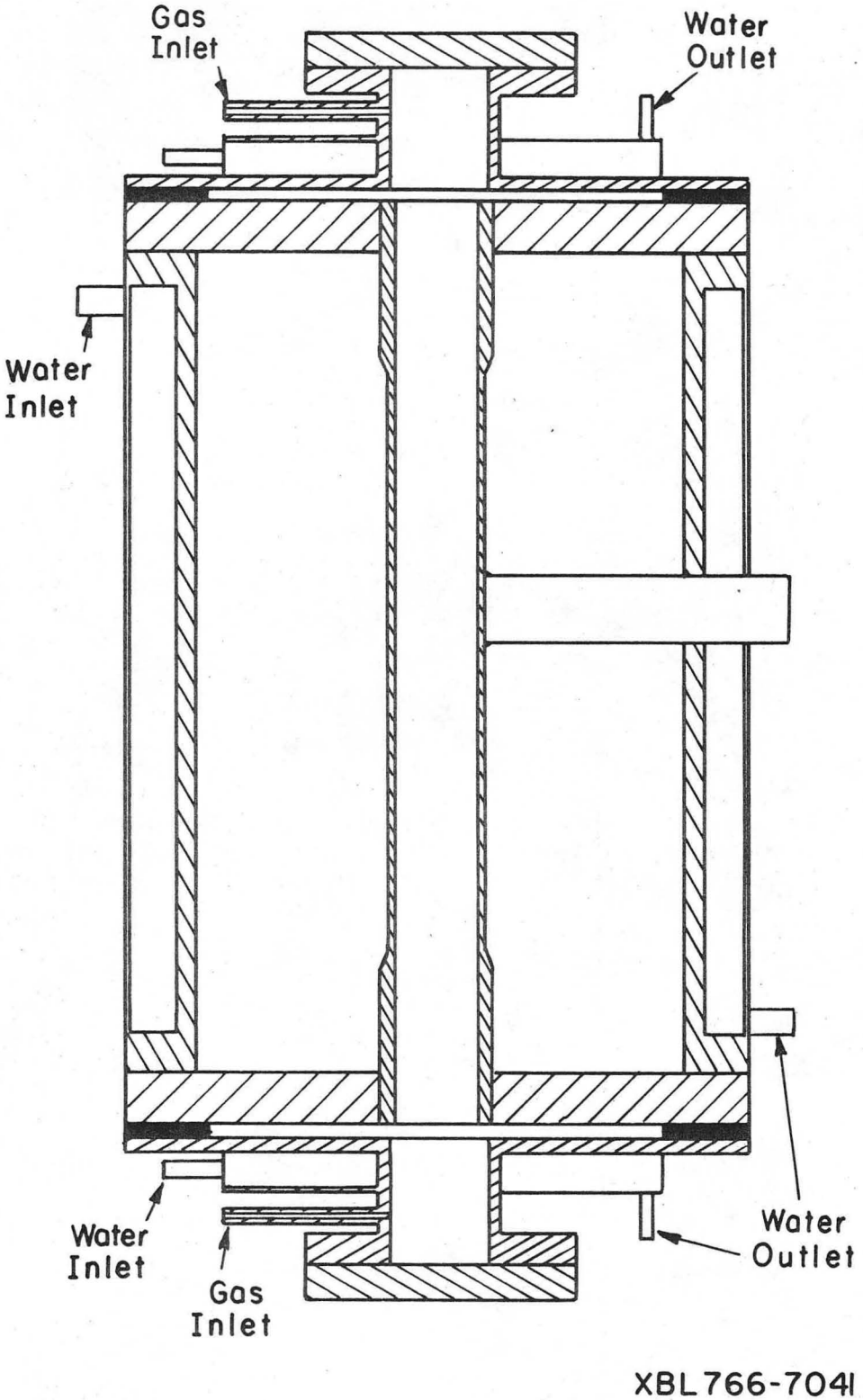
Gas
Inlet
Water
Outlet
Water
Inlet
Water
Inlet
Gas
Inlet
Water
Outlet
XBL766-7041

Figure IV. 1a

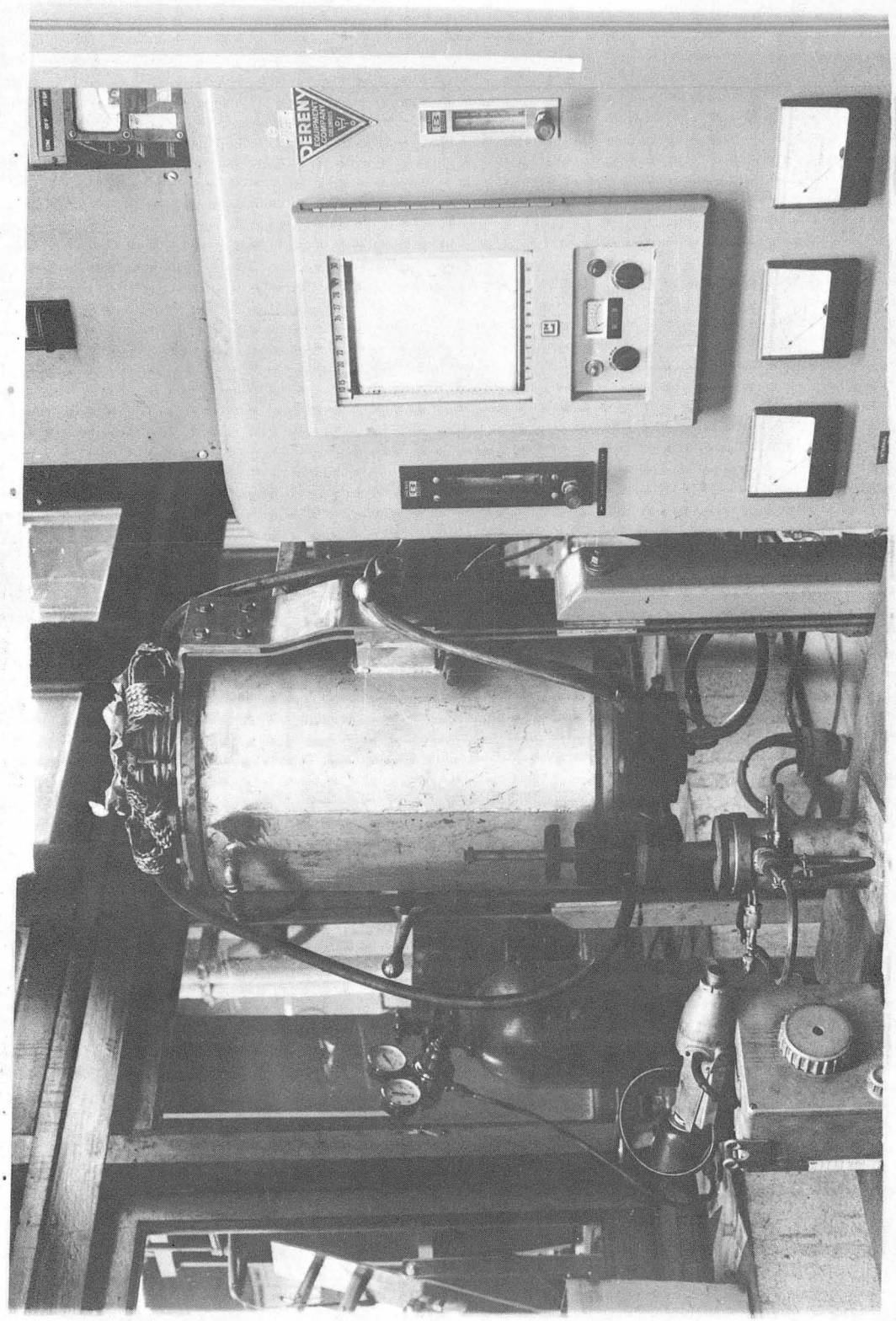

XBB 766-4679

Figure IV. 1b

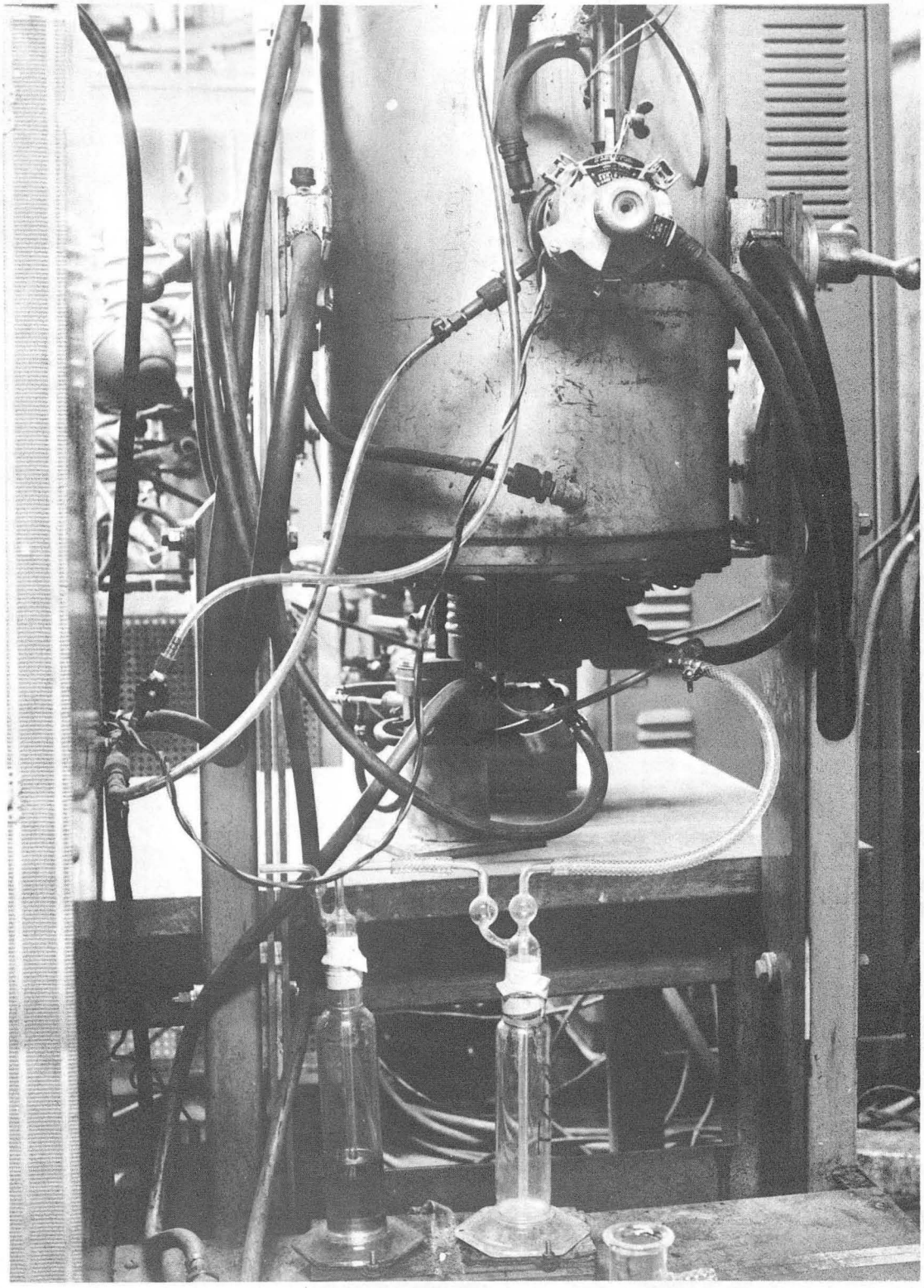

XBB 766-4678

Figure IV. 1c

XBB 766-4677

Figure IV. 2

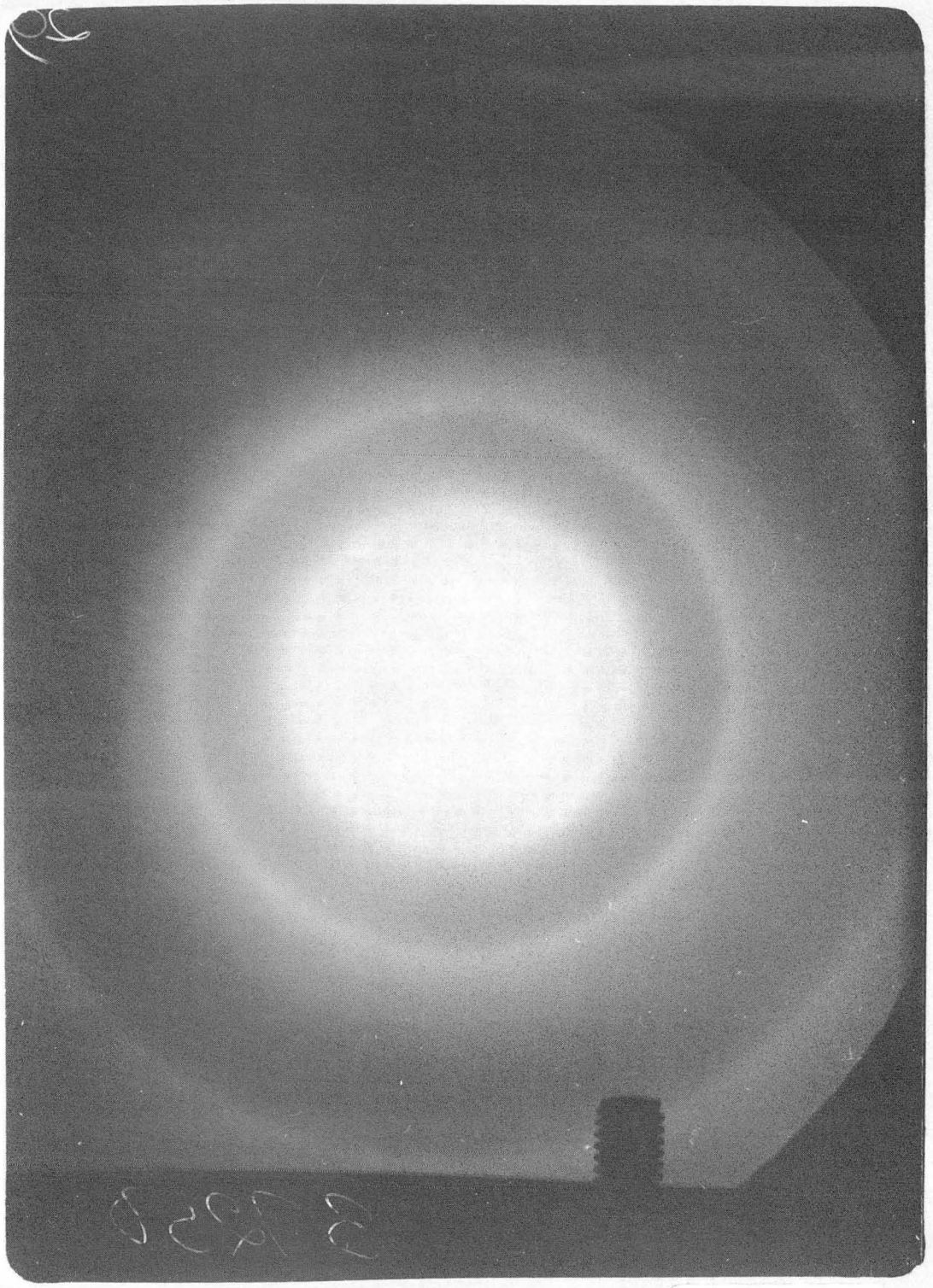

XBB 766-4686

Figure V. 1

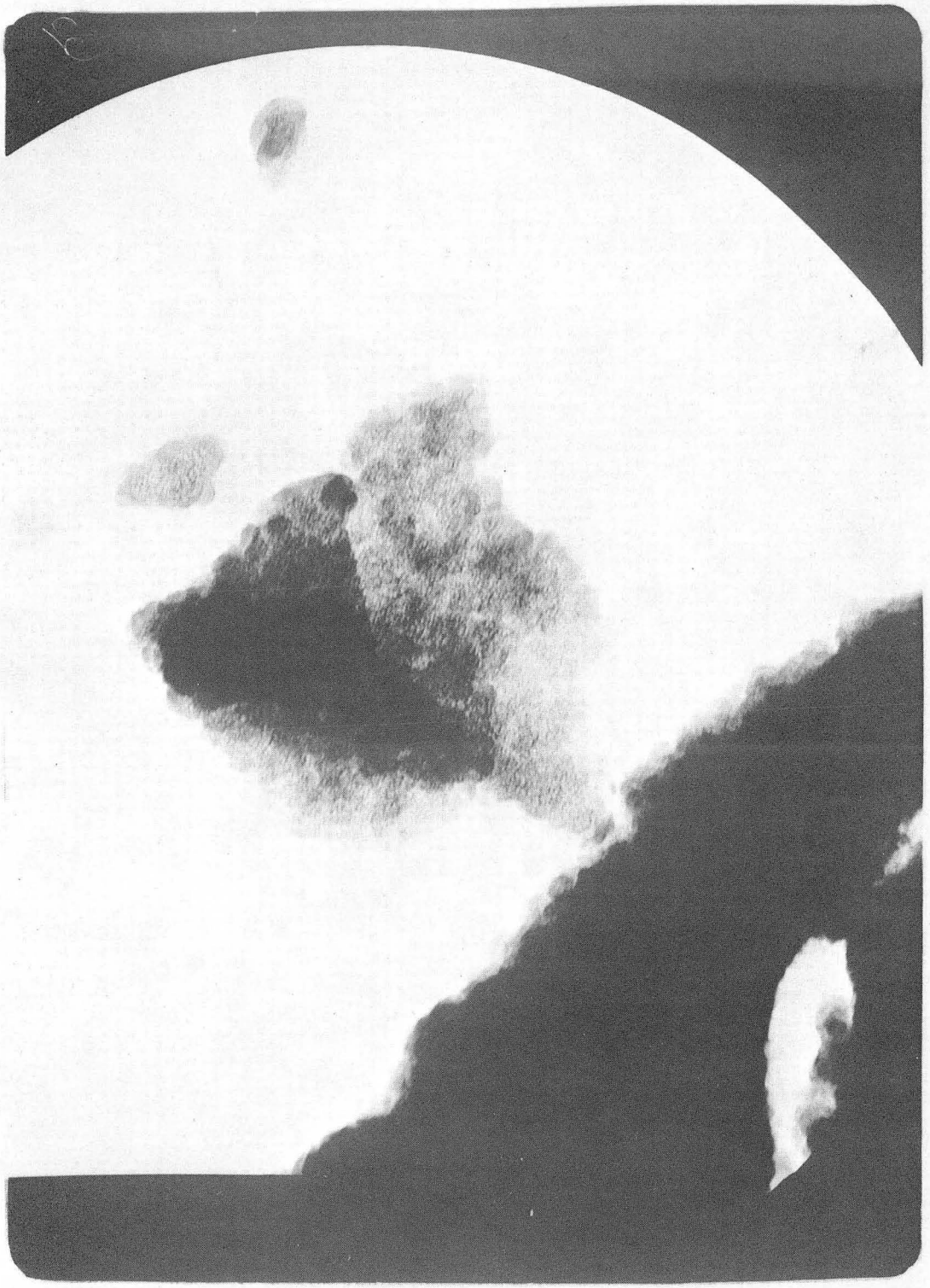

XBB 766-4680

Figure V. 2

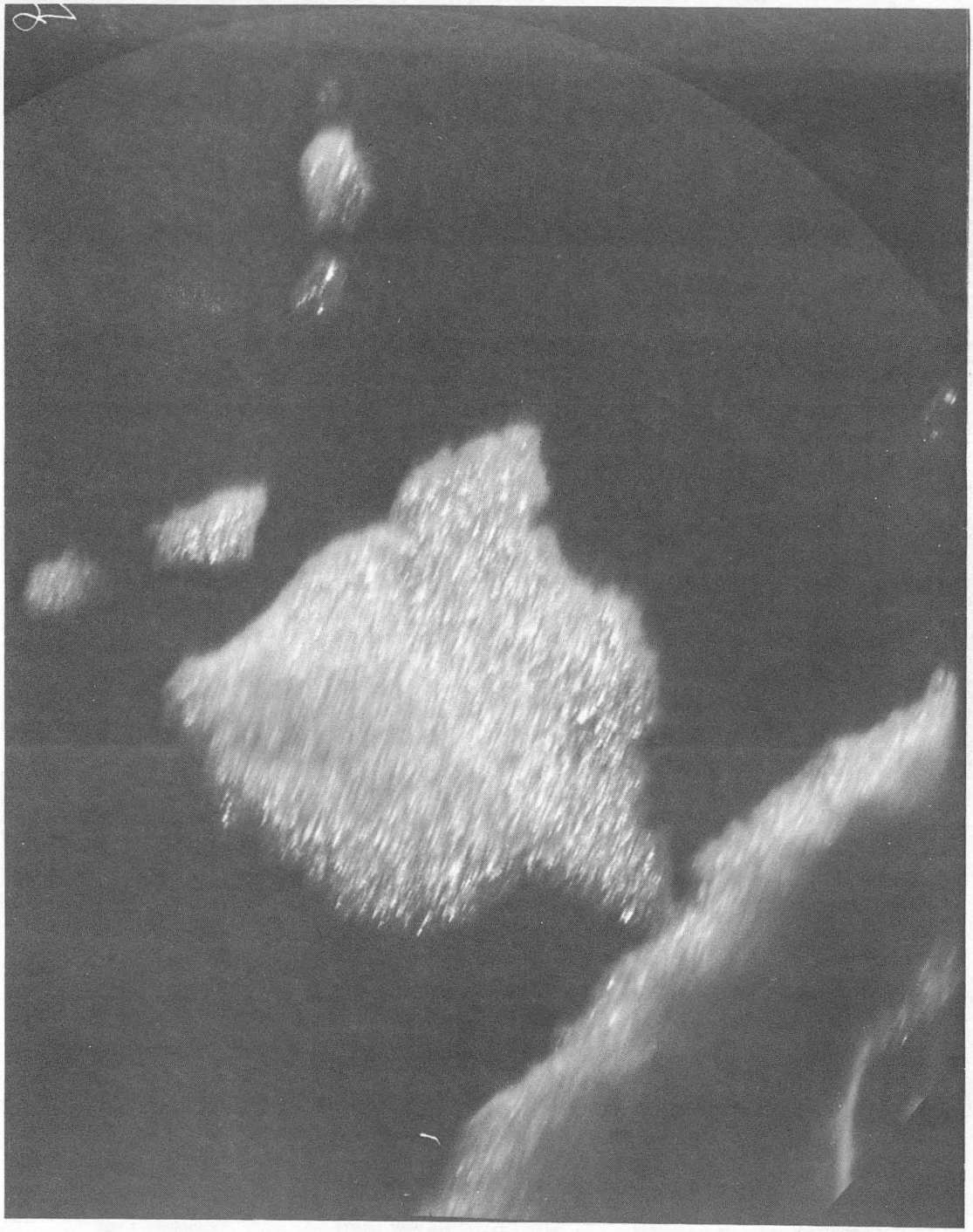

XBB 766-4684

Figure V. 3

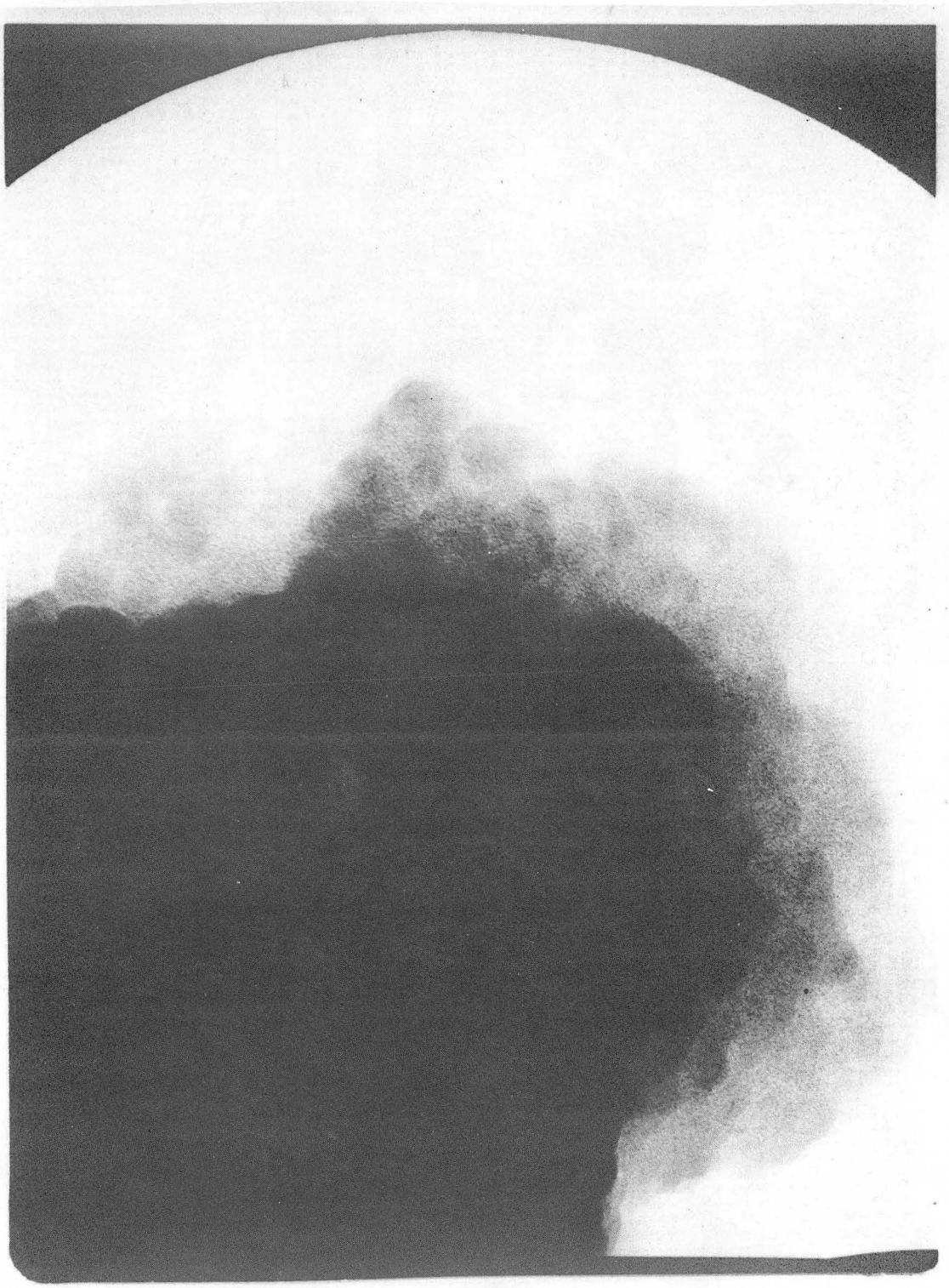

XBB 766-4690

Figure V. 4

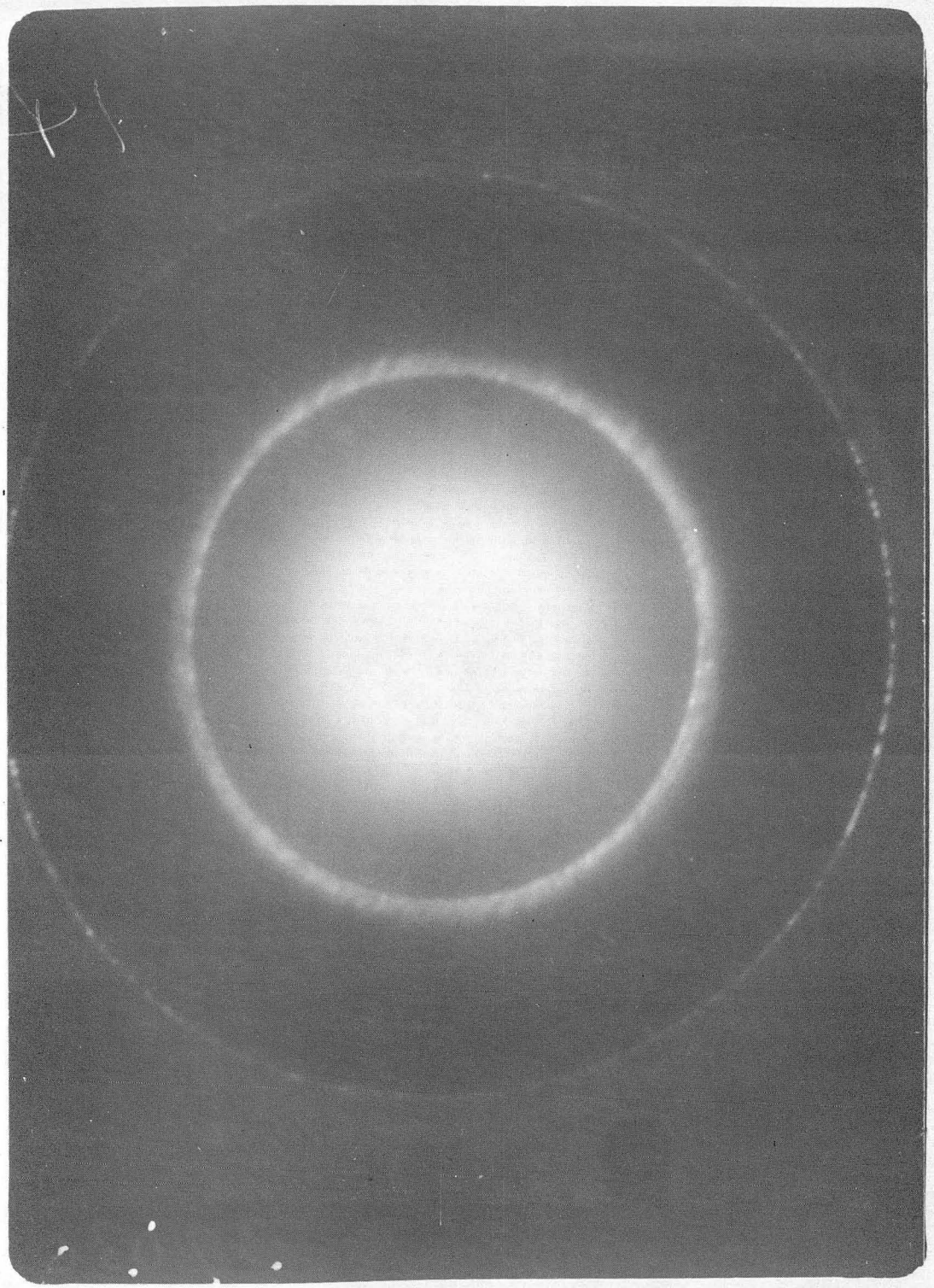

XBB 766-4687

Figure V. 5

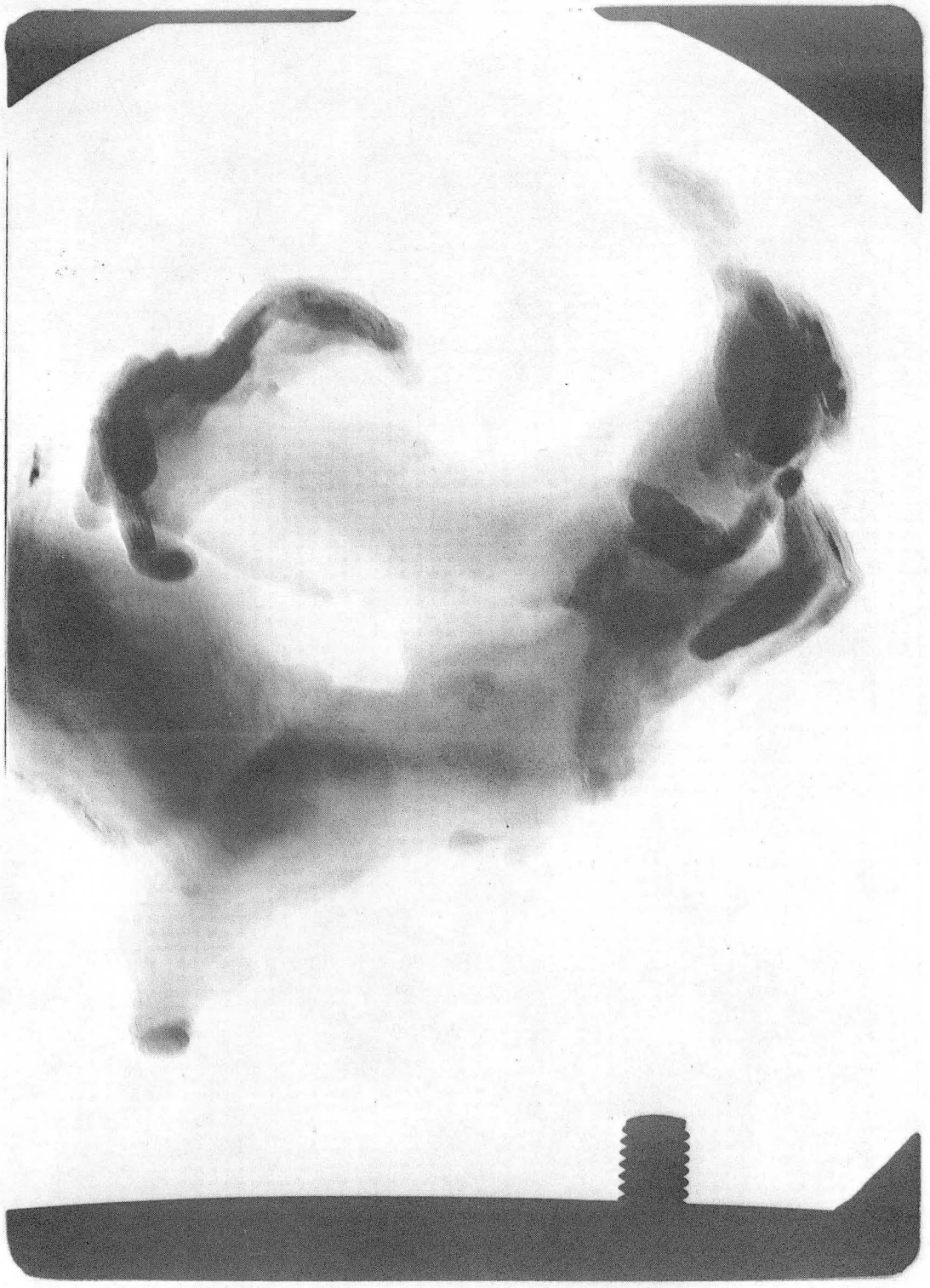

XBB 766-4681

Figure V. 6

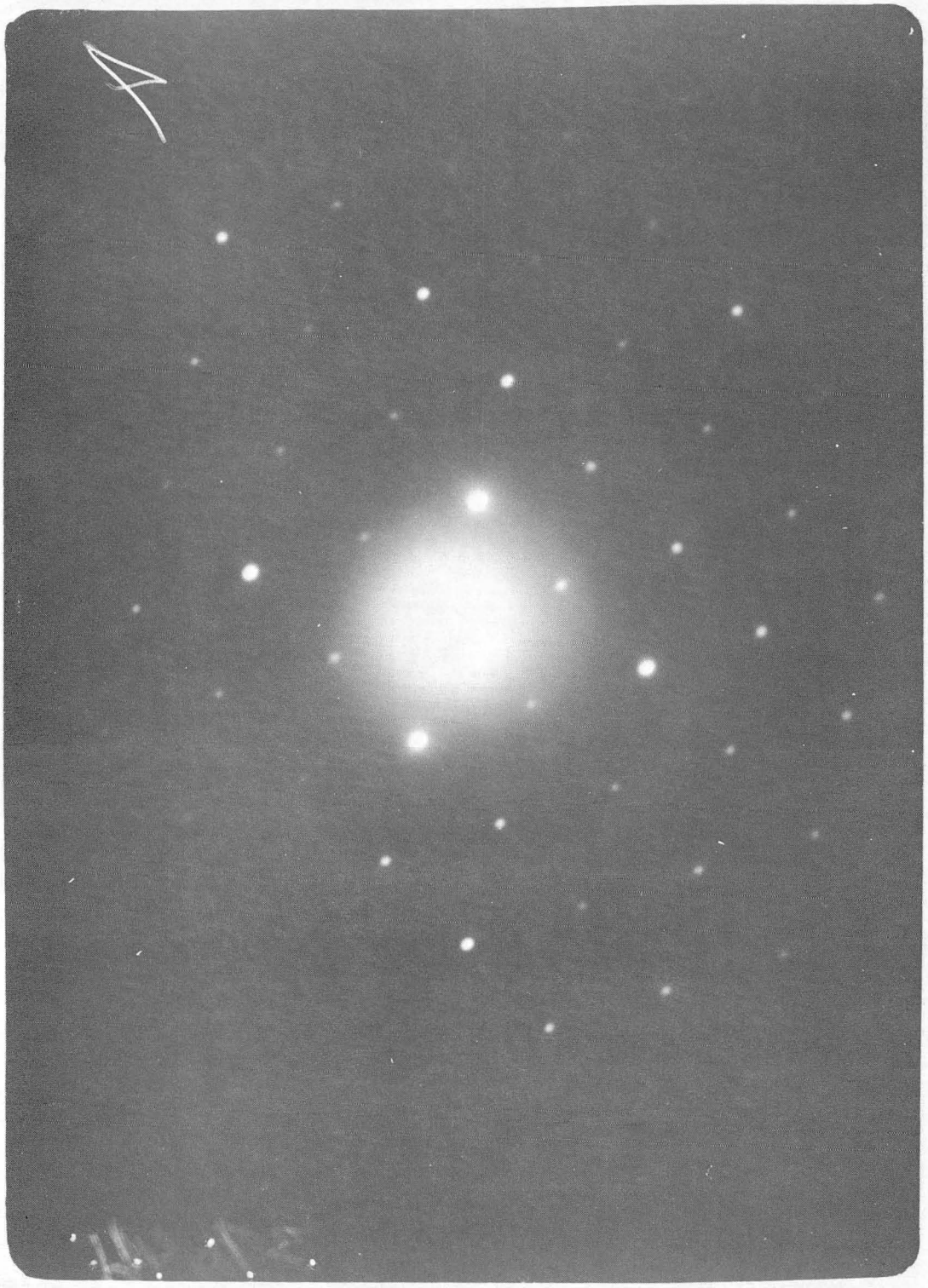

XBB 766-4683

Figure V. 7

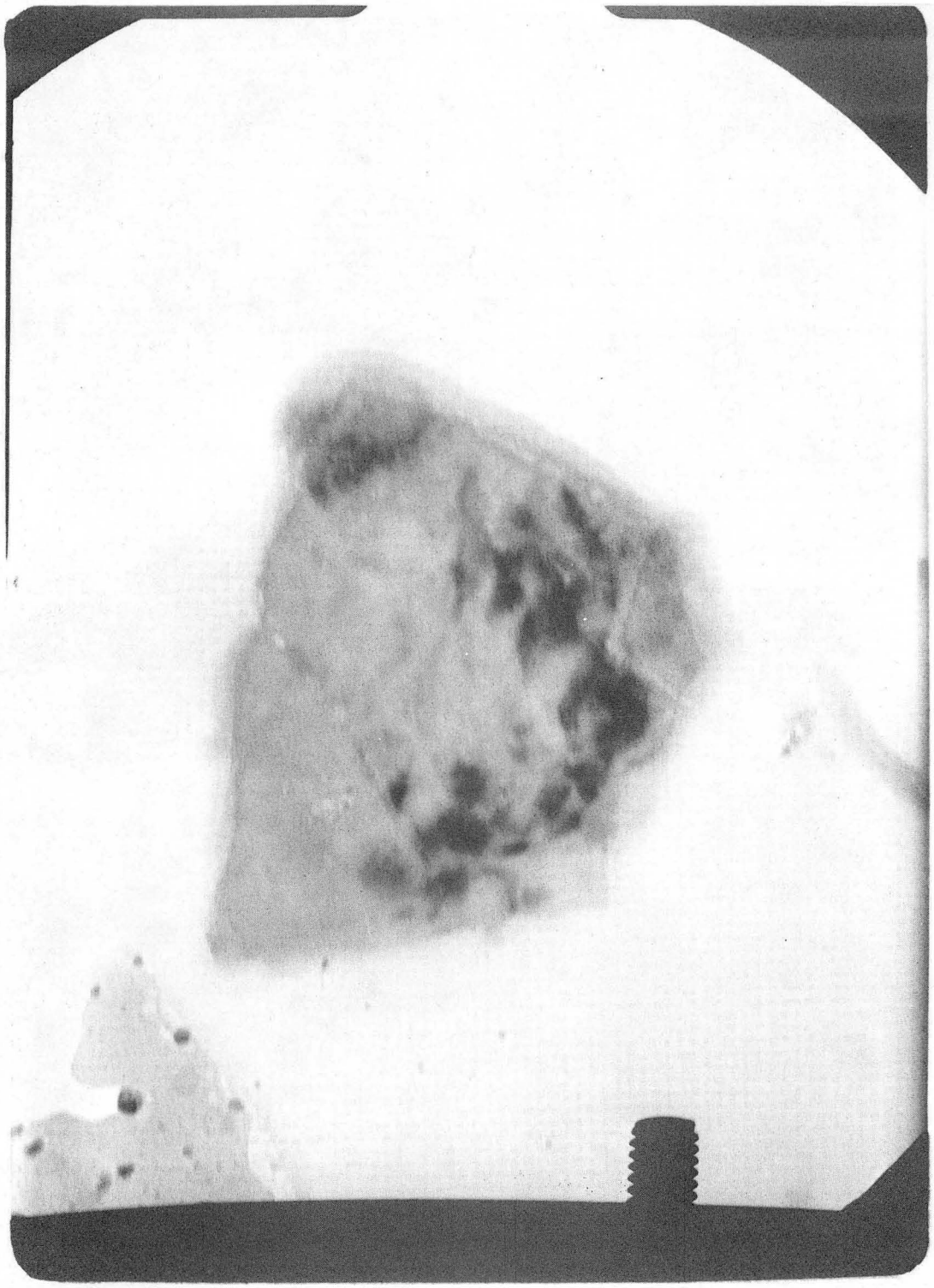

XBB 766-4689

Figure V. 8

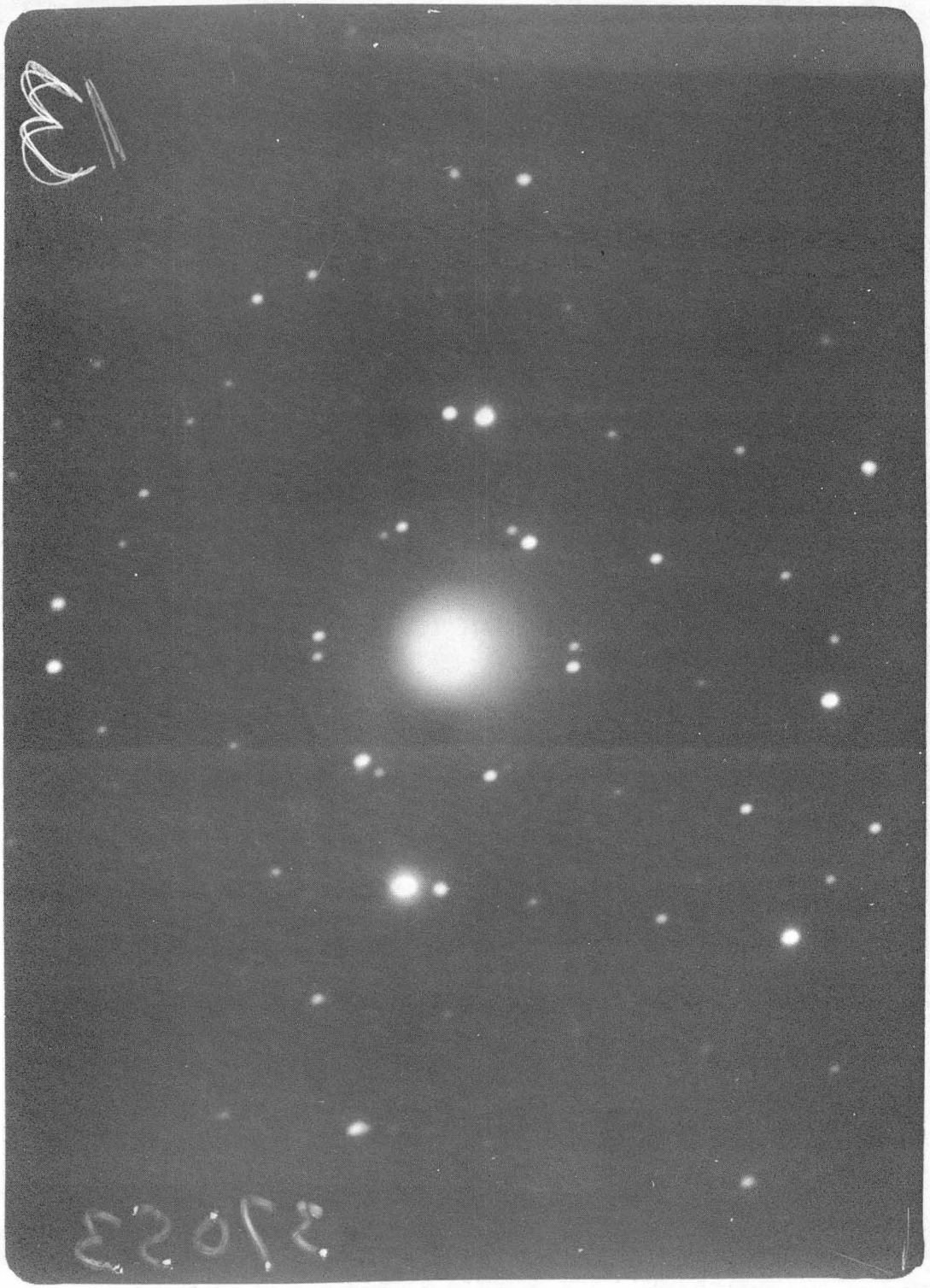

XBB 766-4682

Figure V. 9

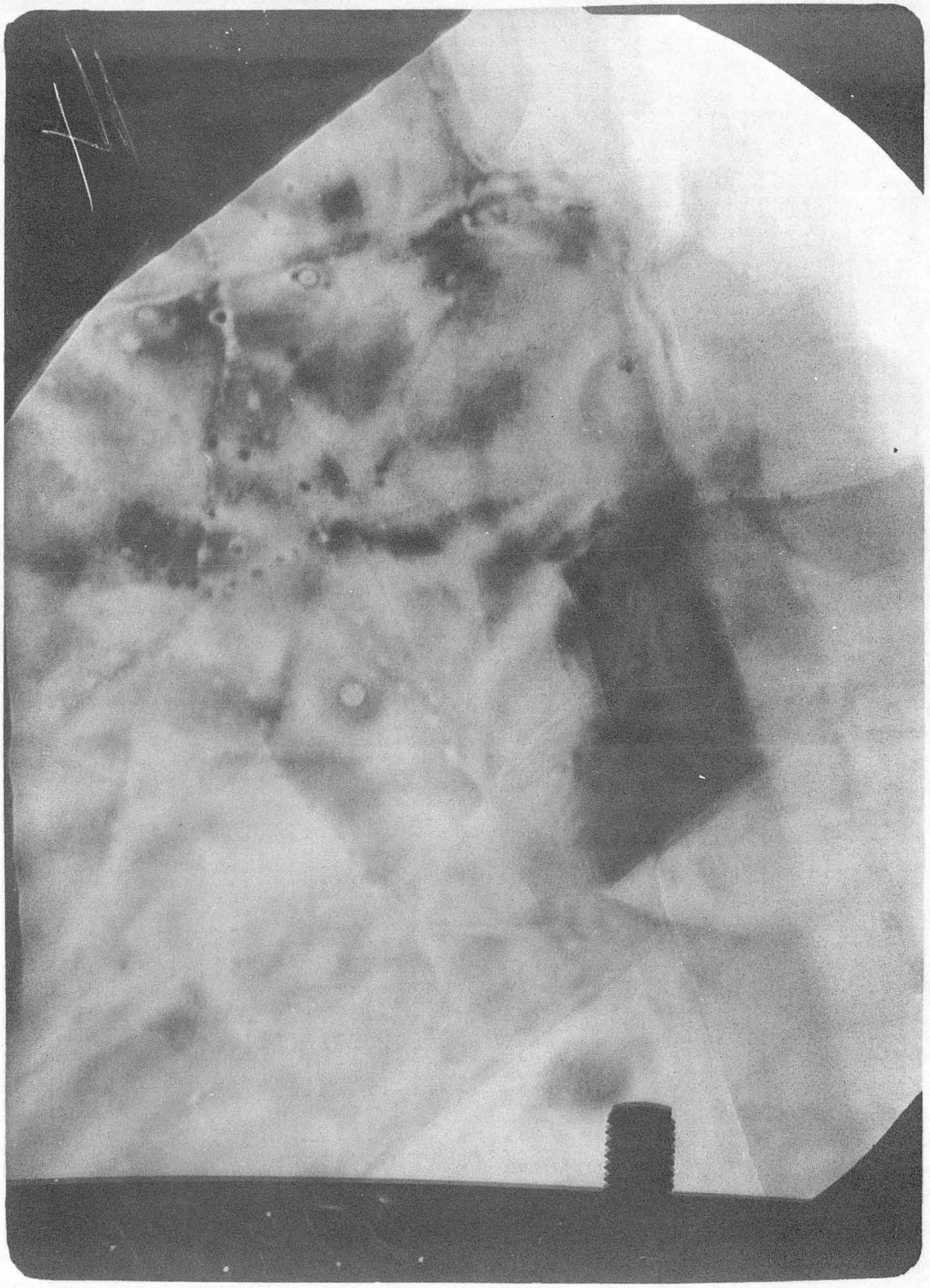

XBB 766-4688

Figure V. 10

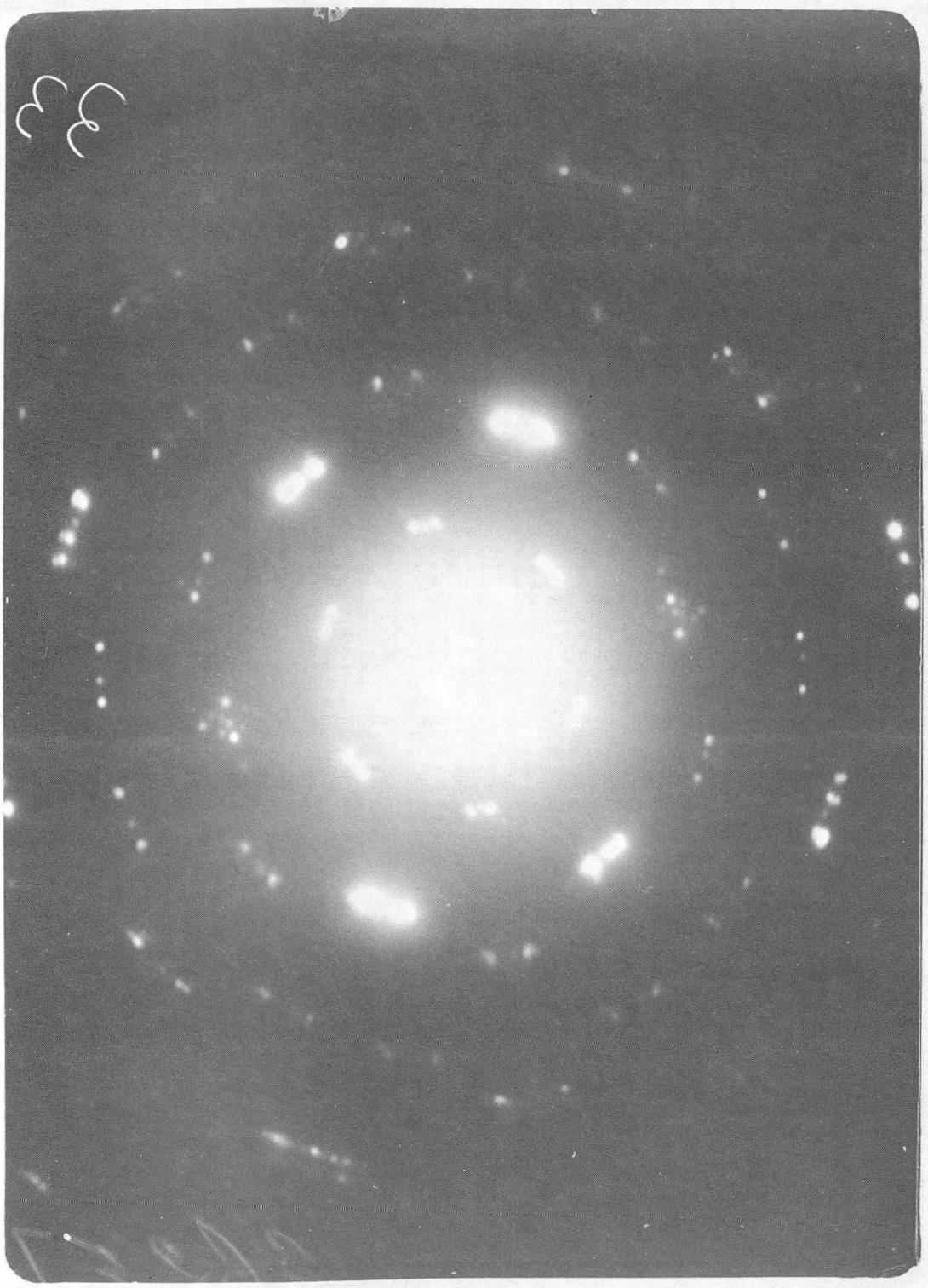

XBB 766-4685

Figure V. 11

XBB 766-4691

Figure V. 12 a

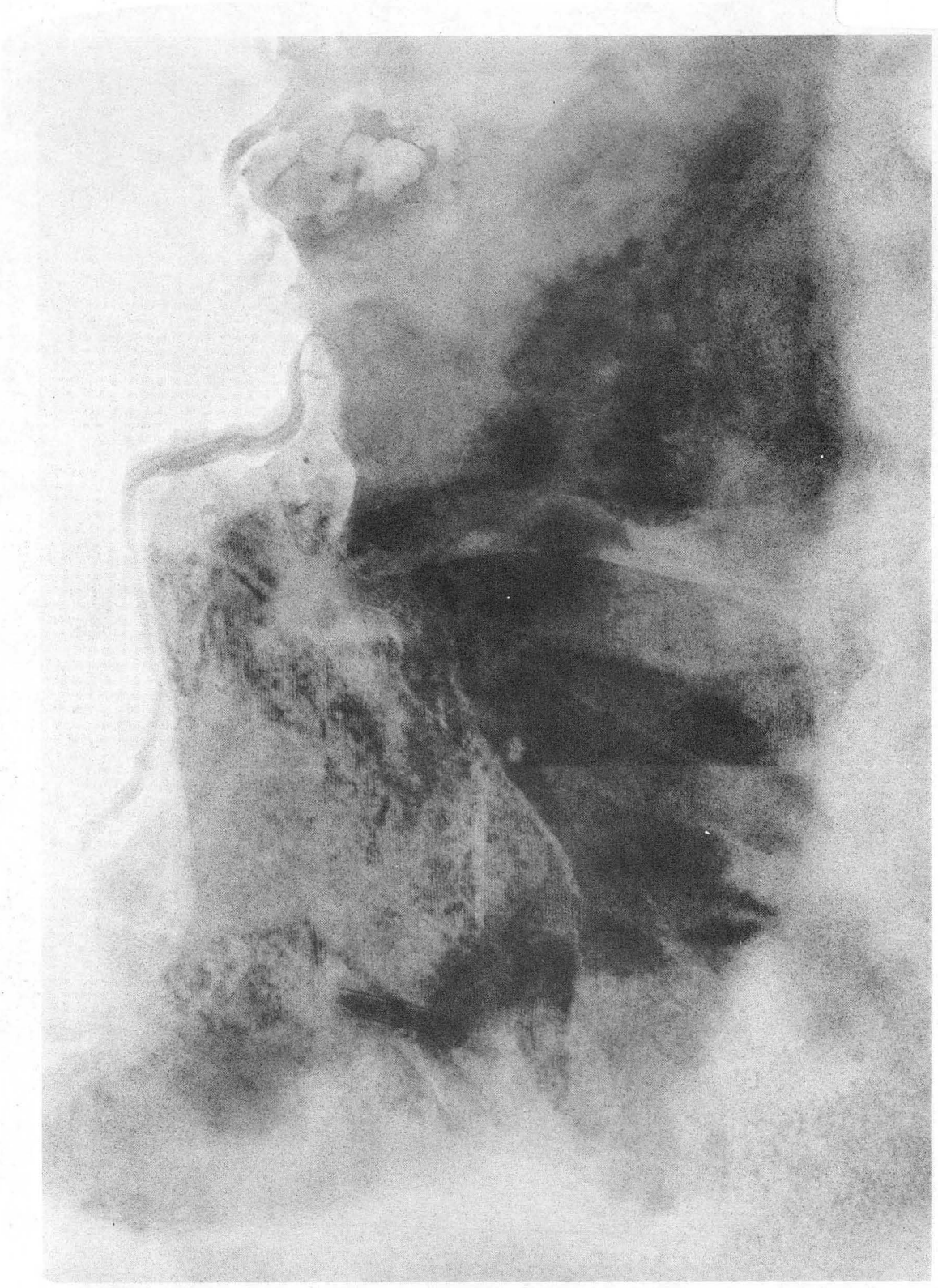

XBB 766-4691A

Figure V. 12 b

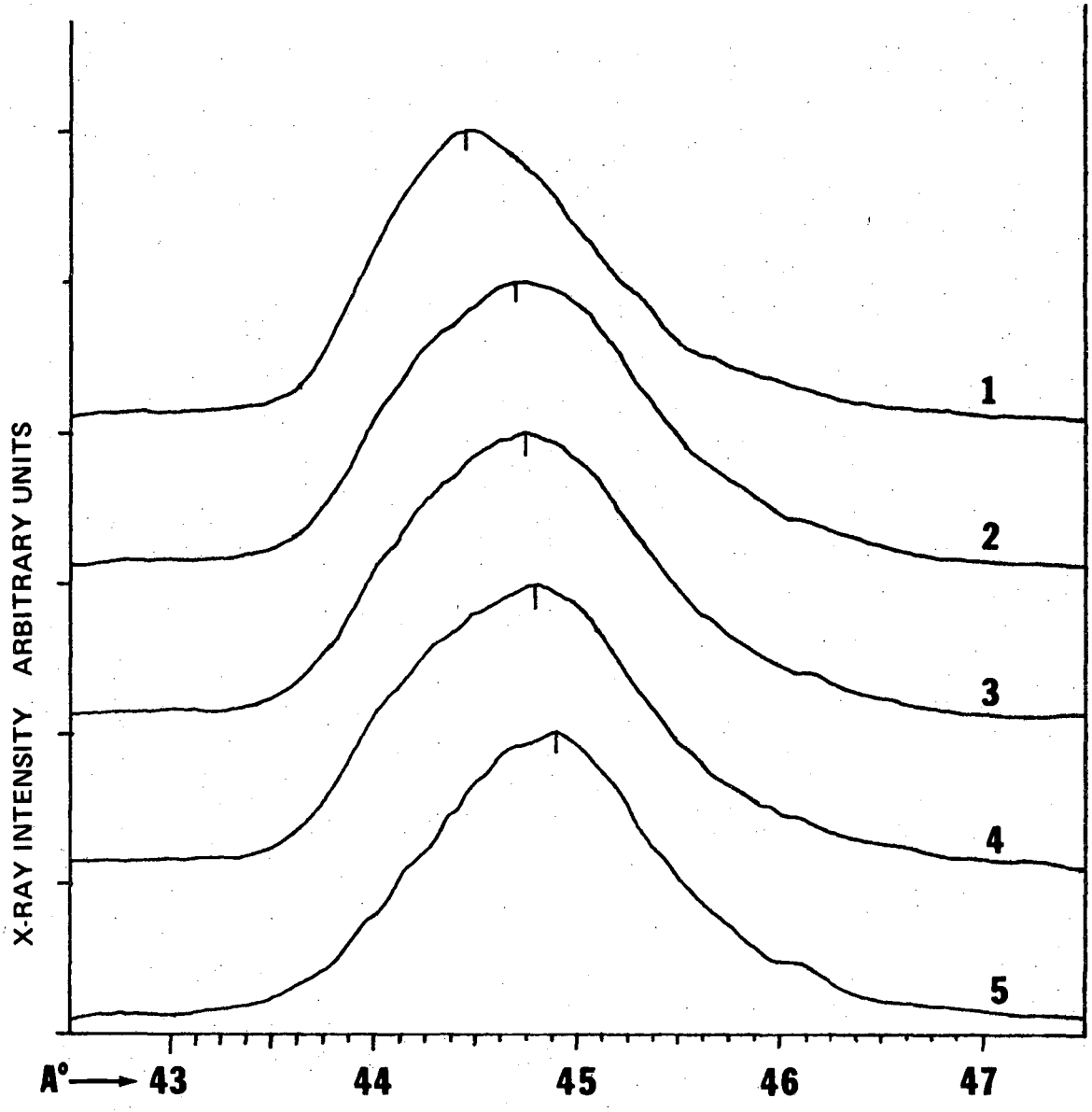

XBL 735-6196

Figure VI. 1

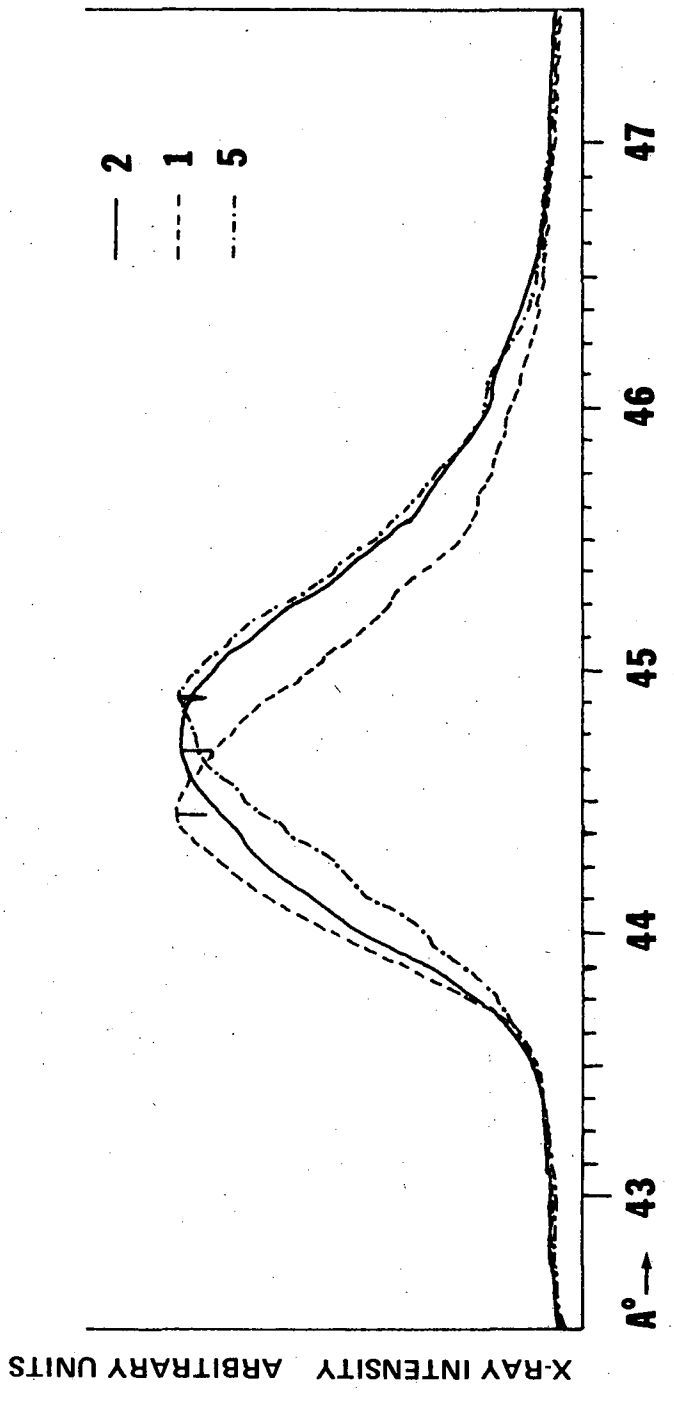

XBL 735-6211

Figure VI. 2

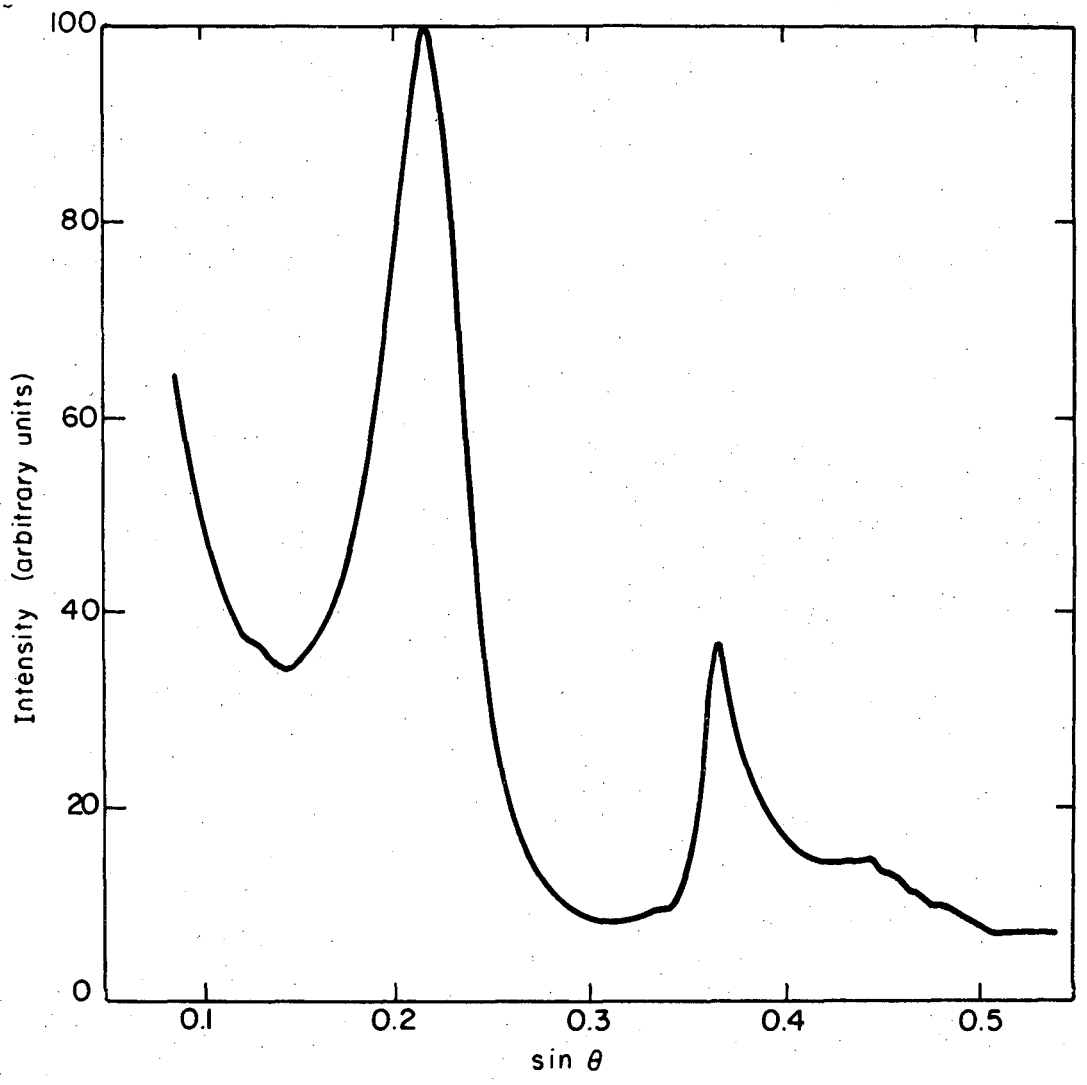

XBL 765-6897

Figure VII. 1

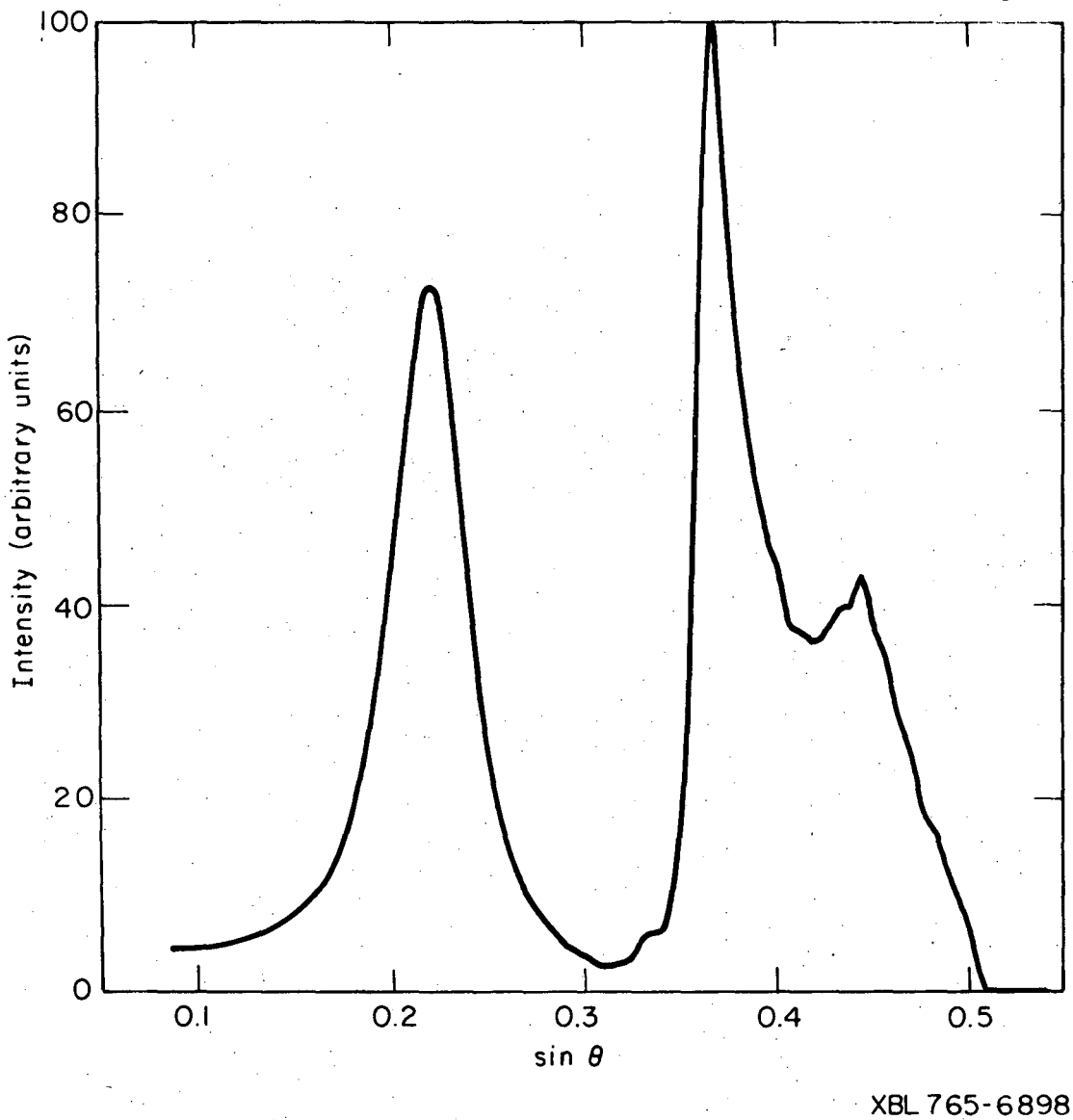
100
80
60
40
20
0
Intensity (arbitrary units)
0.1
0.2
0.3
0.4
0.5
sin θ
XBL 765-6898

Figure VII. 2

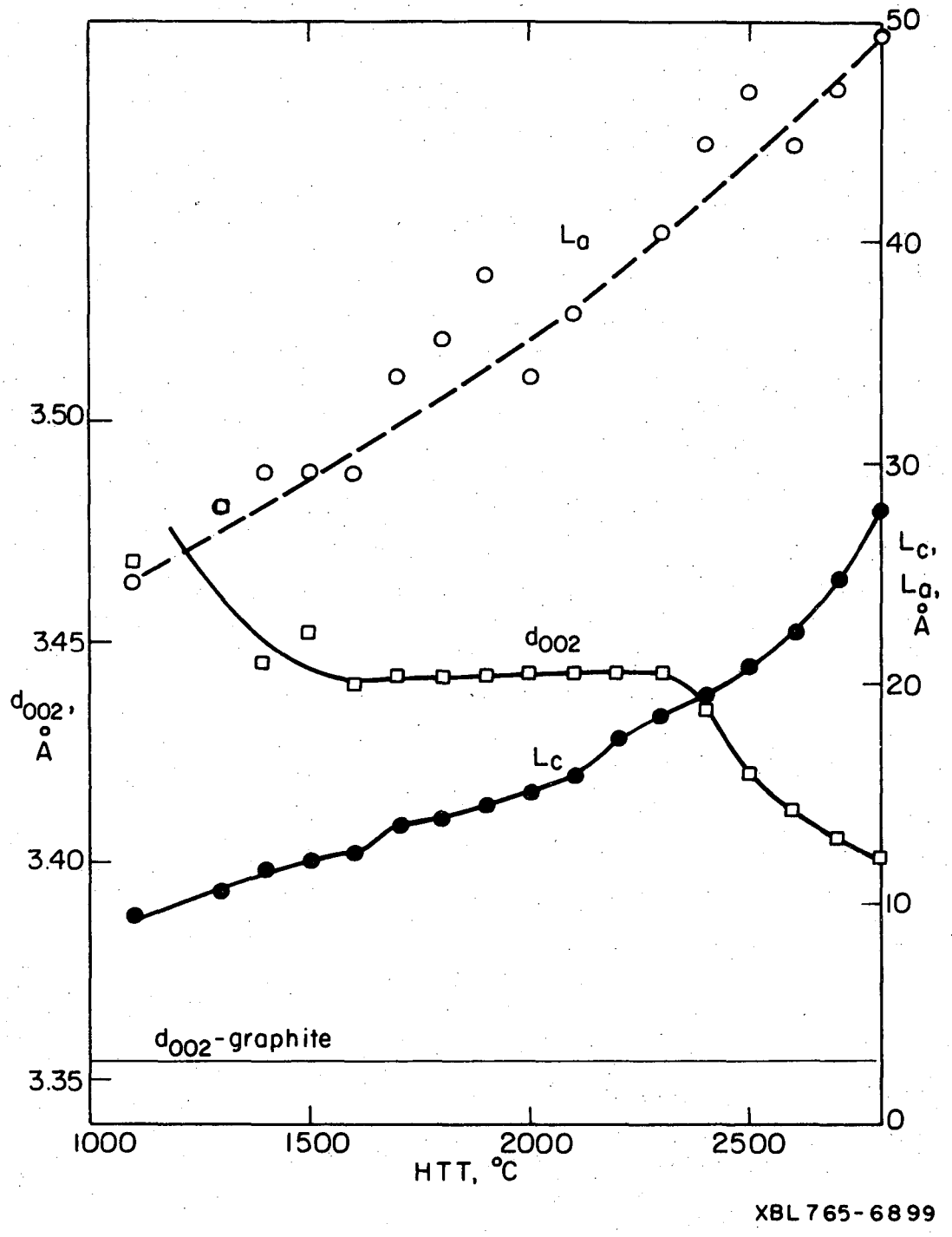

Figure VII. 3

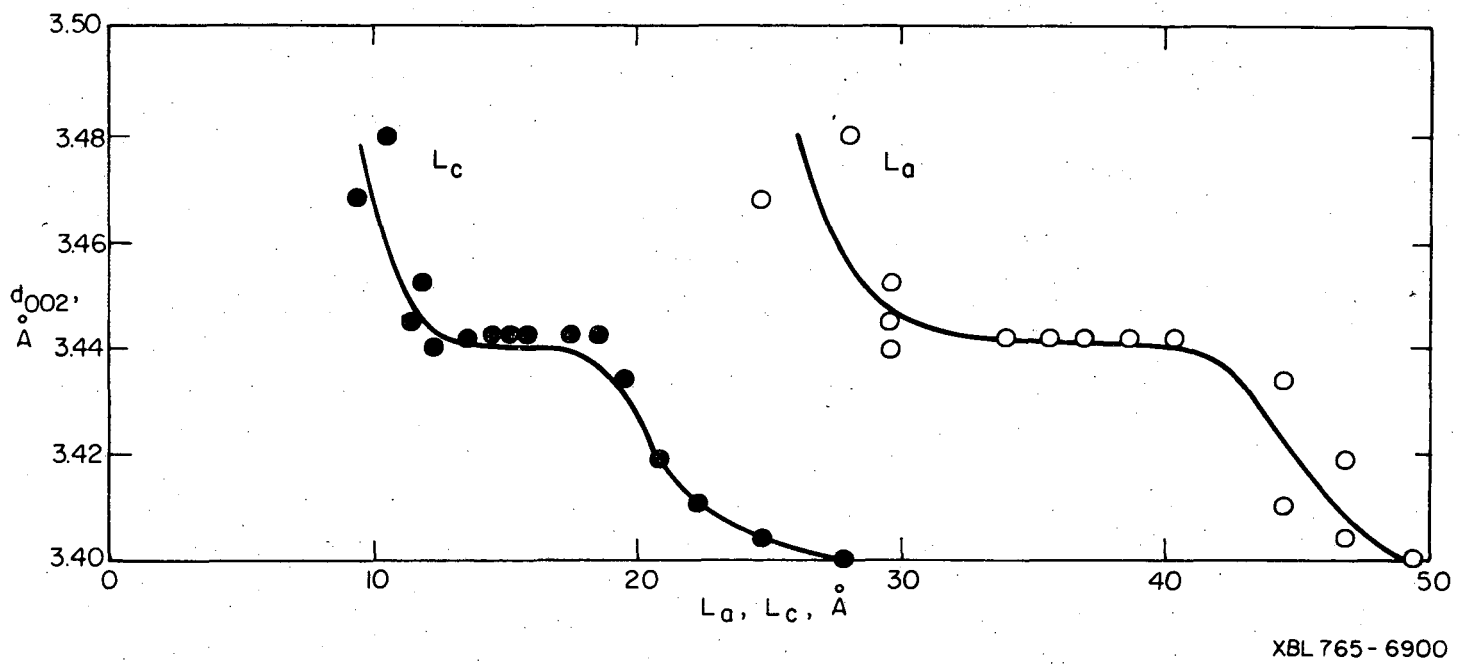
3.50
3.48
3.46
3.44
3.42
3.40
d_{002}, Å
L_c
L_a
0
10
20
30
40
50
L_a, L_c, Å
XBL 765-6900

Figure VII. 4

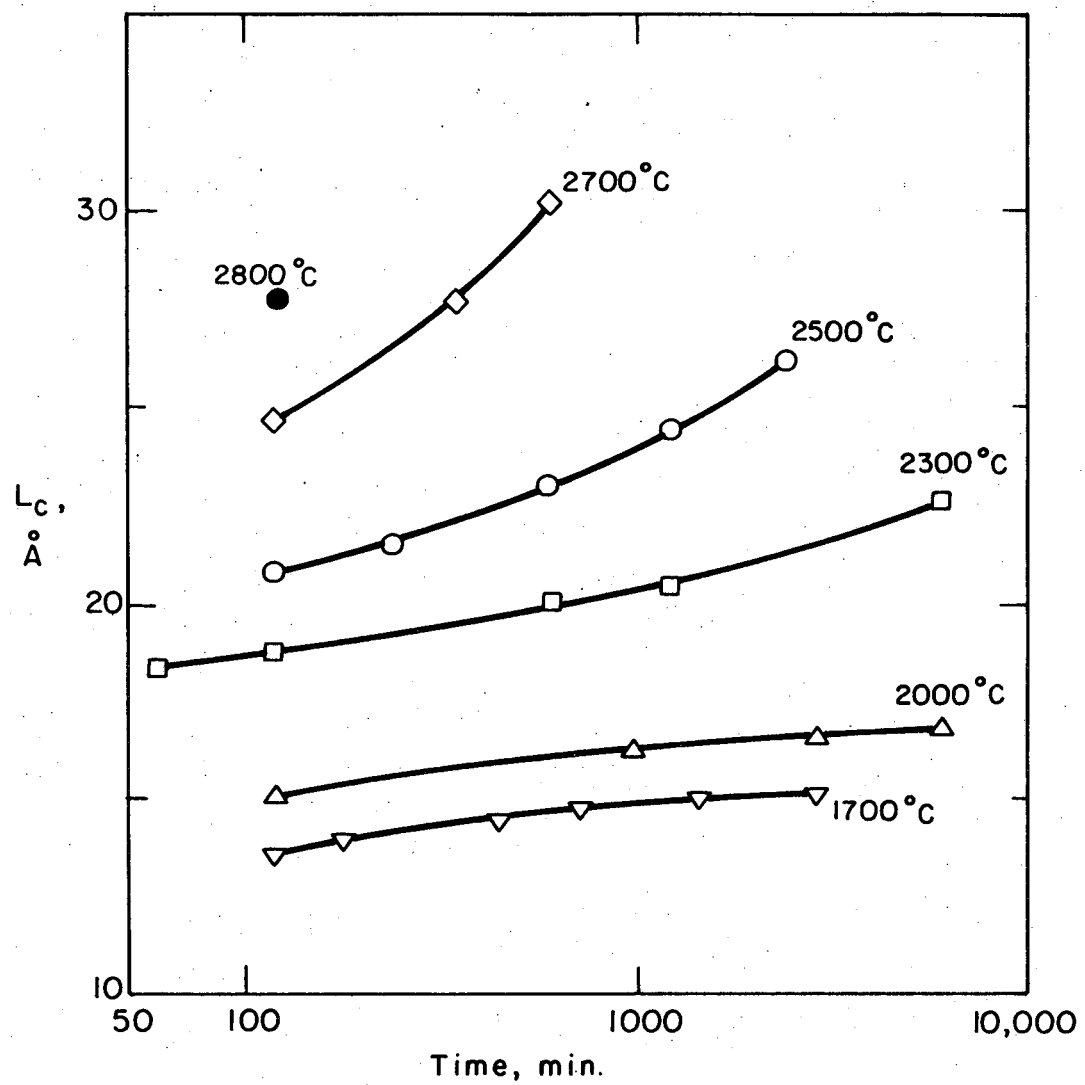

XBL 765-6901

Figure VII. 5

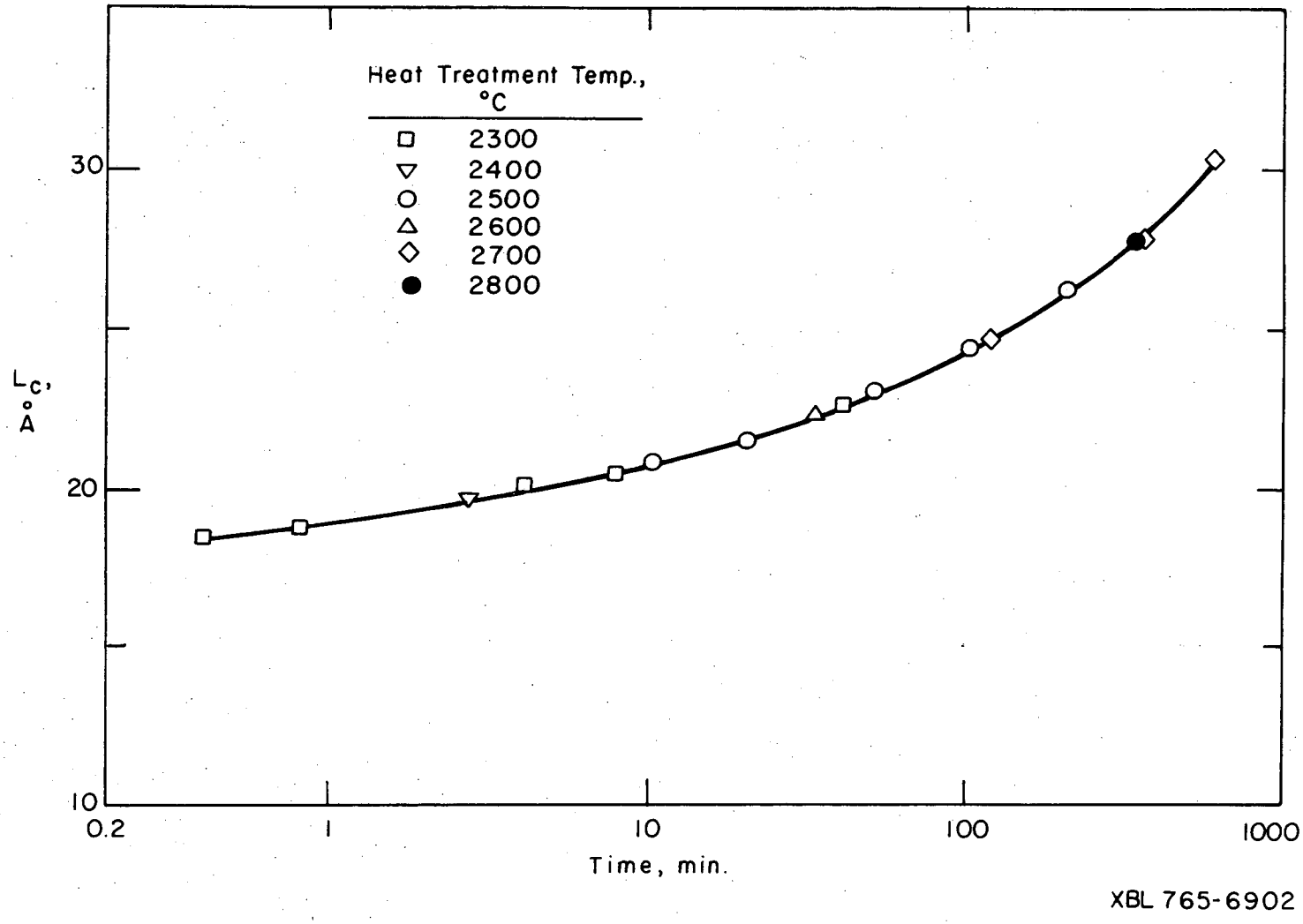
Heat Treatment Temp., °C
2300
2400
2500
2600
2700
2800
30
20
10
L_c, Å
0.2
1
10
100
1000
Time, min.
XBL 765-6902

Figure VII. 6

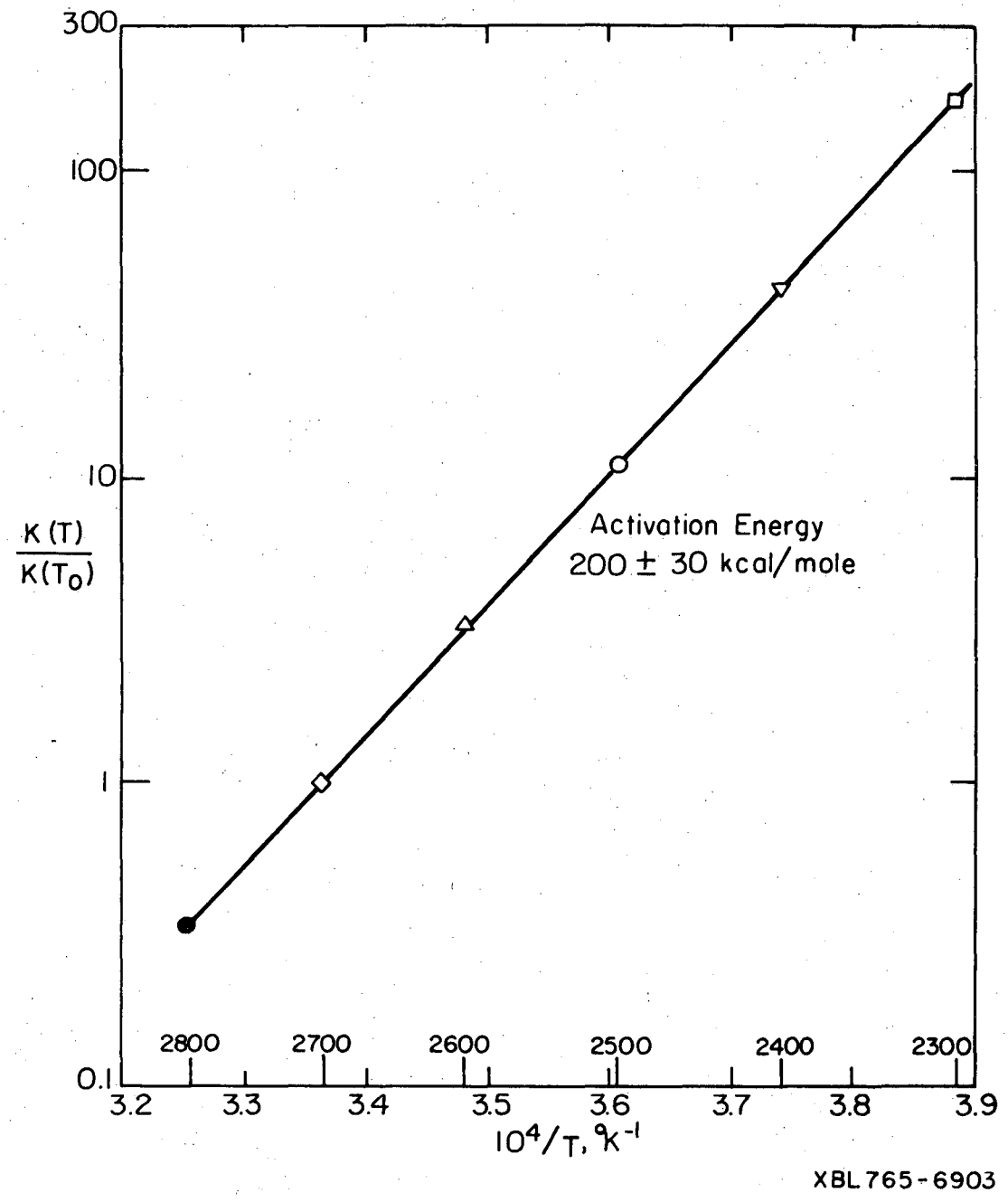

Figure VII. 7

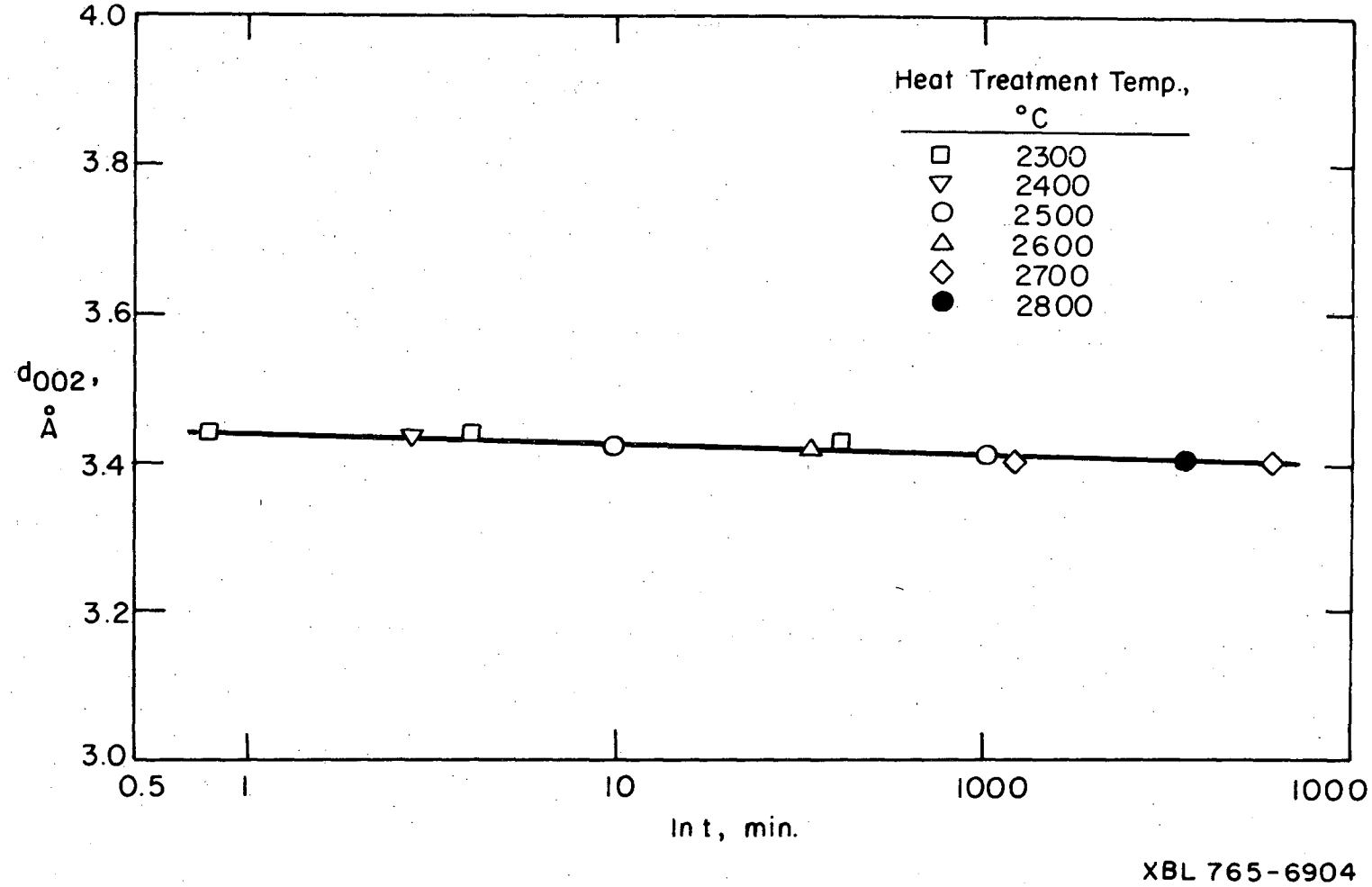
4.0
3.8
3.6
3.4
3.2
3.0
d_{002}, Å
0.5
1
10
1000
1000
ln t, min.
Heat Treatment Temp., °C
2300
2400
2500
2600
2700
2800
XBL 765-6904

Figure VII. 8

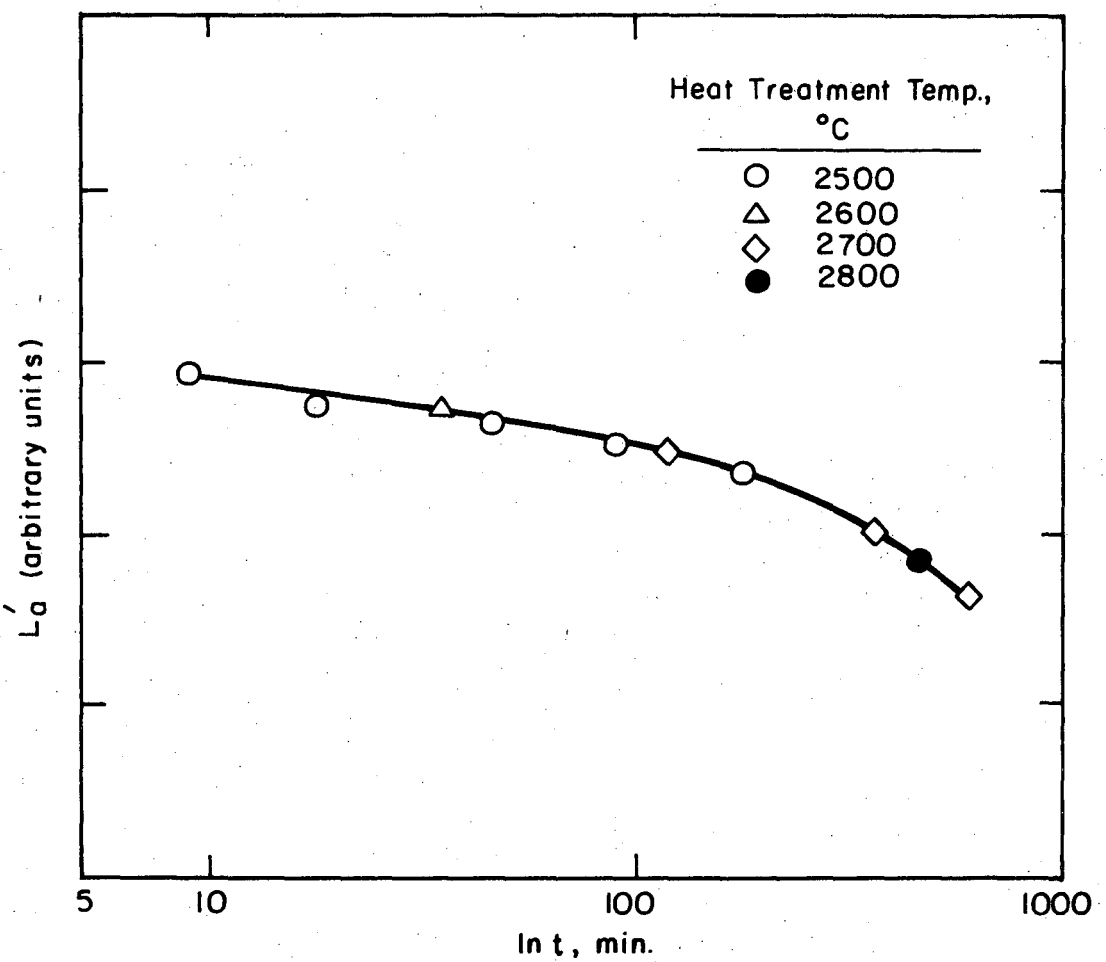

XBL 765-6905

Figure VII. 9

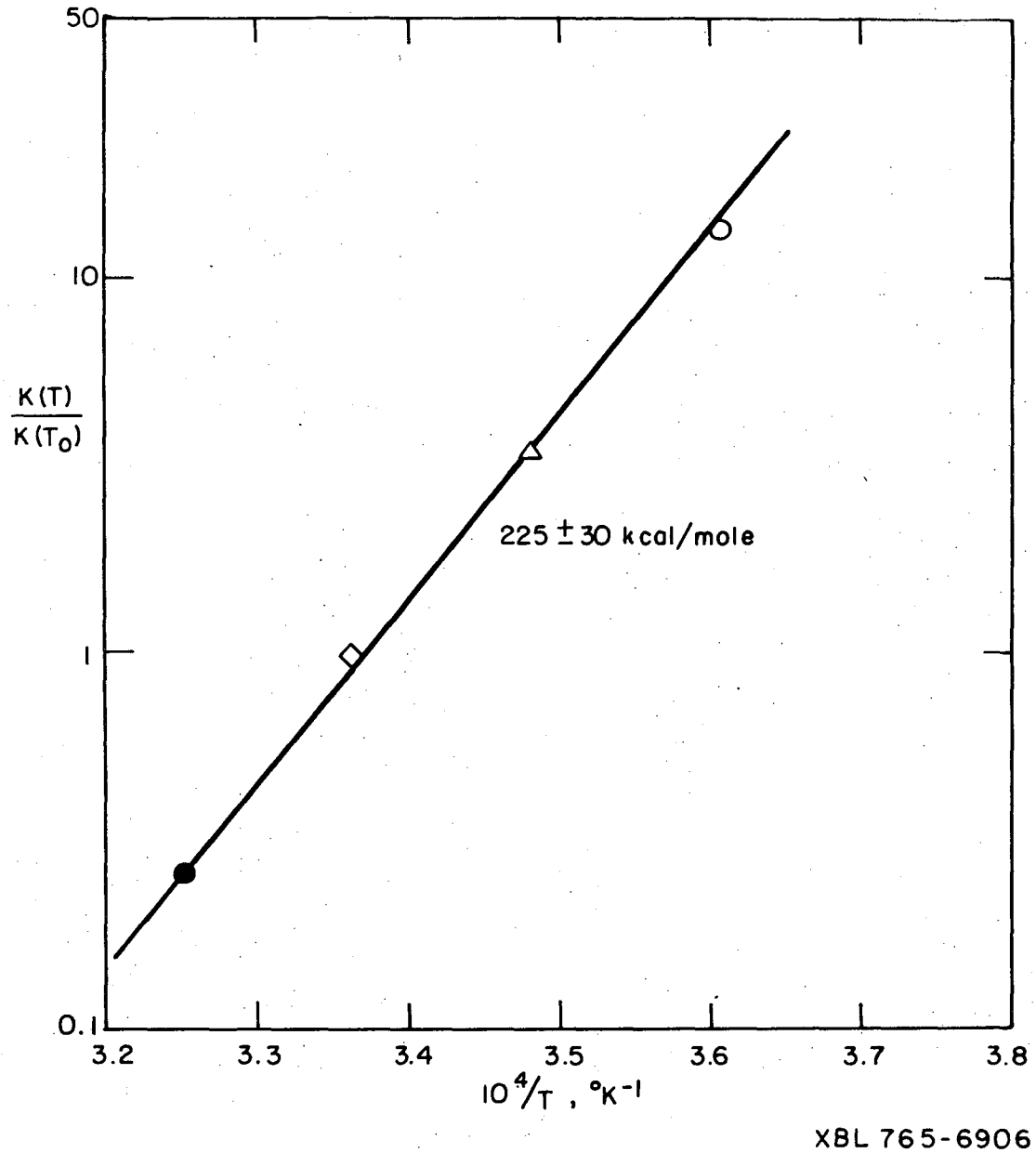

Figure VII. 10

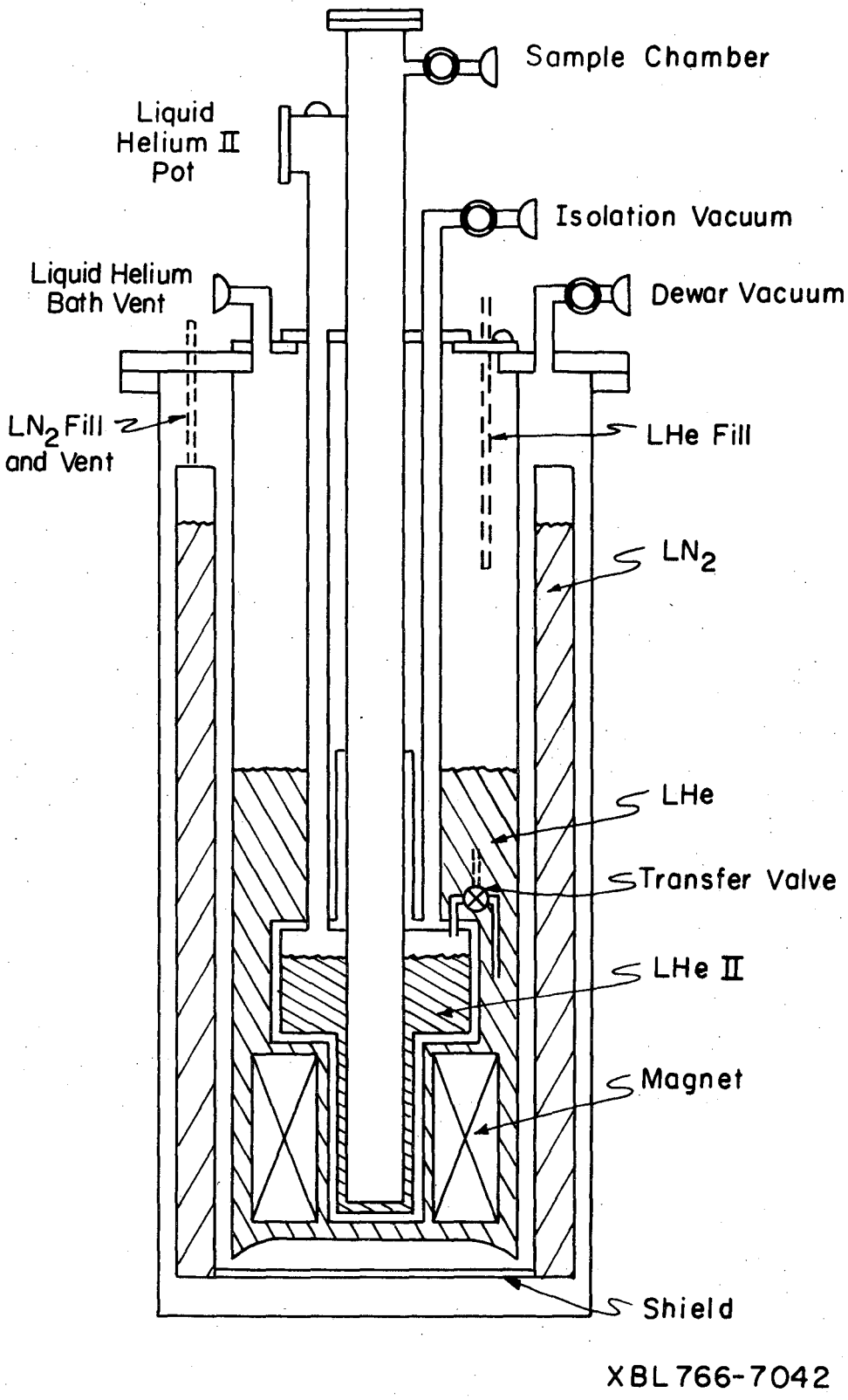

Figure VIII. 1

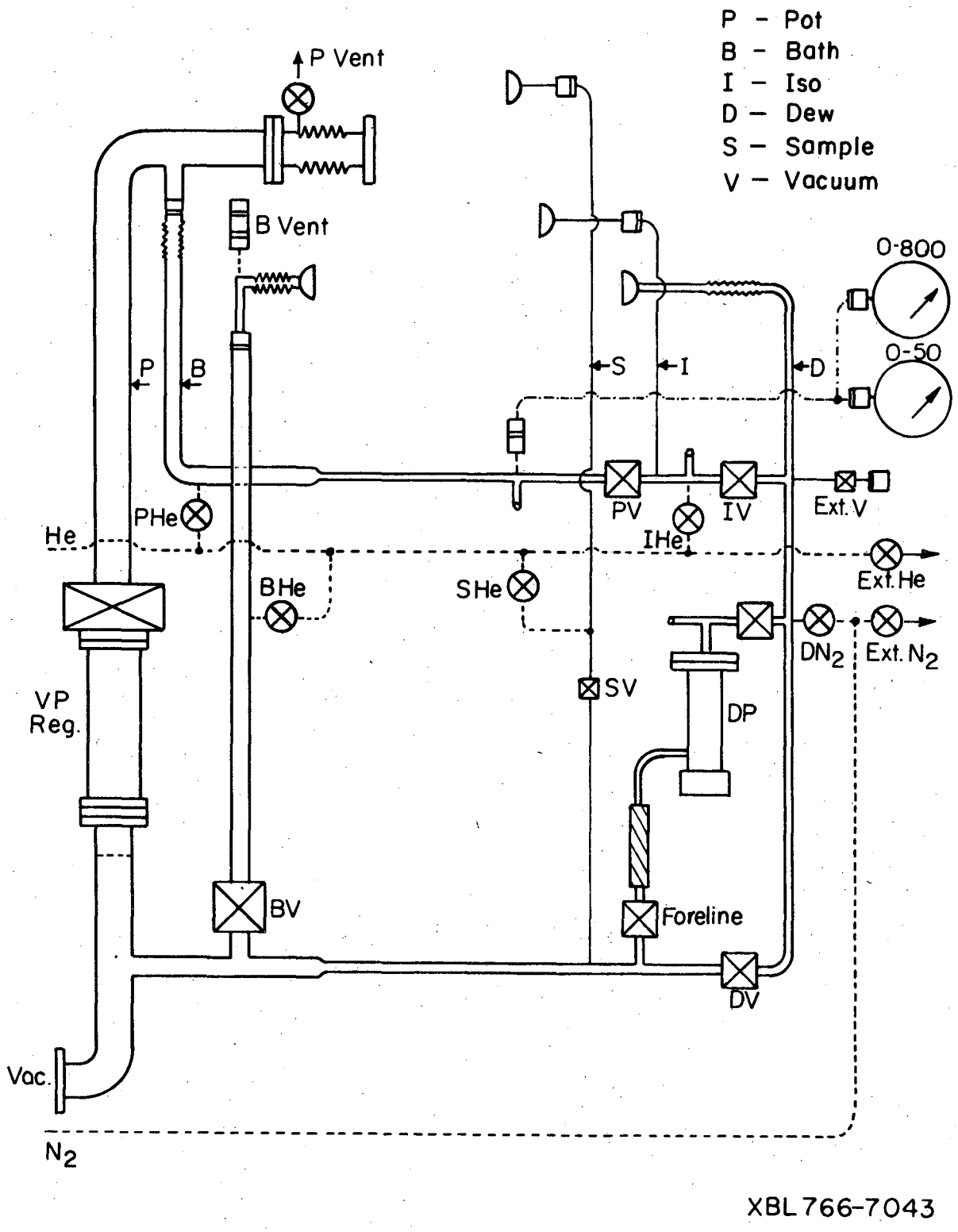

Figure VIII. 2a

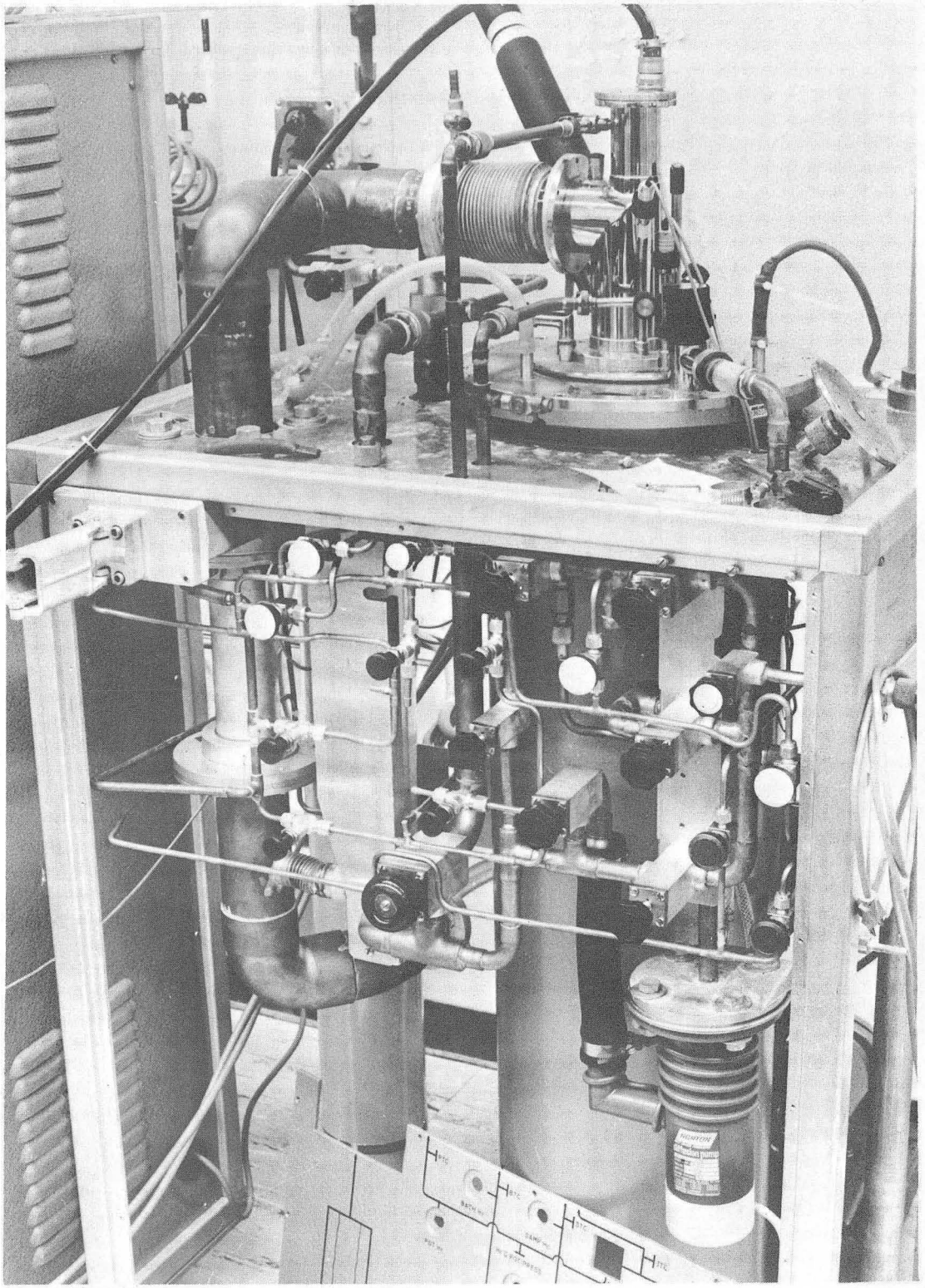

XBB 766-5191

Figure VIII. 2b

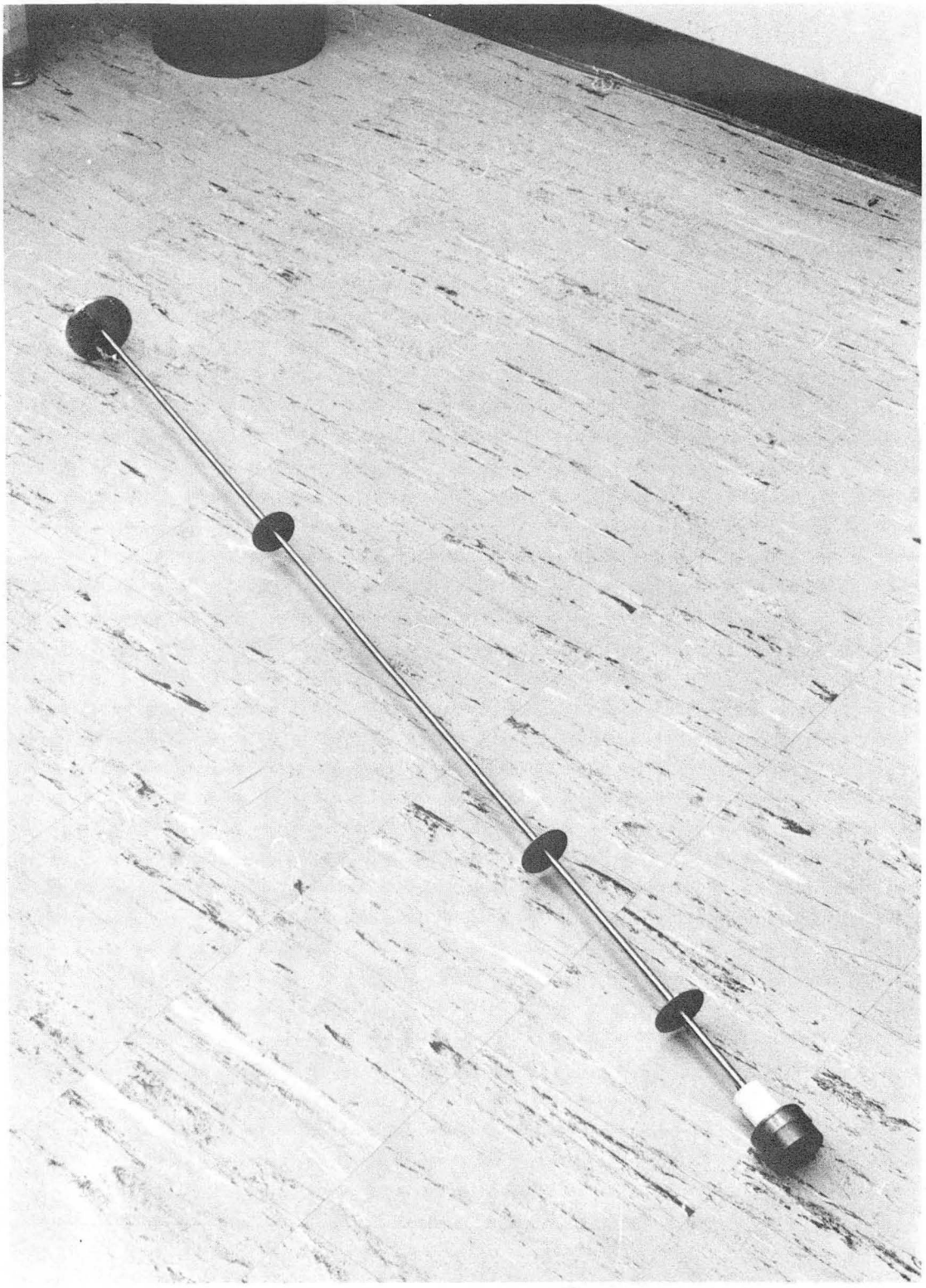

XBB 766-4676

Figure VIII. 3a

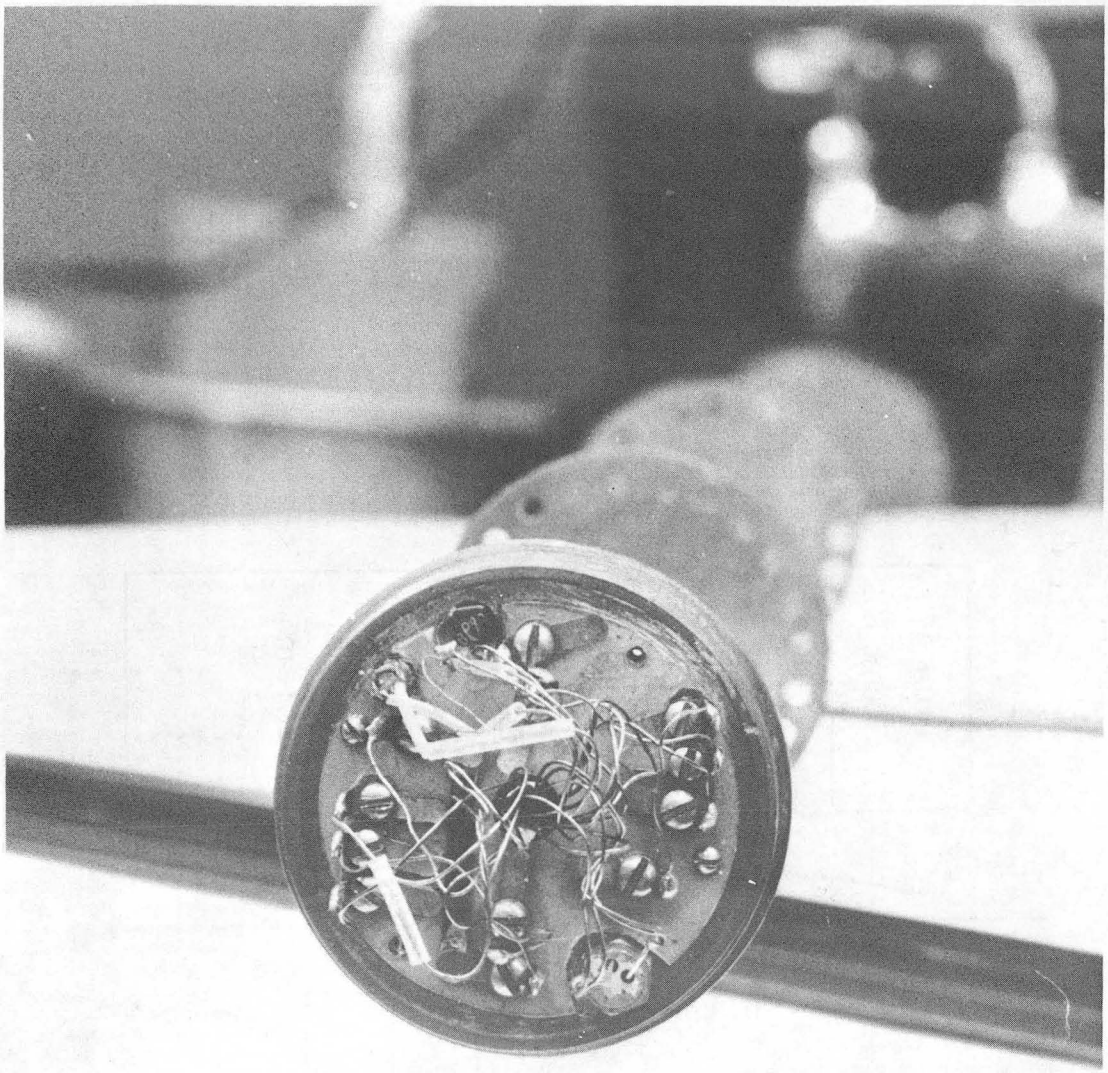

XBB 766-4675

Figure VIII. 3b

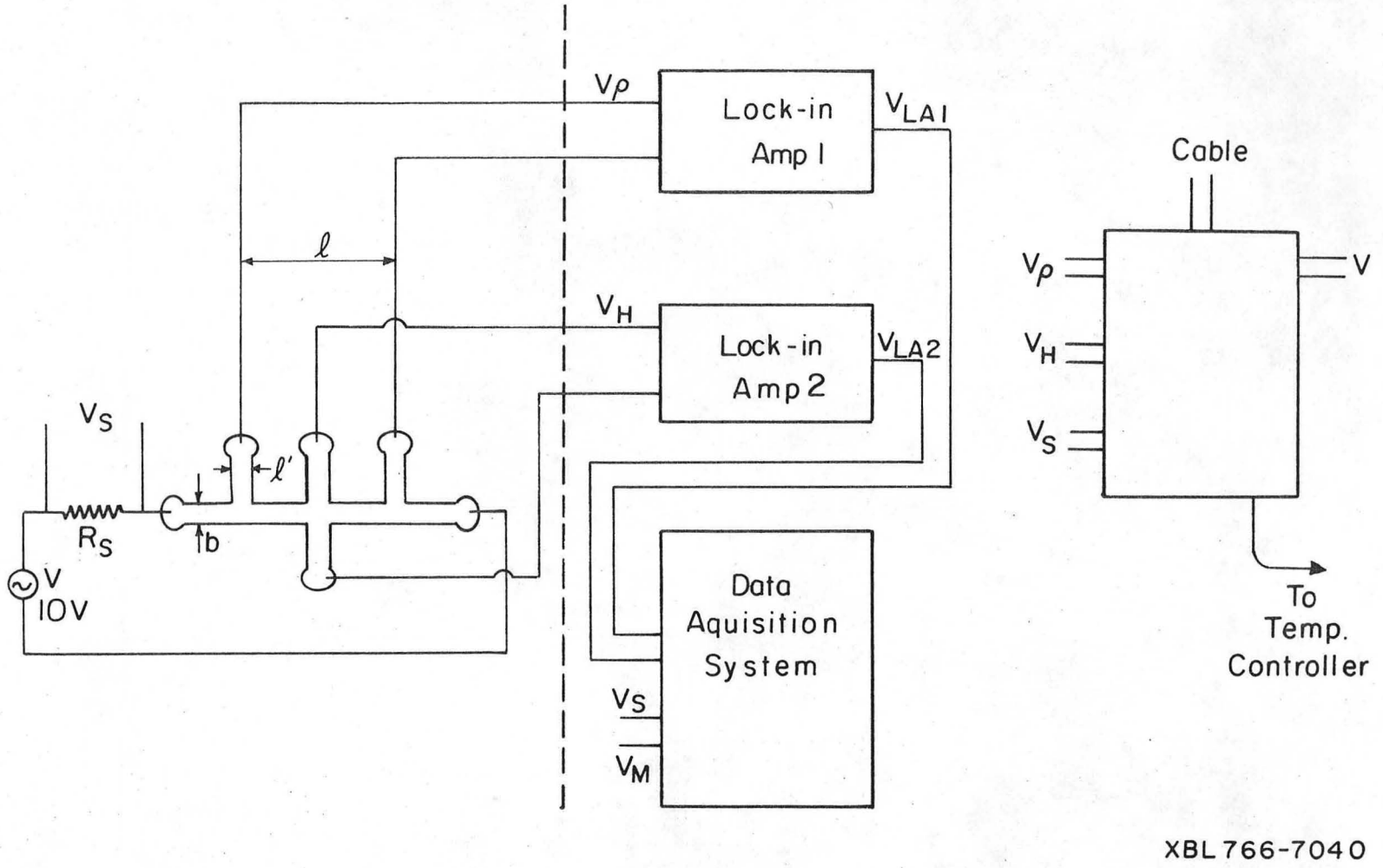
Vρ
Lock-in
Amp 1
VLA1
ℓ
VH
Lock-in
Amp 2
VLA2
VS
ℓ'
RS
b
V
10V
Data
Aquisition
System
VS
VM
Cable
Vρ
VH
VS
V
To
Temp.
Controller
XBL766-7040

Figure IX. 1a

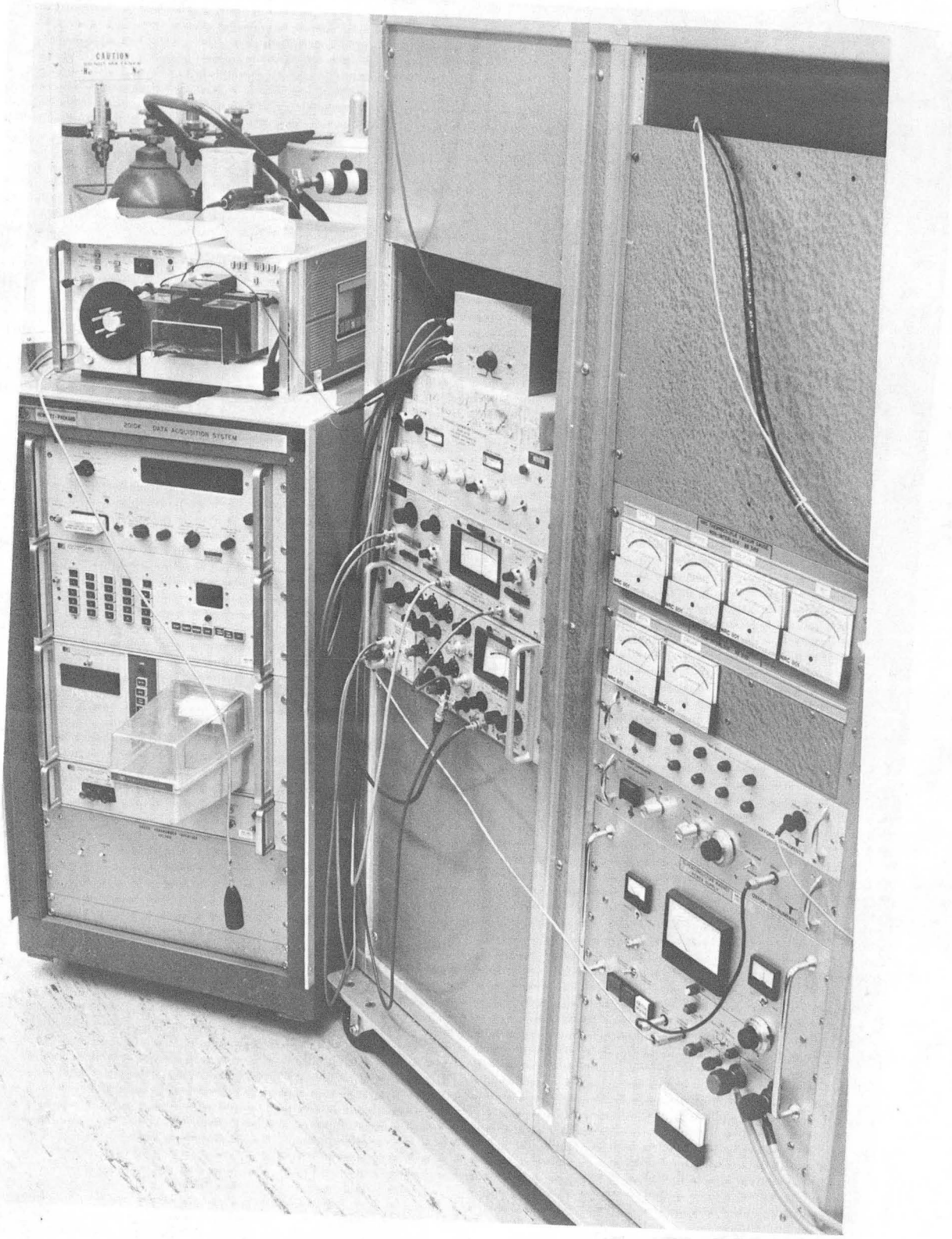

XBB 766-5192

Figure IX. 1b

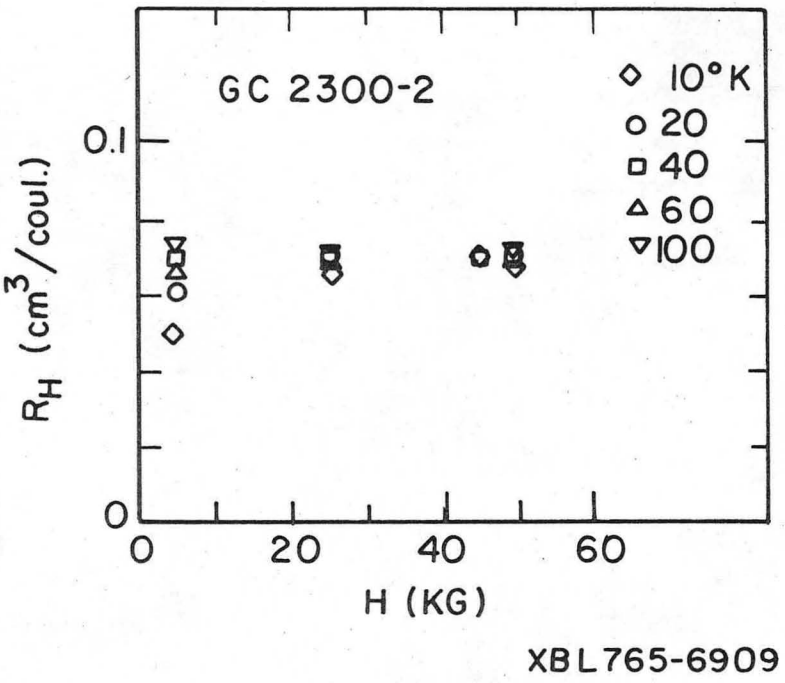
GC 2300-2
10°K
20
40
60
100
0.1
0
R_H (cm^3/coul.)
0
20
40
60
H (KG)
XBL765-6909

Figure X. 1

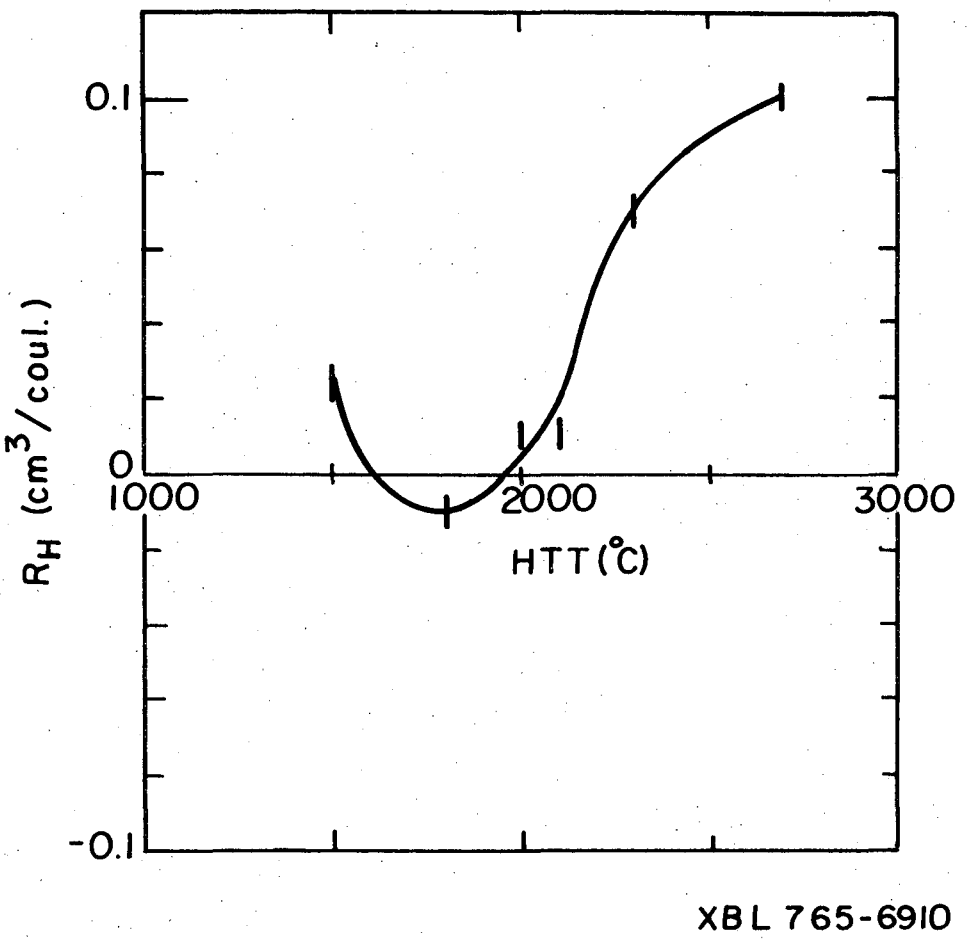

Figure X. 2

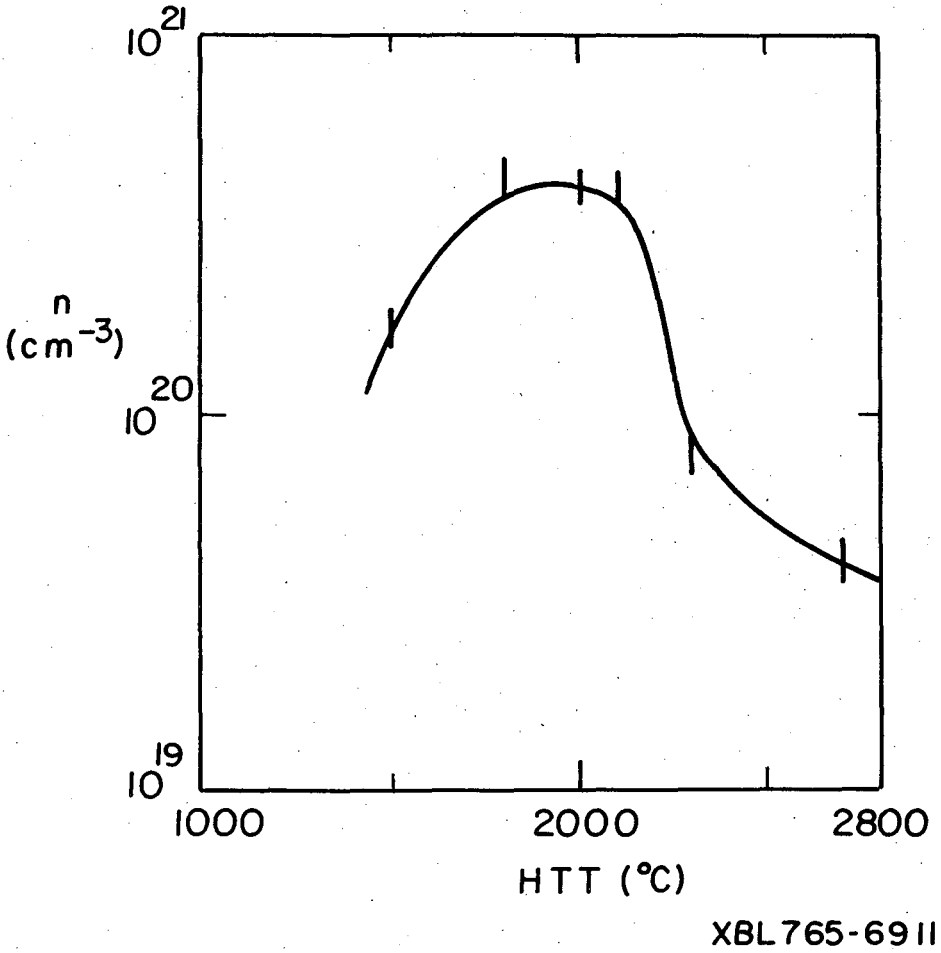

Figure X. 3

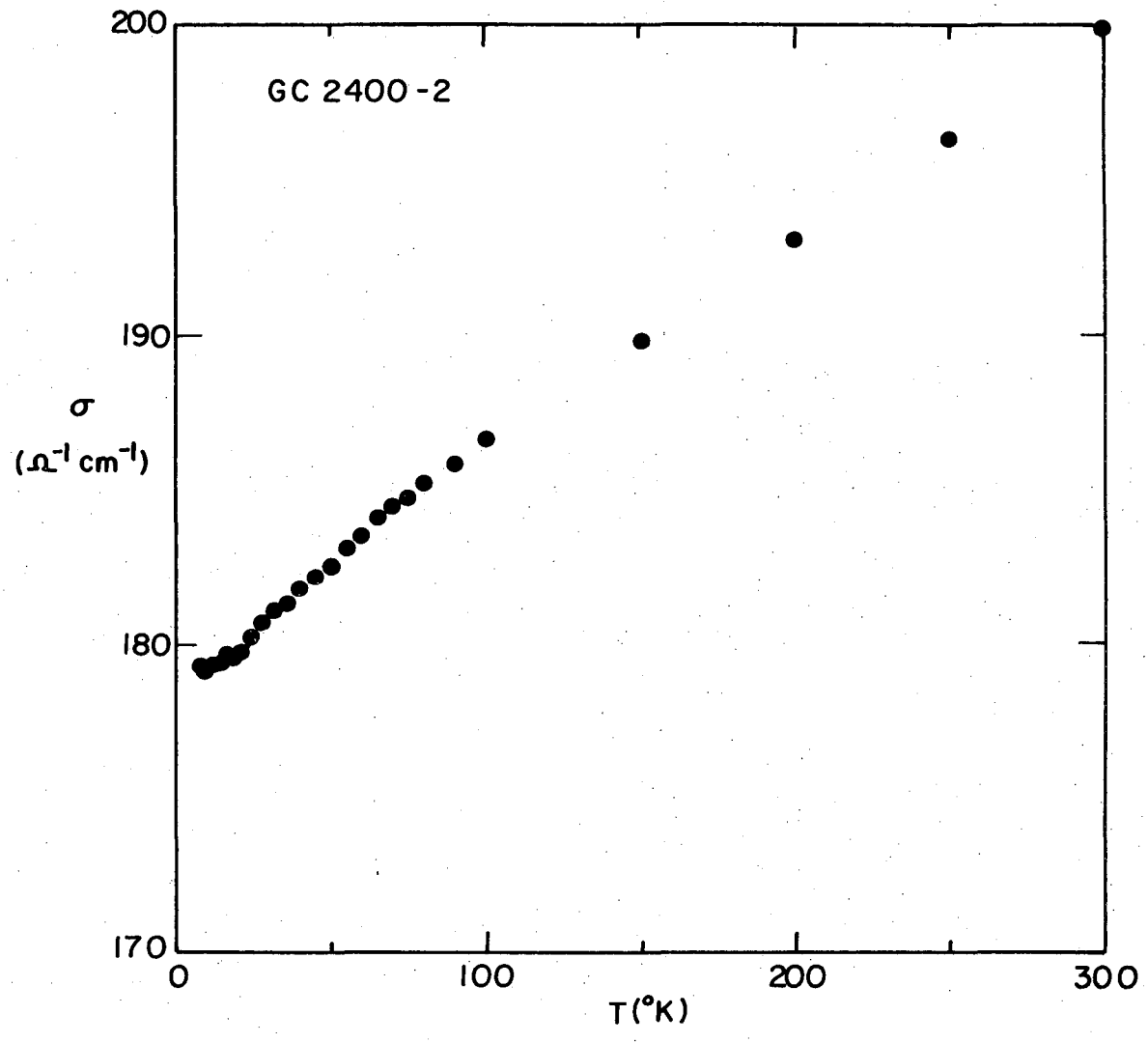

Figure X. 4

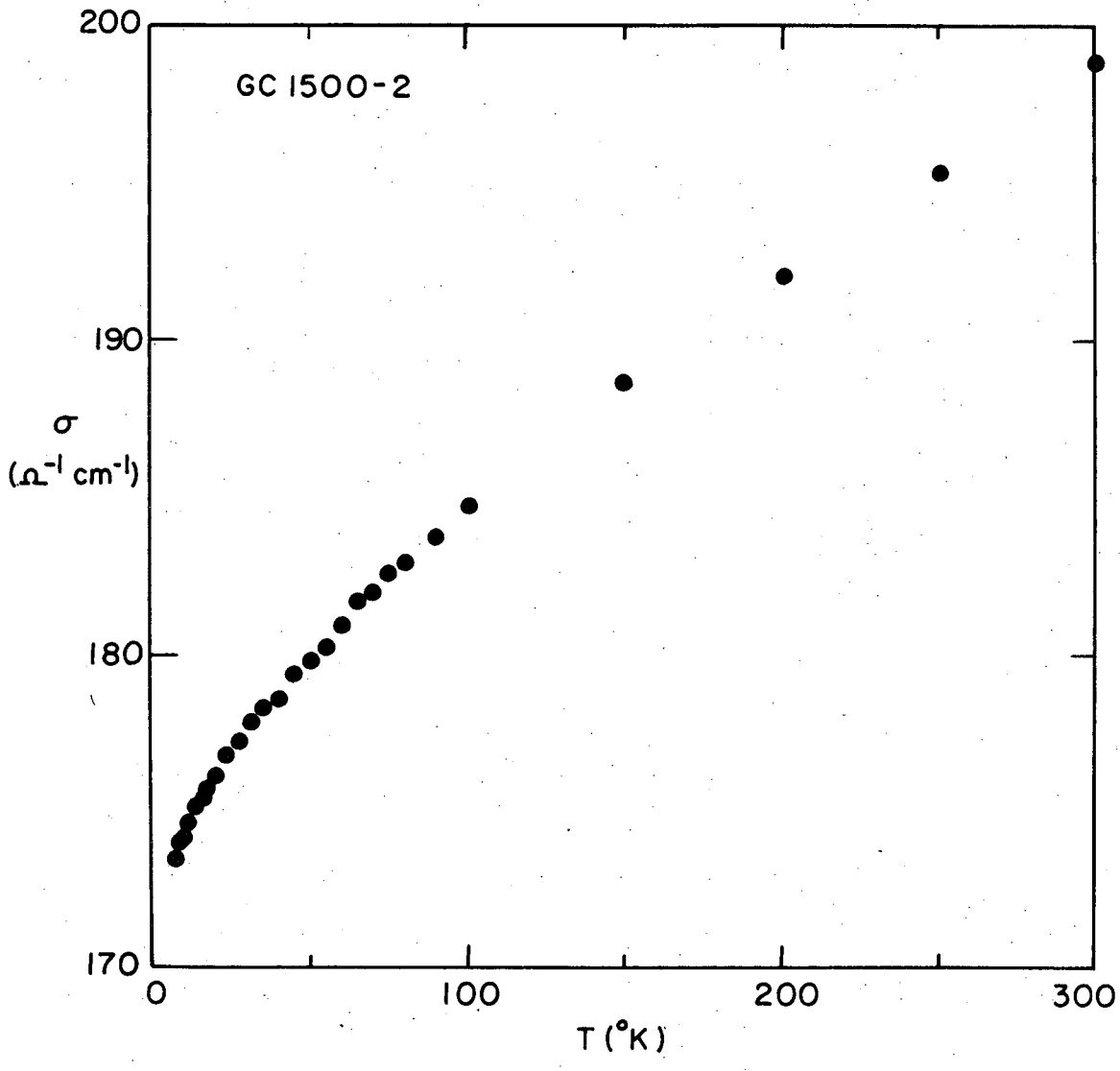

Figure X. 5

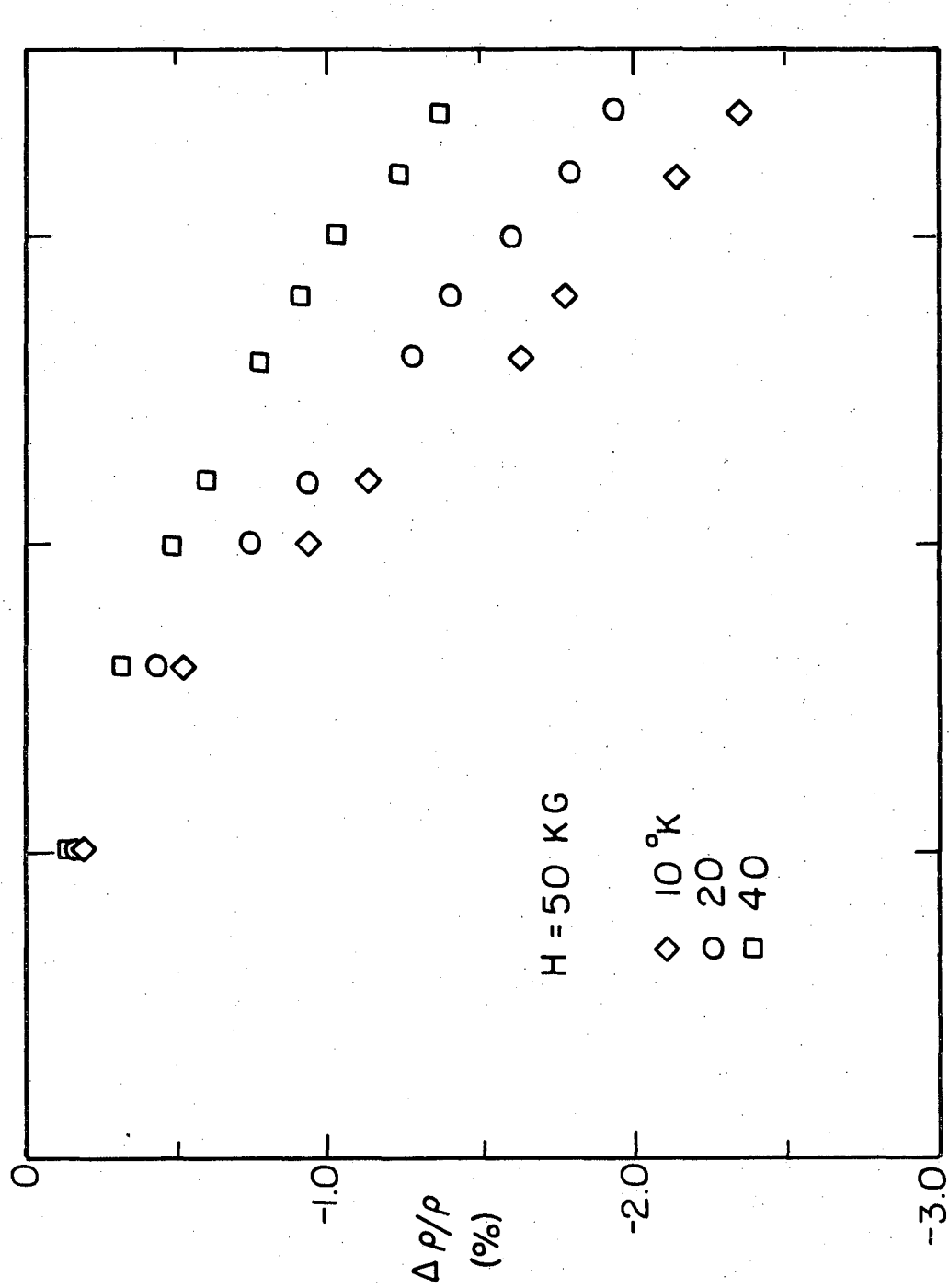

XBL 765-6912

Figure X. 6

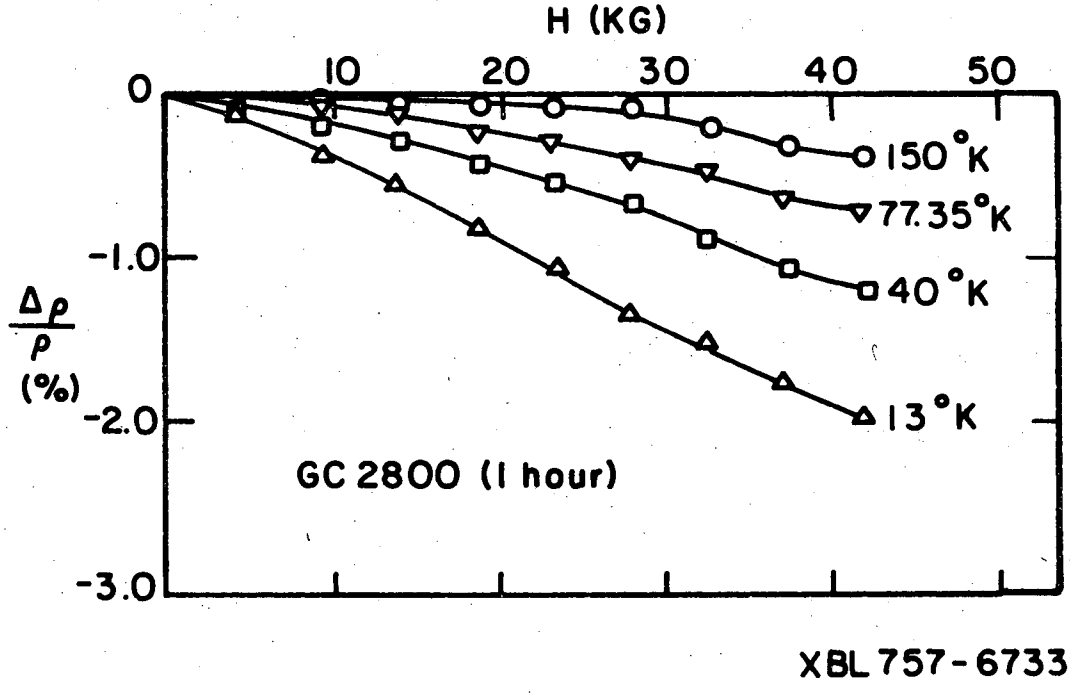
H (KG)
10
20
30
40
50
0
-1.0
-2.0
-3.0
Δρ/ρ (%)
150°K
77.35°K
40°K
13°K
GC 2800 (1 hour)
XBL 757-6733

Figure X. 7

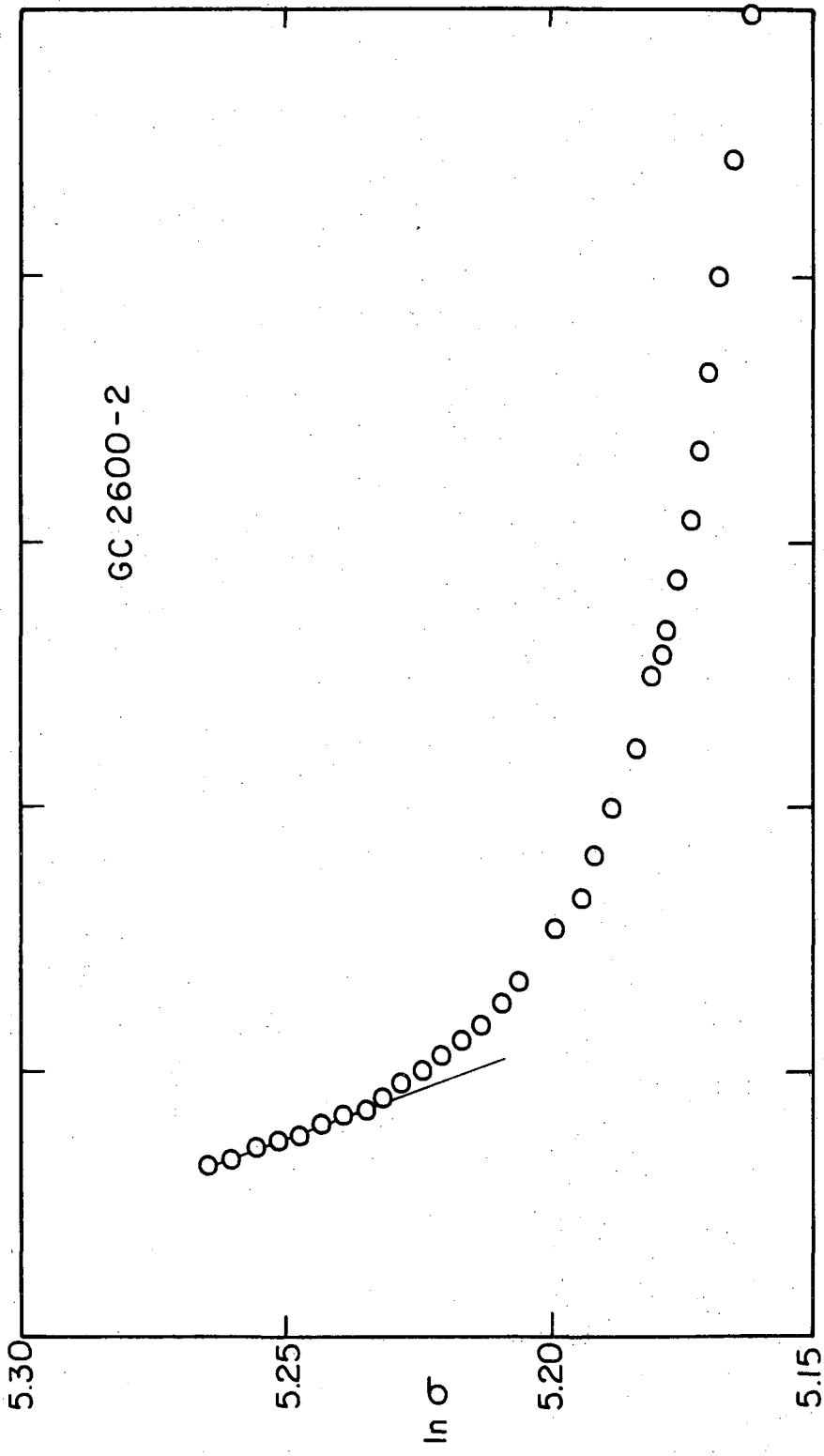

XBL 765-6913

Figure X. 8

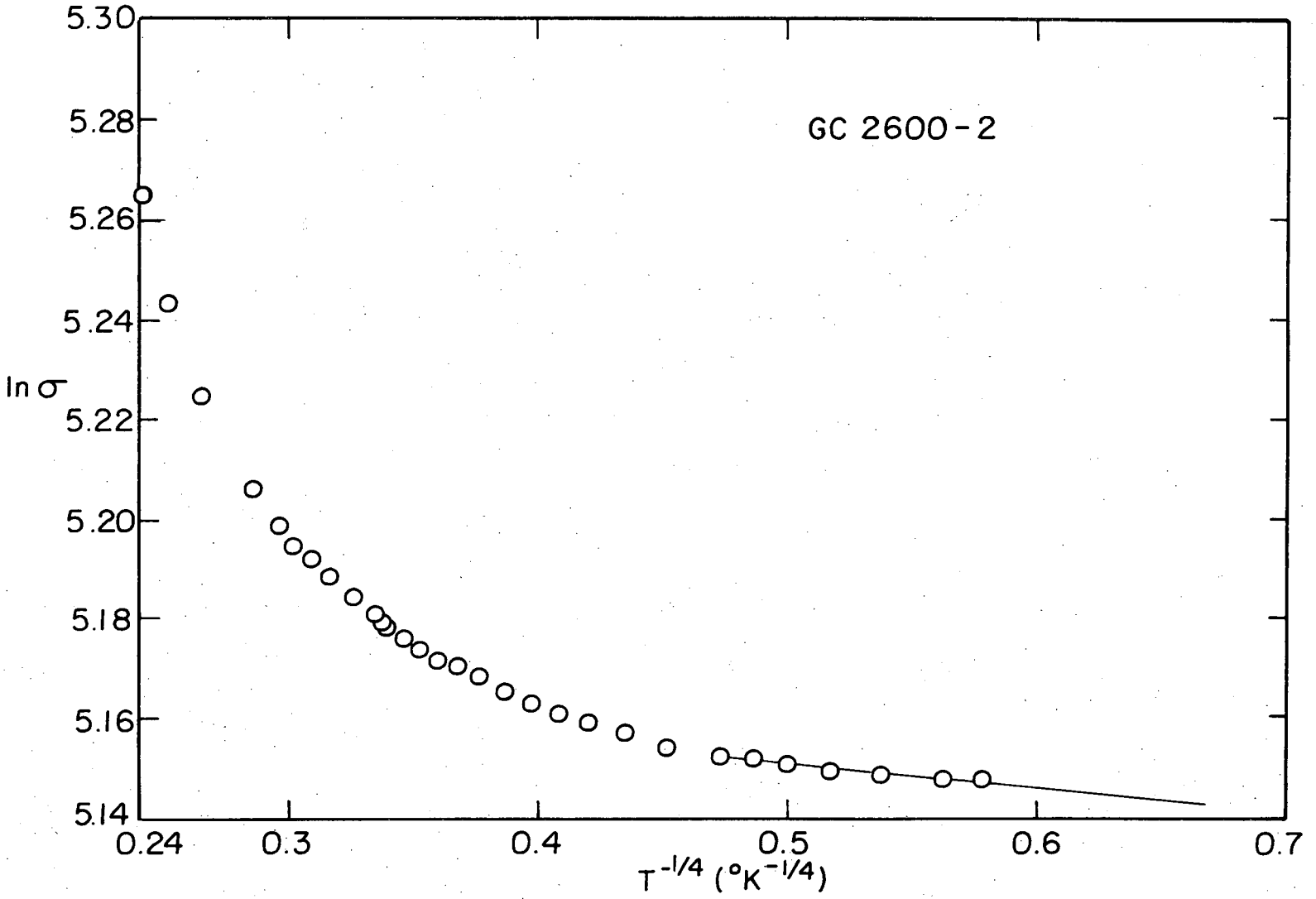

XBL 765-6914

Figure X. 9

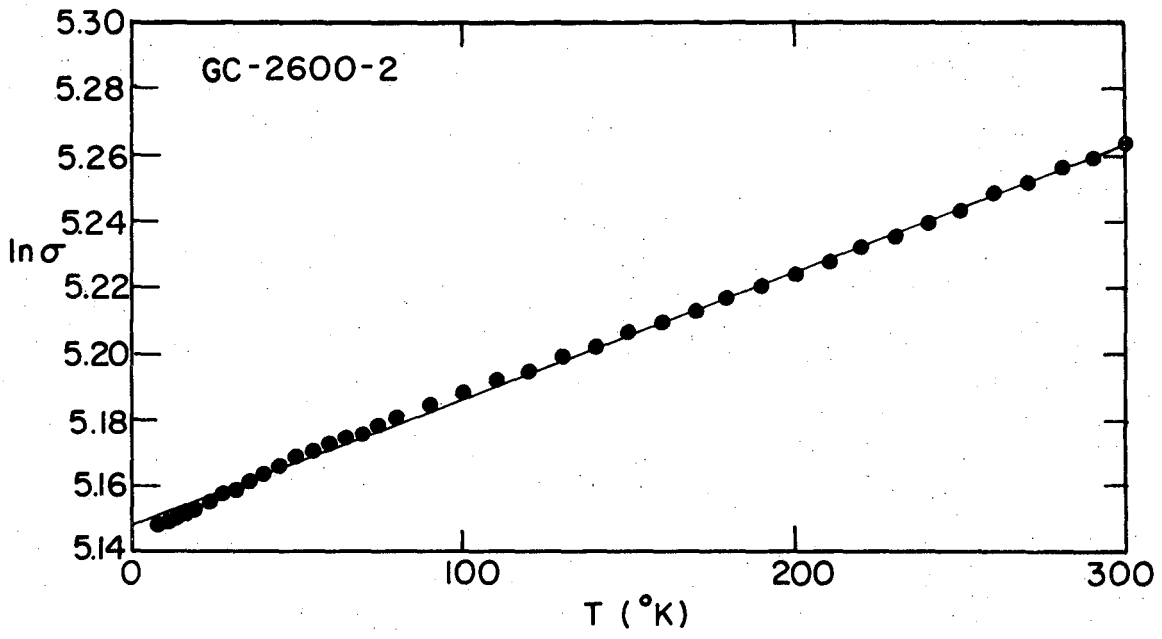

XBL765-6915

Figure X. 10

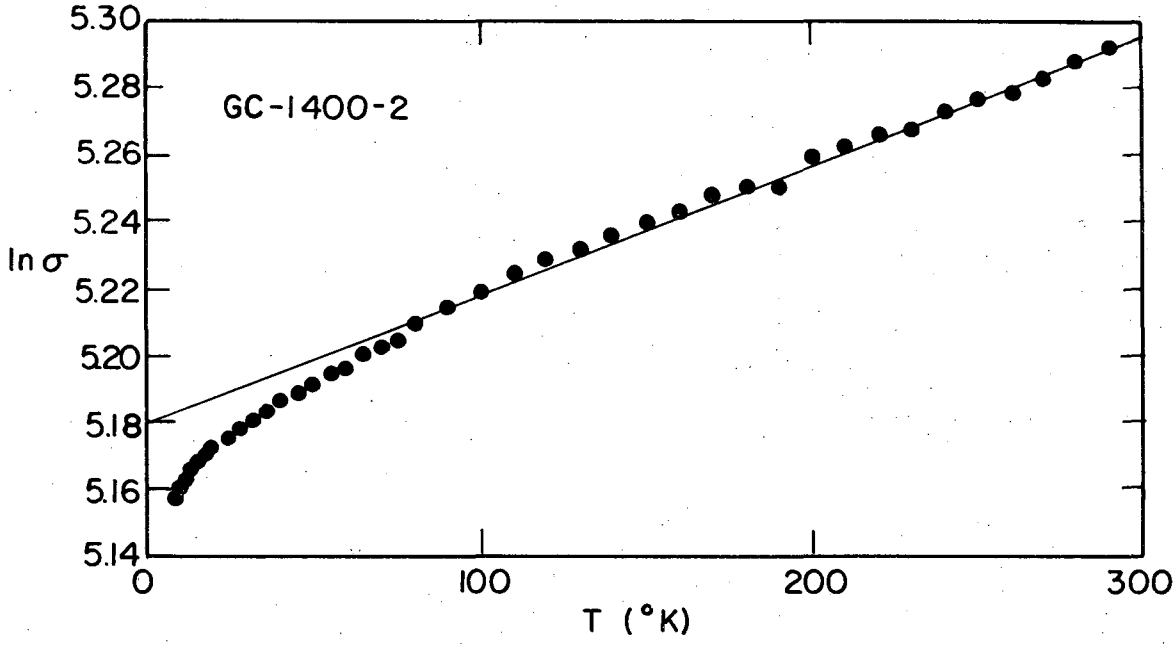
5.30
5.28
5.26
5.24
5.22
5.20
5.18
5.16
5.14
ln σ
GC-1400-2
0
100
200
300
T (°K)
XBL765-6916

Figure X. 11

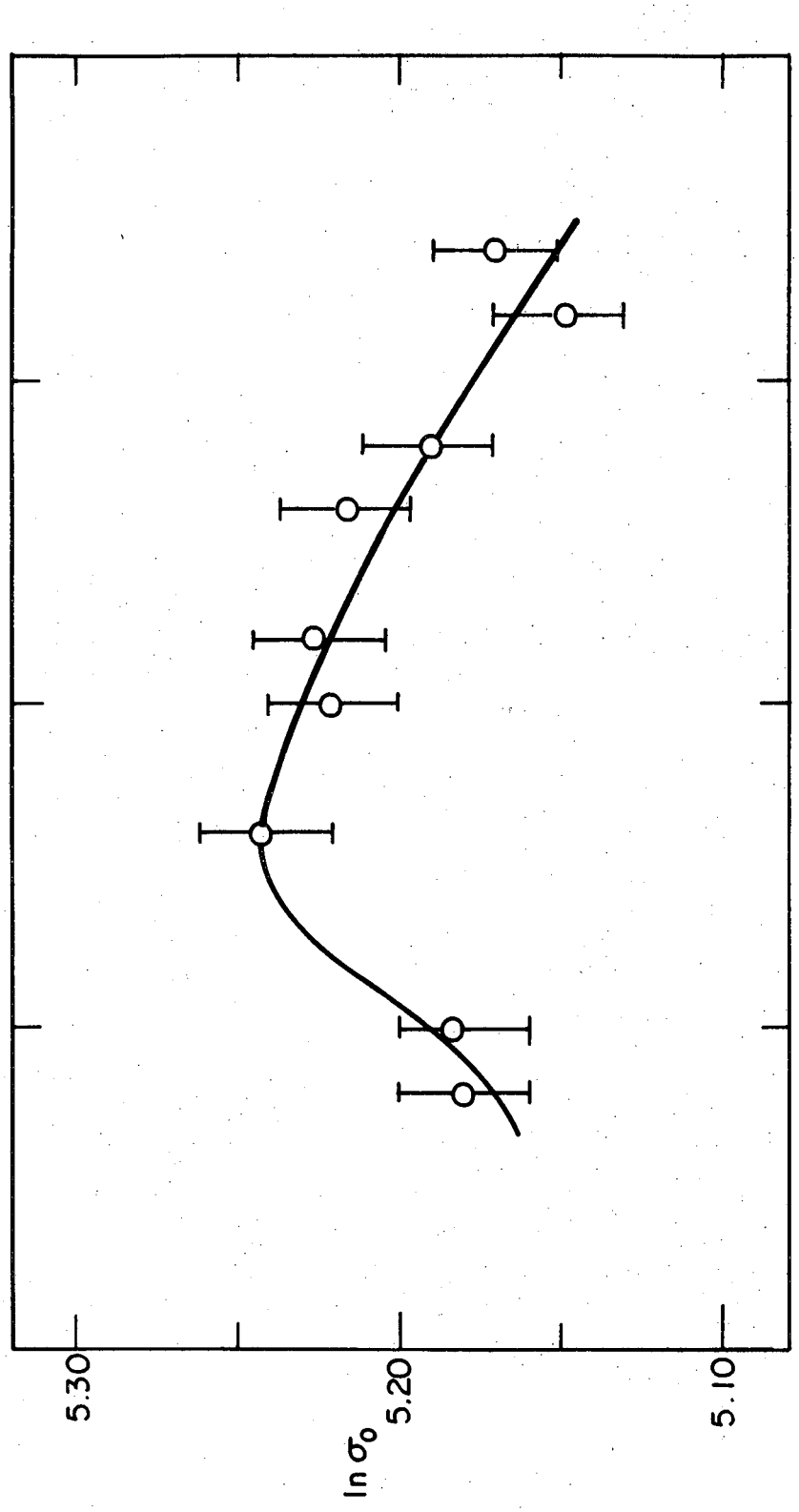

XBL 765-6917

Figure X. 12

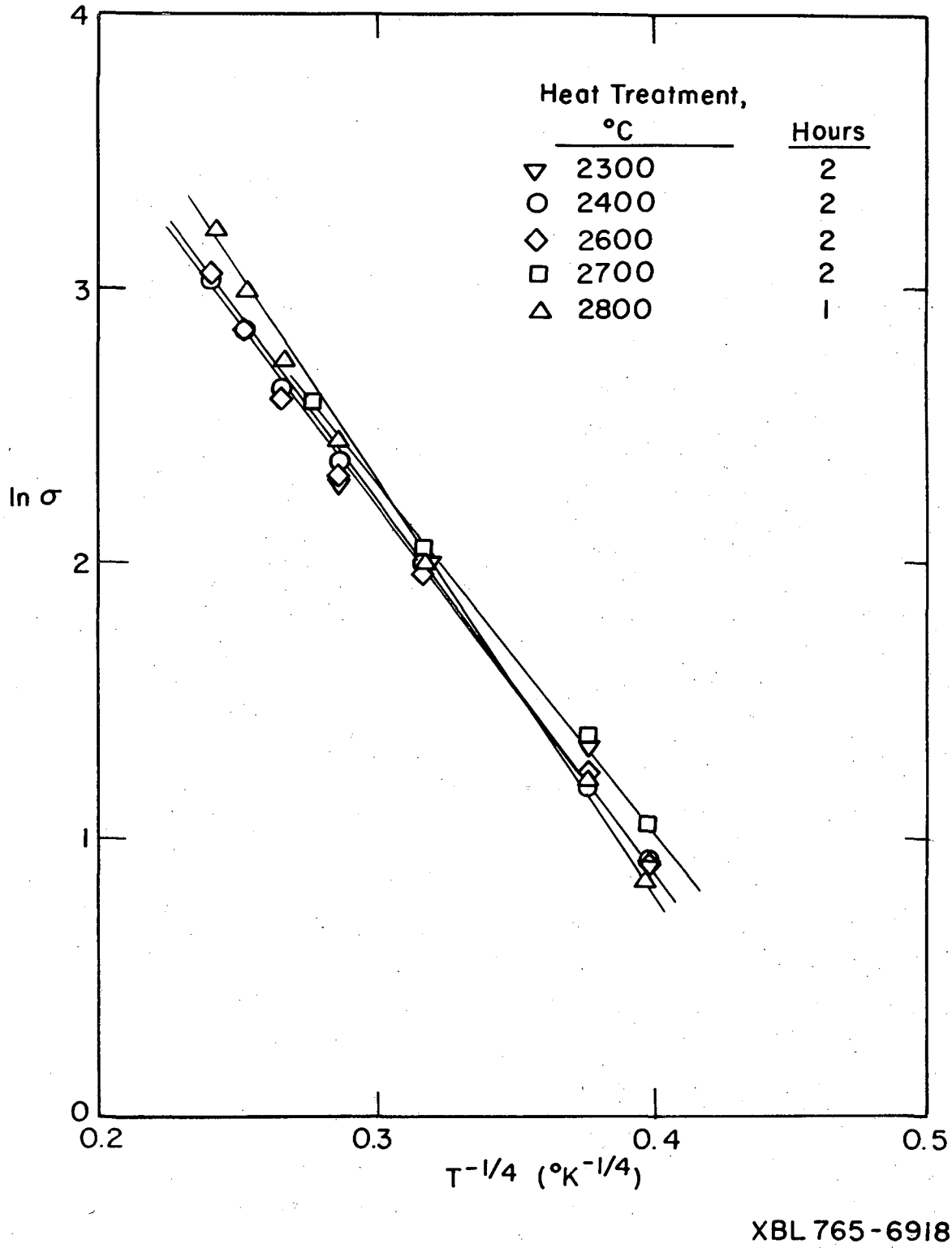
Heat Treatment,
°C
Hours
2300
2
2400
2
2600
2
2700
2
2800
1
ln σ
4
3
2
1
0
0.2
0.3
0.4
0.5
T^-1/4 (°K^-1/4)
XBL 765-6918

Figure X. 13

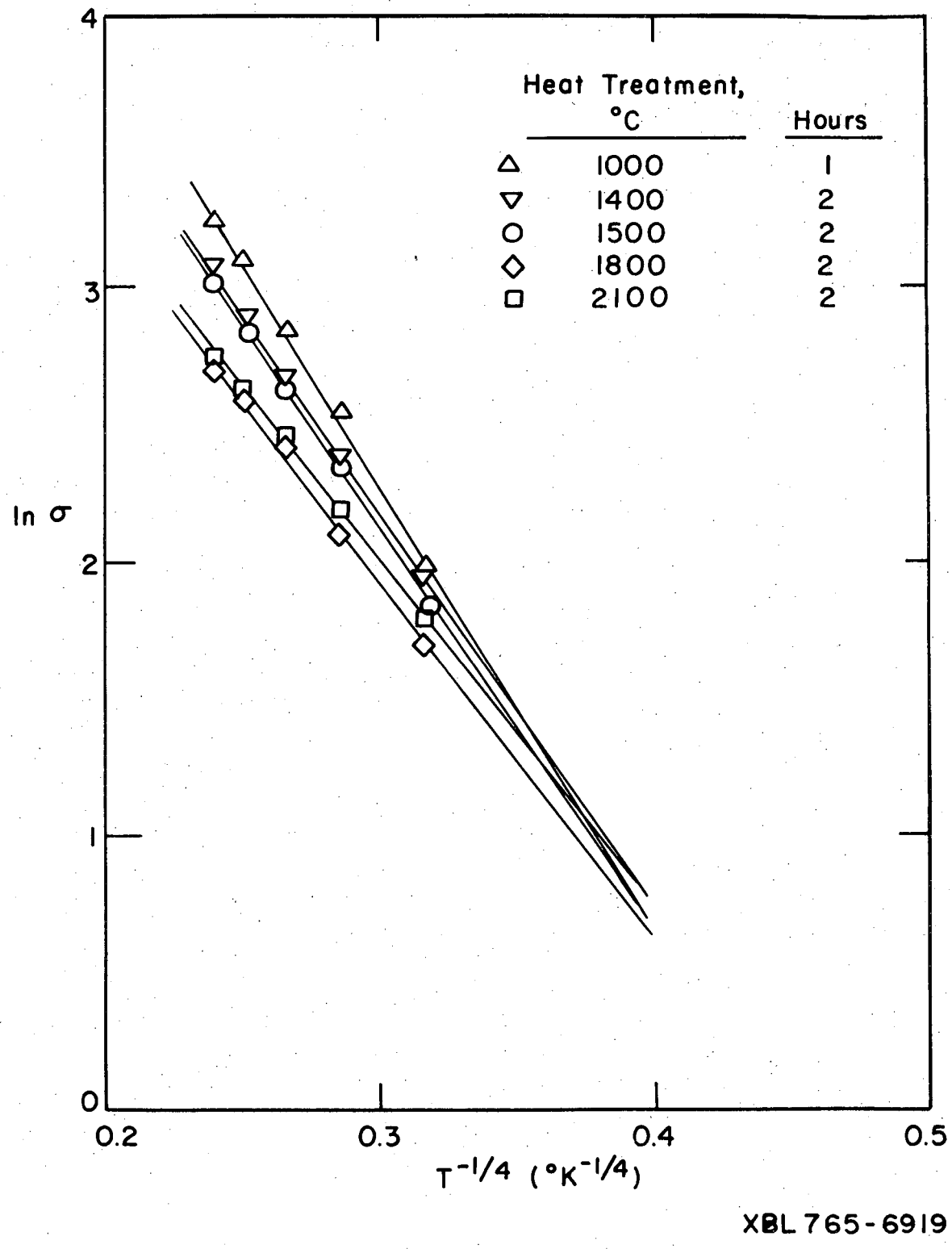

Figure X. 14

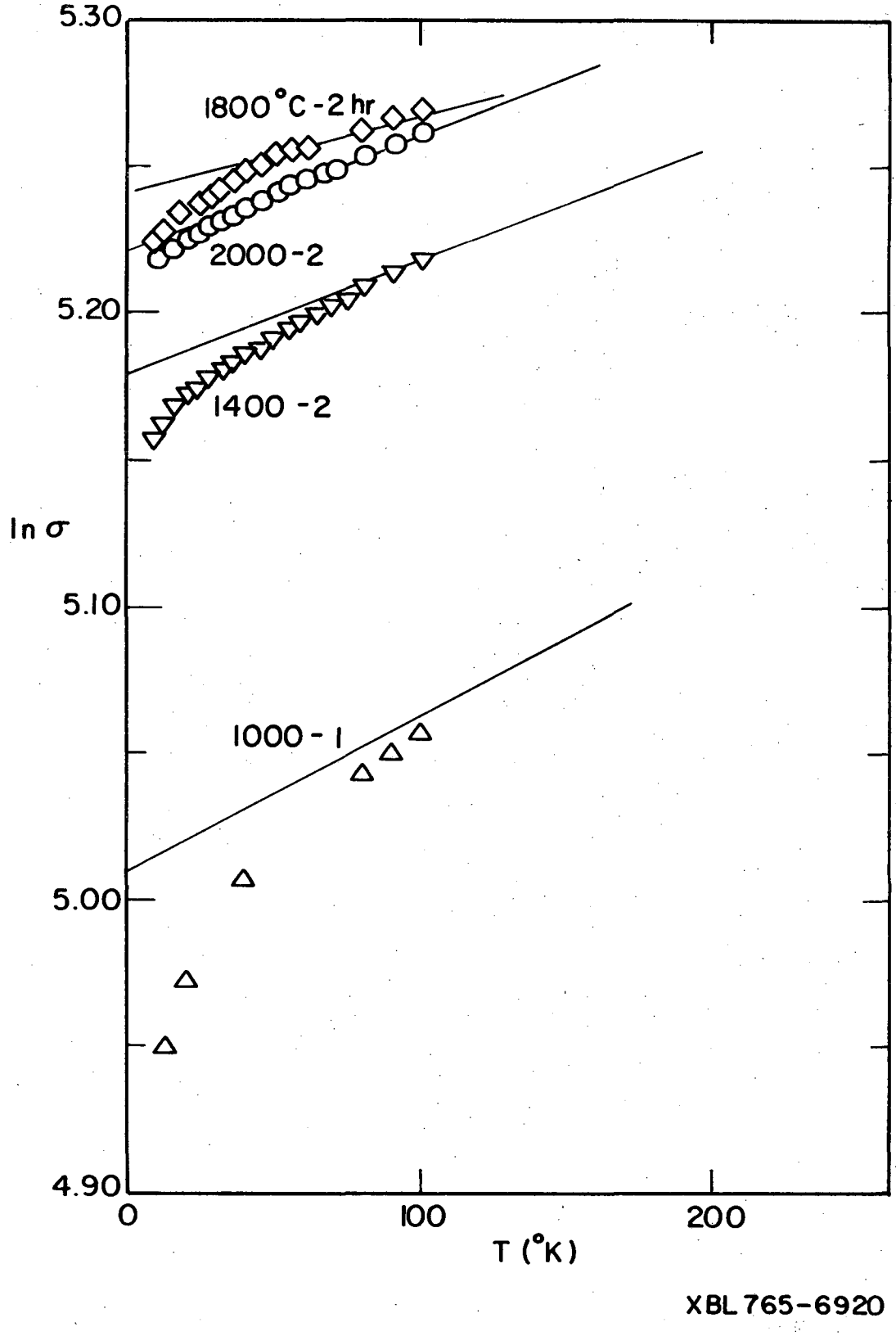
5.30
5.20
5.10
5.00
4.90
ln σ
1800°C - 2 hr
2000 - 2
1400 - 2
1000 - 1
0
100
200
T (°K)
XBL 765-6920

Figure X. 15

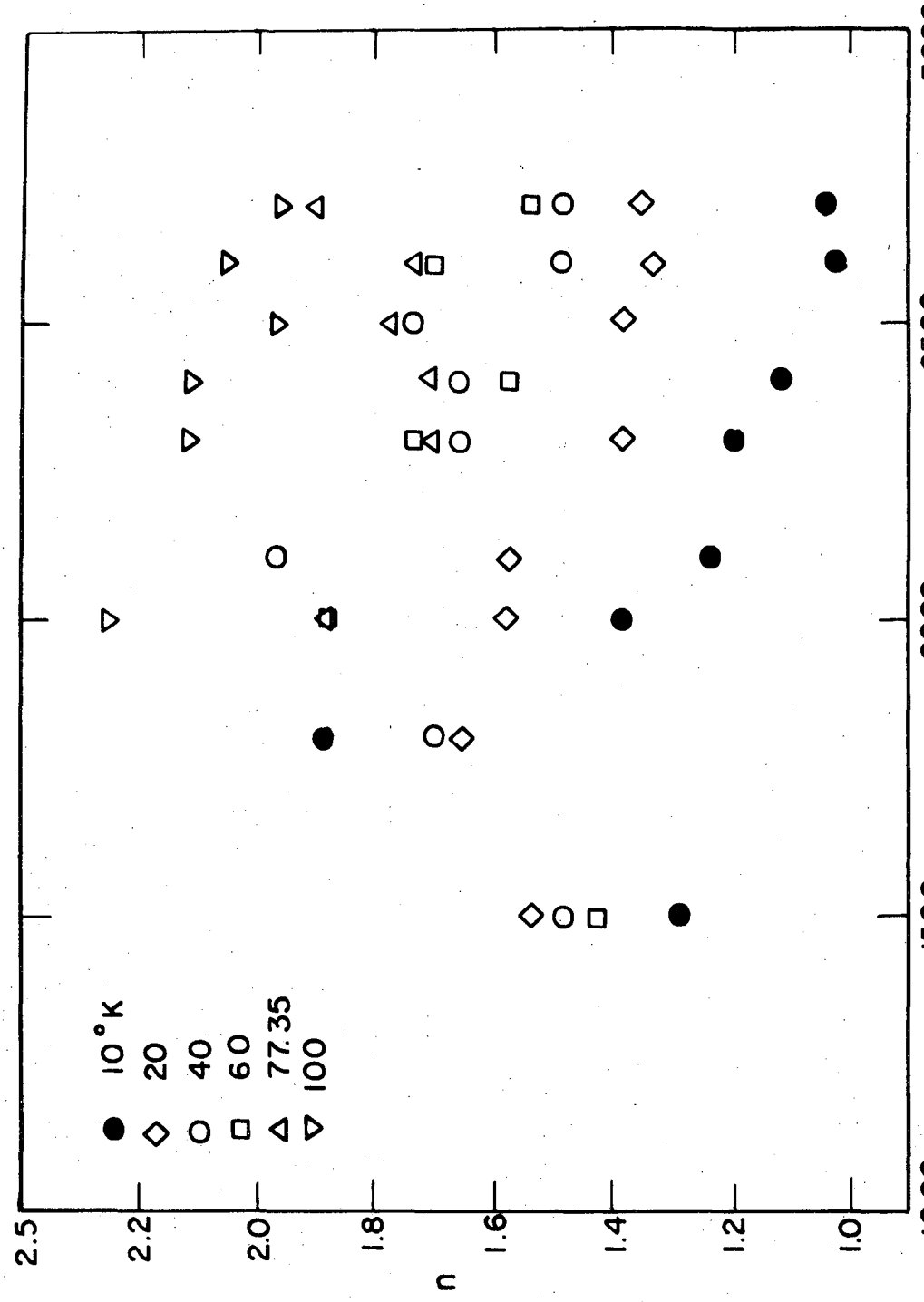

XBL 765-6921

Figure X. 16

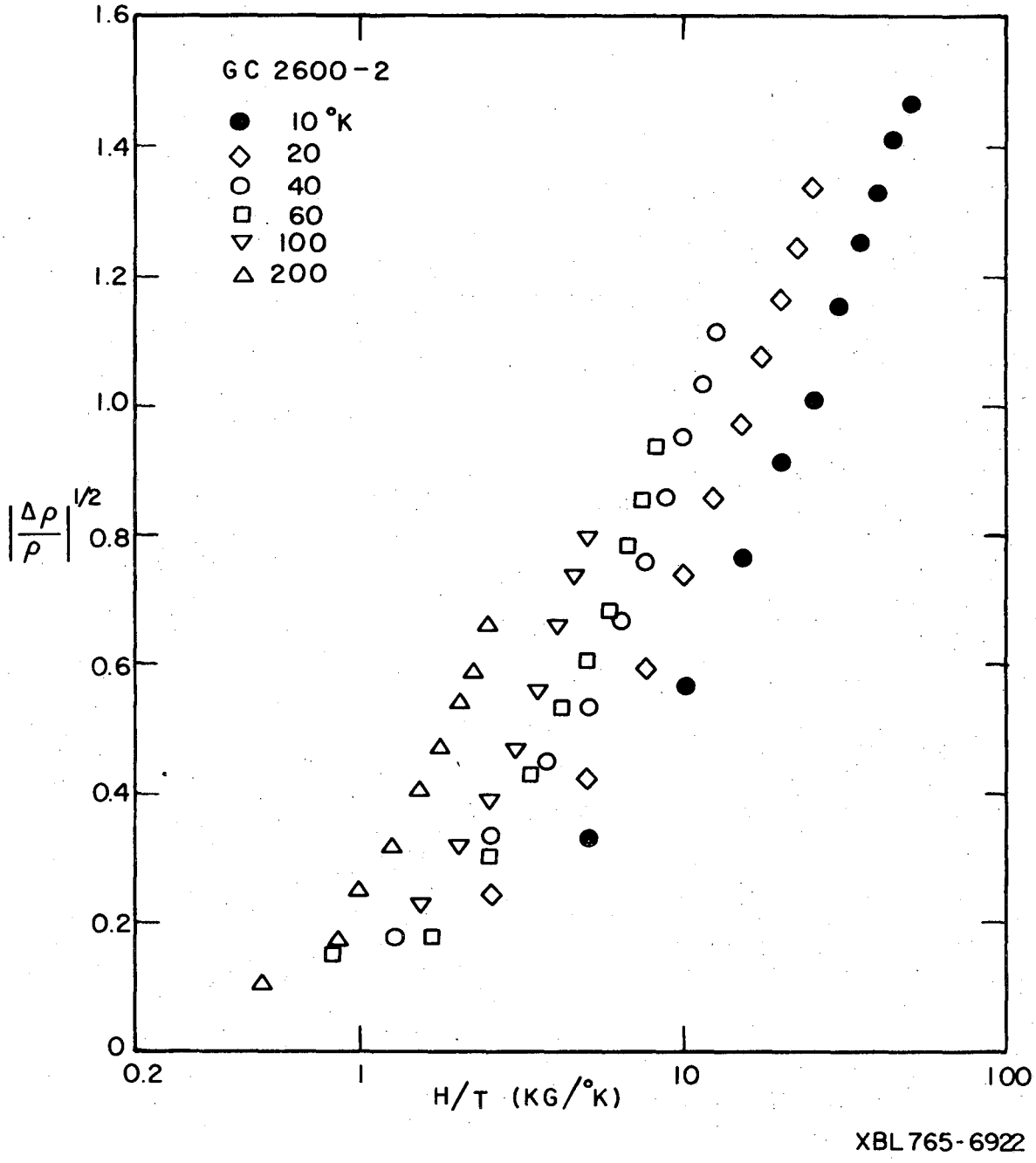
GC 2600-2
10 °K
20
40
60
100
200
$\left|\frac{\Delta\rho}{\rho}\right|^{1/2}$
1.6
1.4
1.2
1.0
0.8
0.6
0.4
0.2
0
0.2
1
10
100
H/T (KG/°K)
XBL765-6922

Figure X. 17

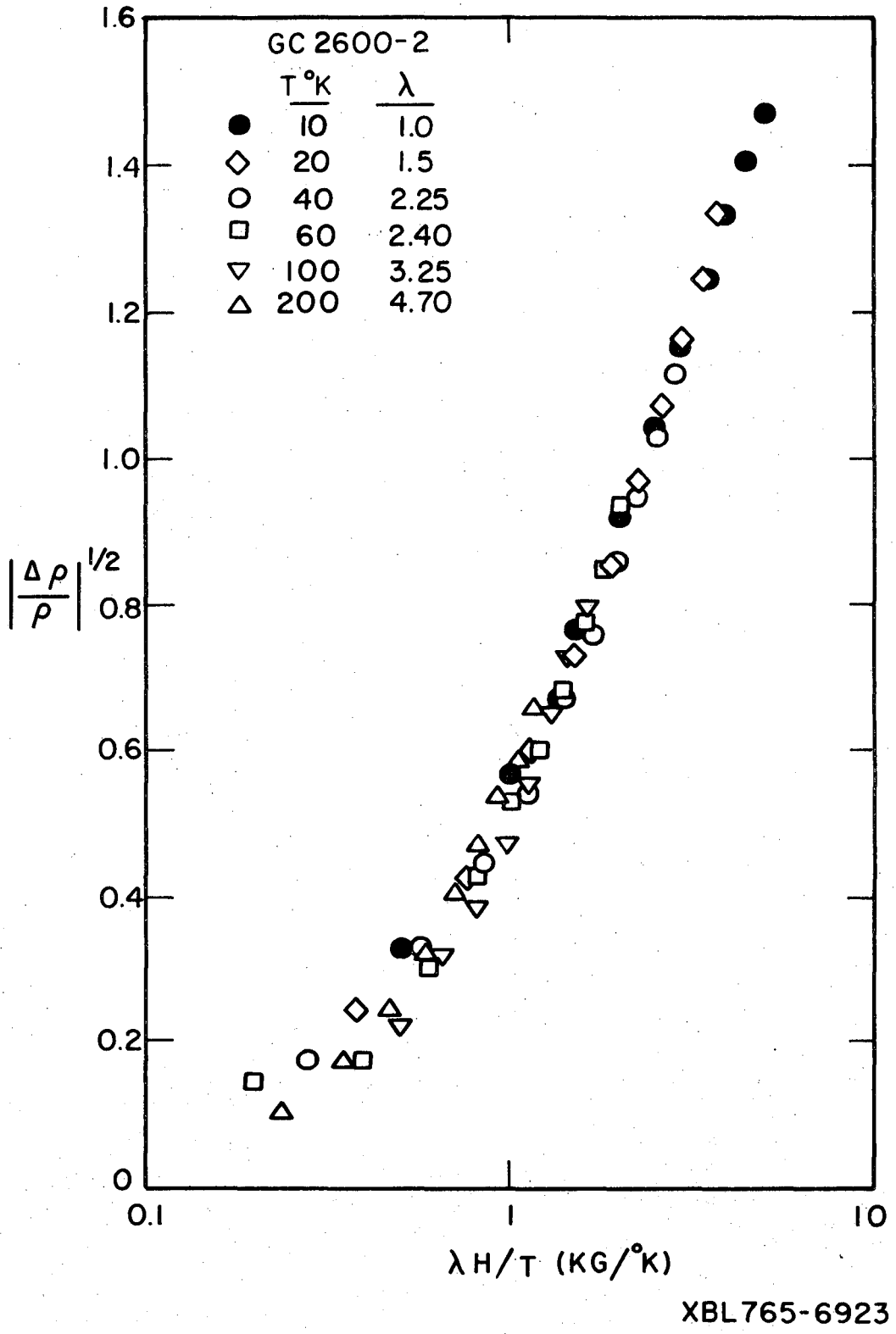

Figure X. 18

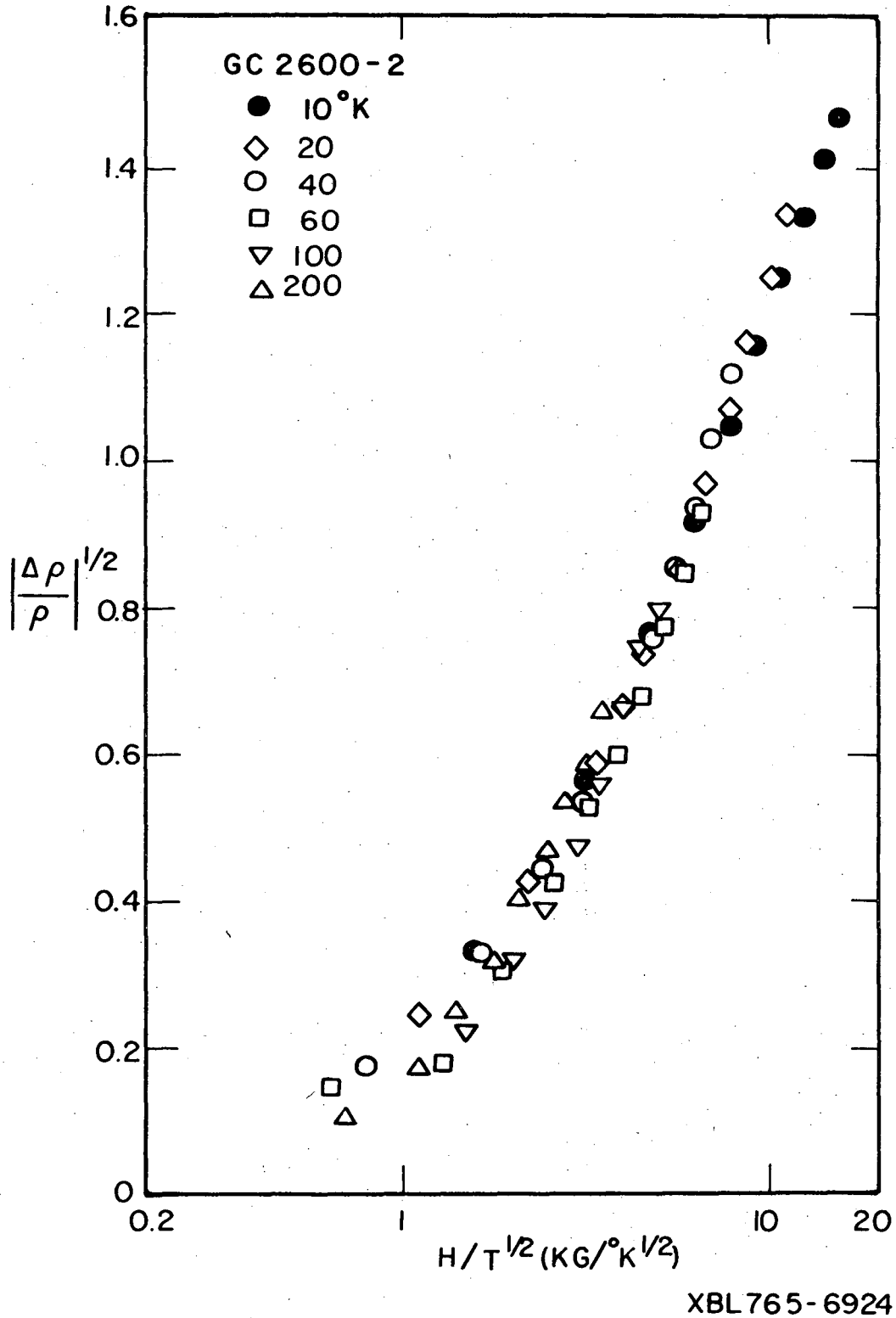
GC 2600-2
10°K
20
40
60
100
200
1.6
1.4
1.2
1.0
0.8
0.6
0.4
0.2
0
$\left|\frac{\Delta\rho}{\rho}\right|^{1/2}$
0.2
1
10
20
$H/T^{1/2}$ (KG/°$K^{1/2}$)
XBL765-6924

Figure X. 19

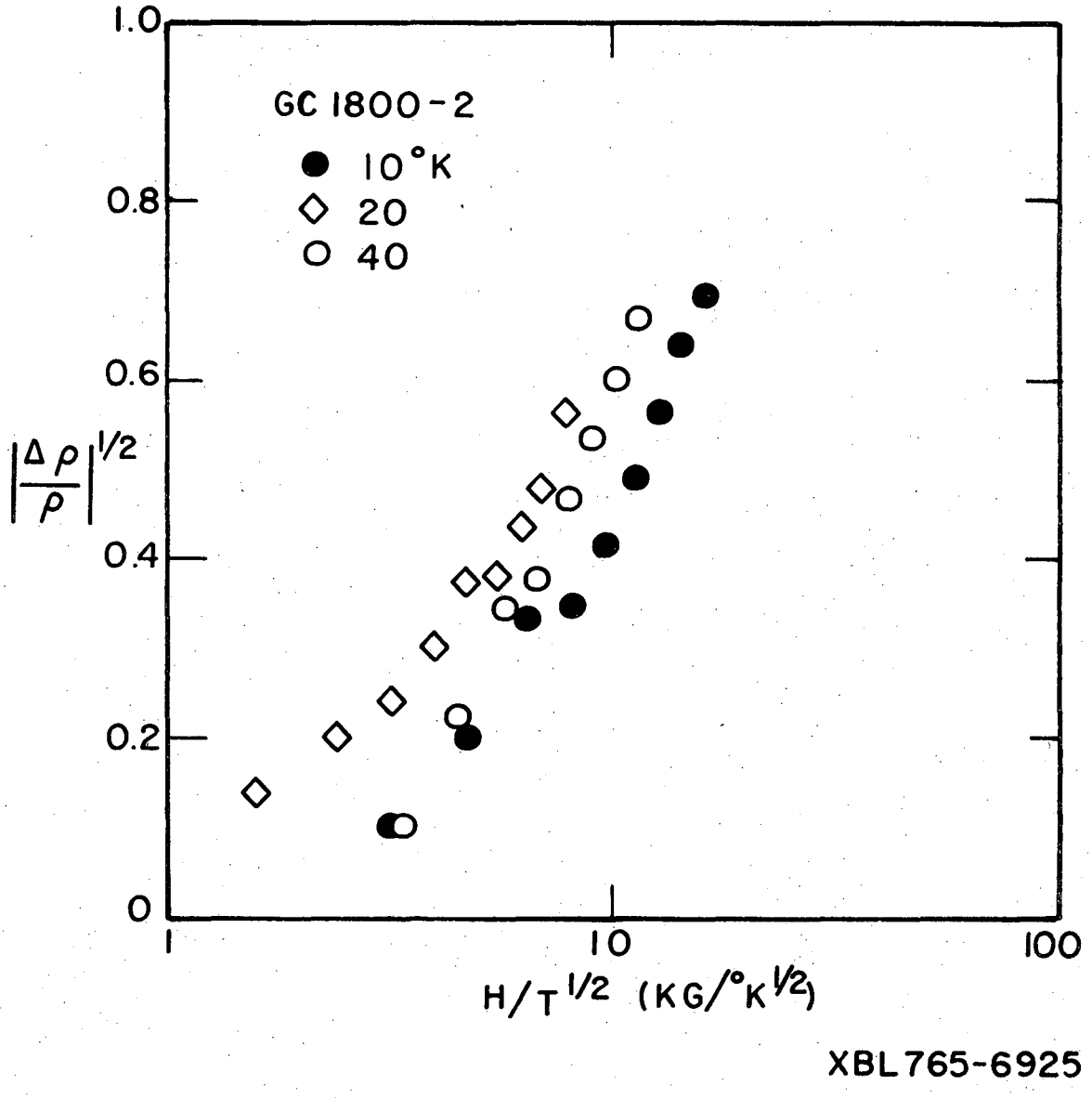

Figure X. 20

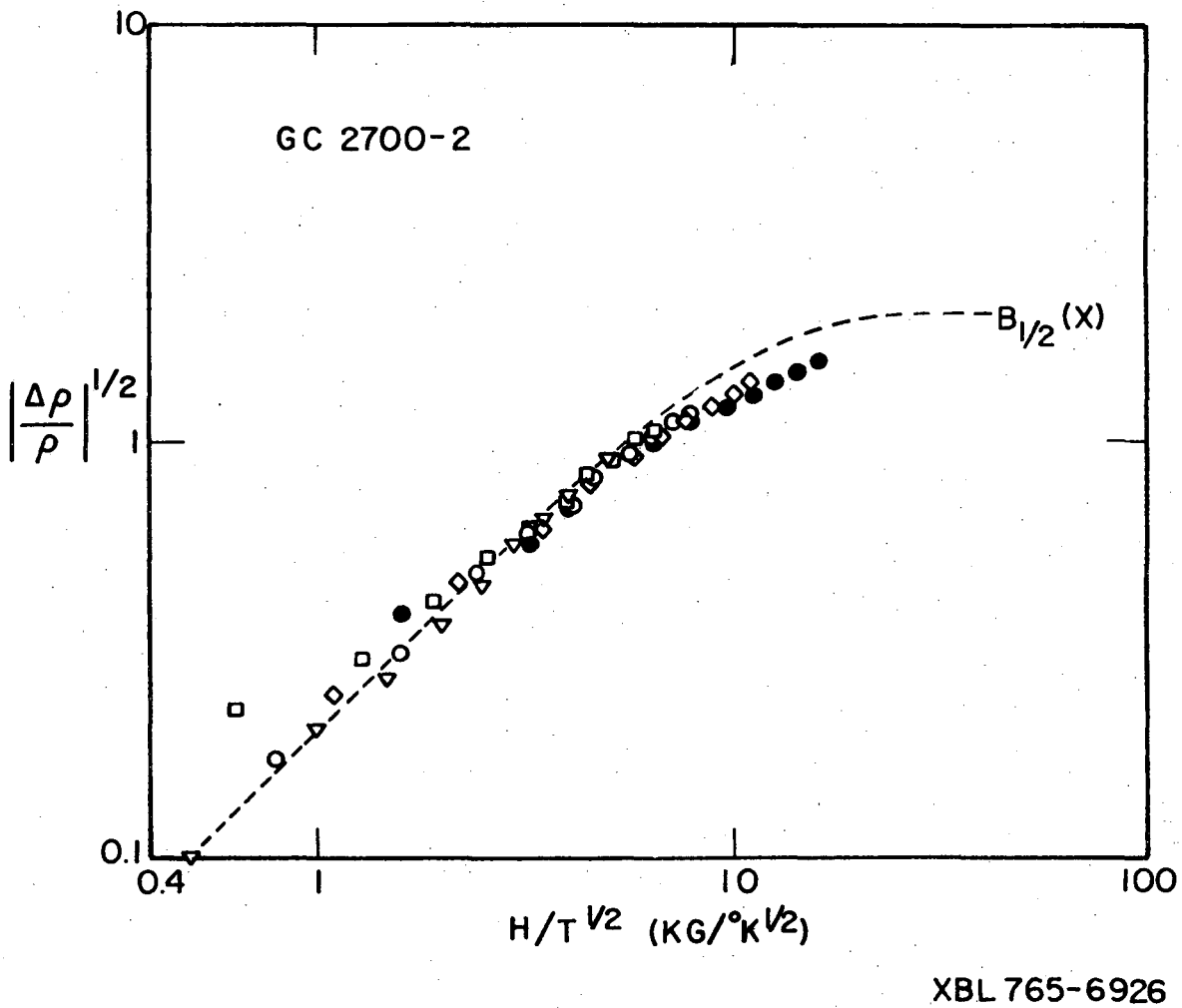
10
GC 2700-2
$B_{1/2}(X)$
$\left|\frac{\Delta\rho}{\rho}\right|^{1/2}$
1
0.1
0.4
1
10
100
$H/T^{1/2}$ (KG/°K$^{1/2}$)
XBL 765-6926

Figure X. 21

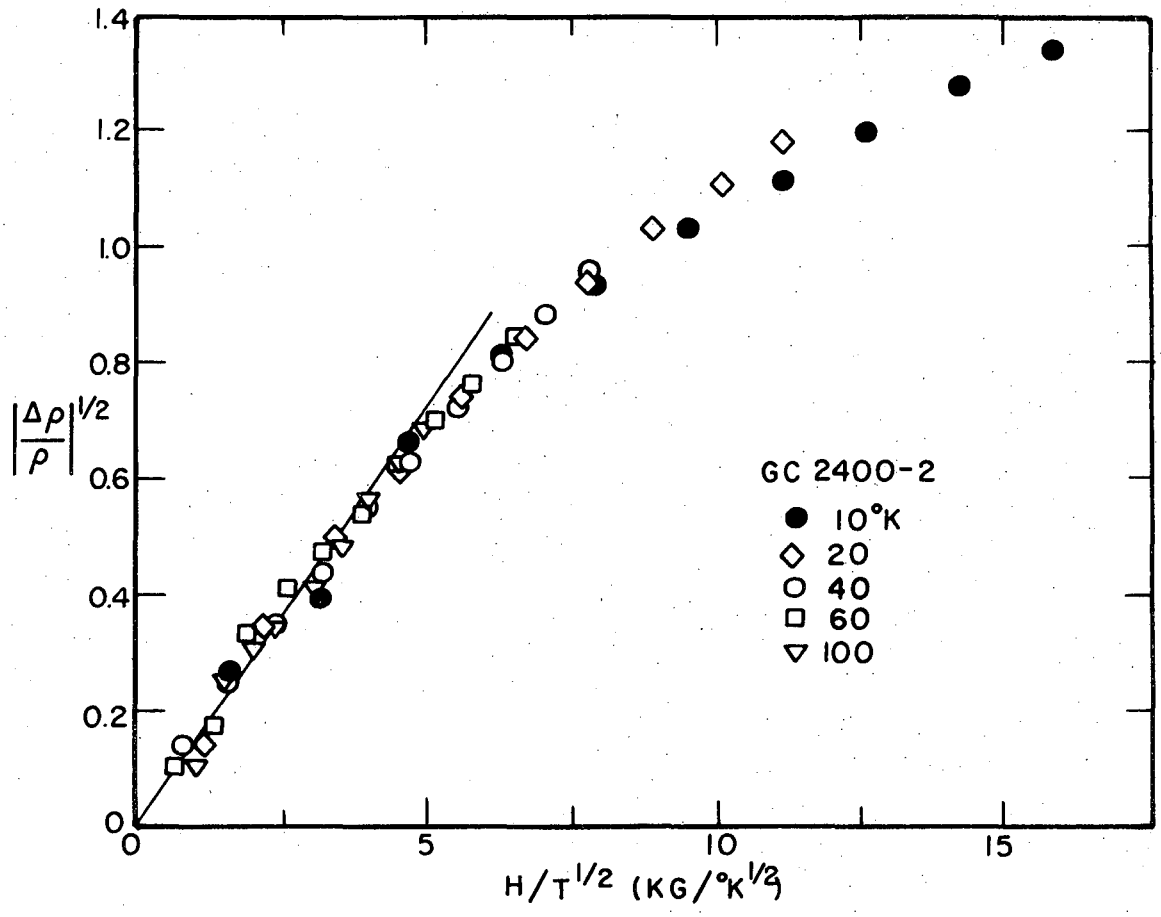

Figure X. 22

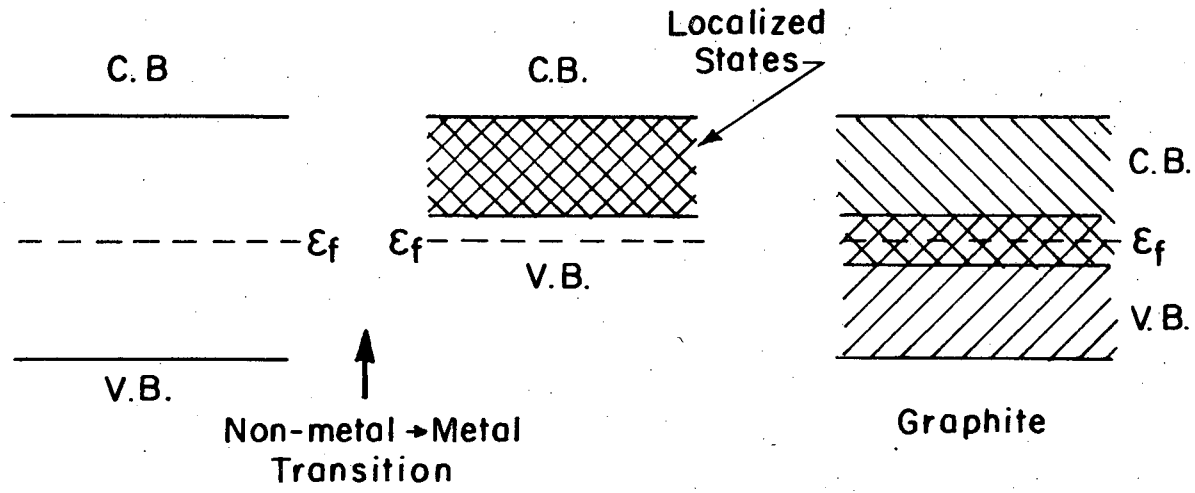

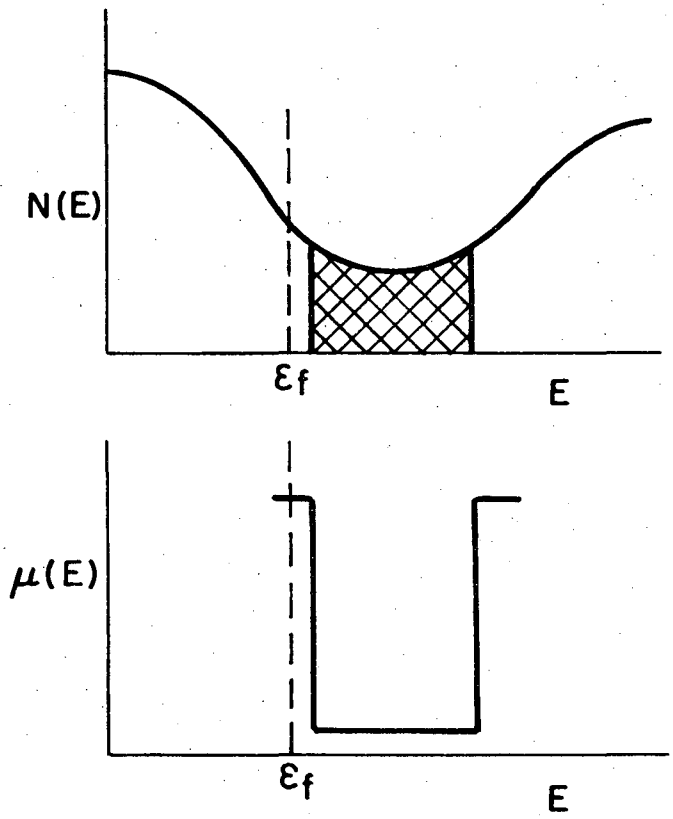

XBL765-6928

Figure X. 23

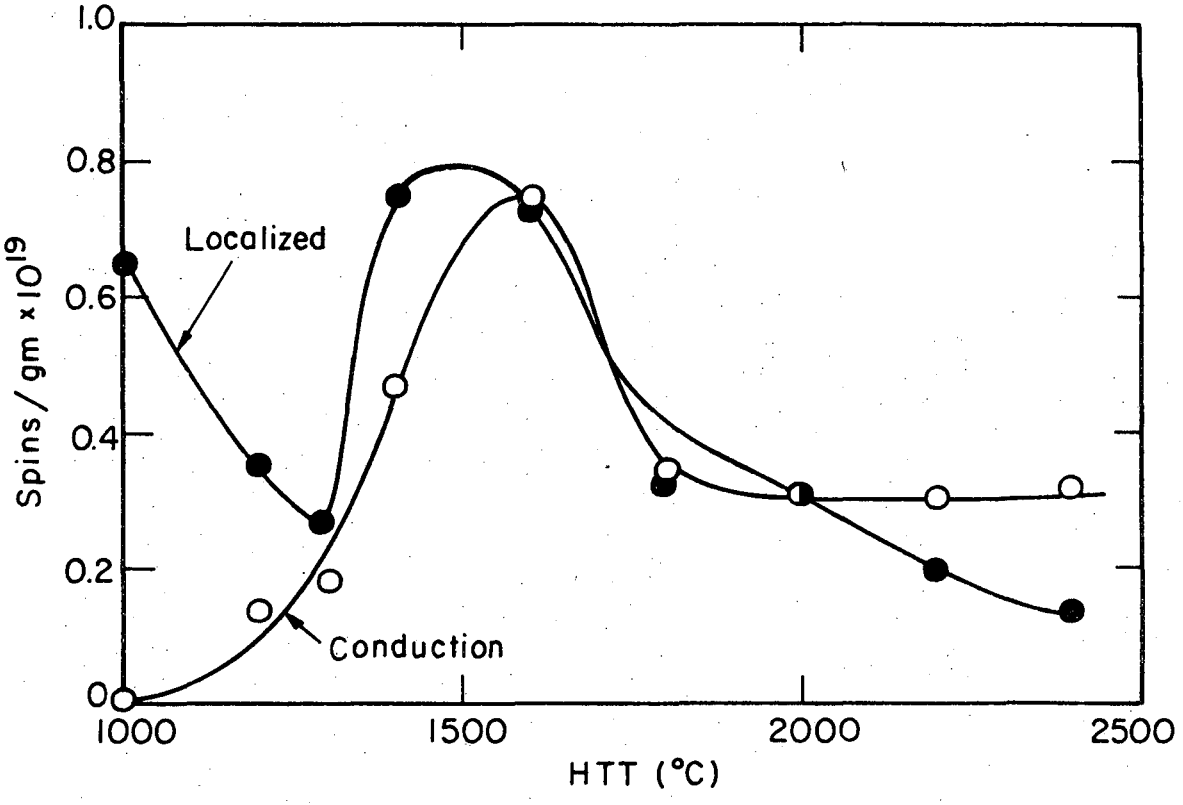

XBL 765-6929

Figure X. 24

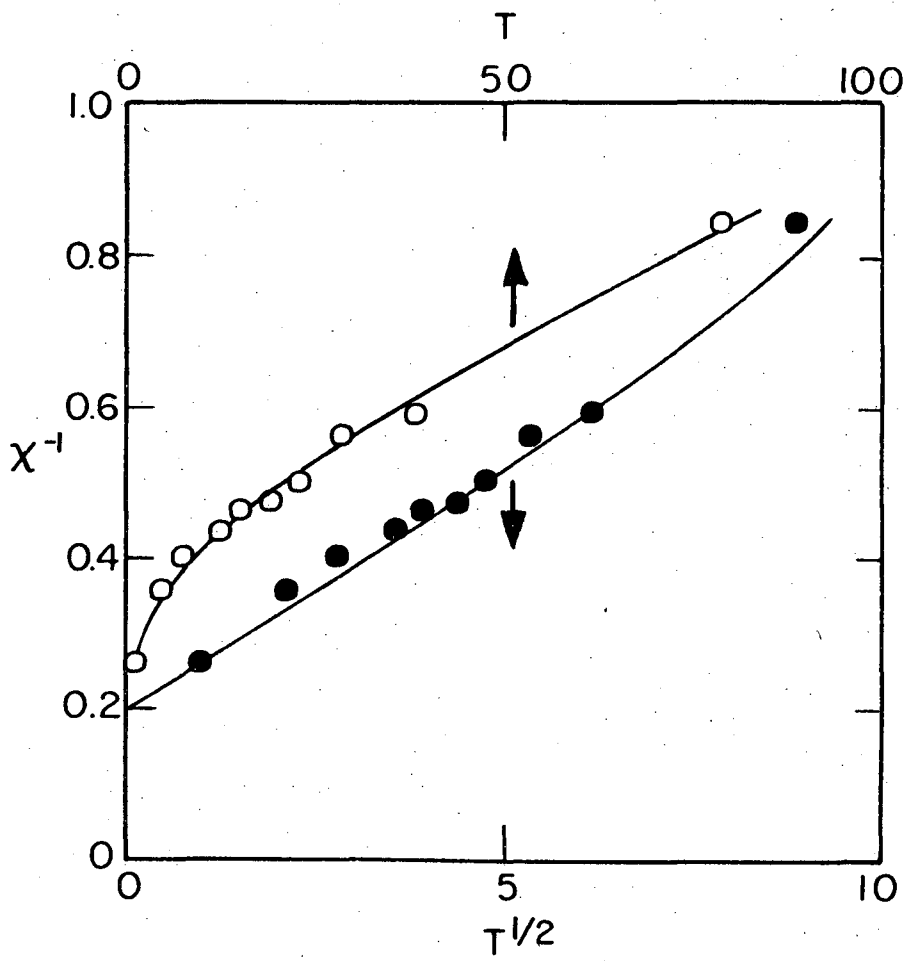

XBL 765-6930

Figure X. 25

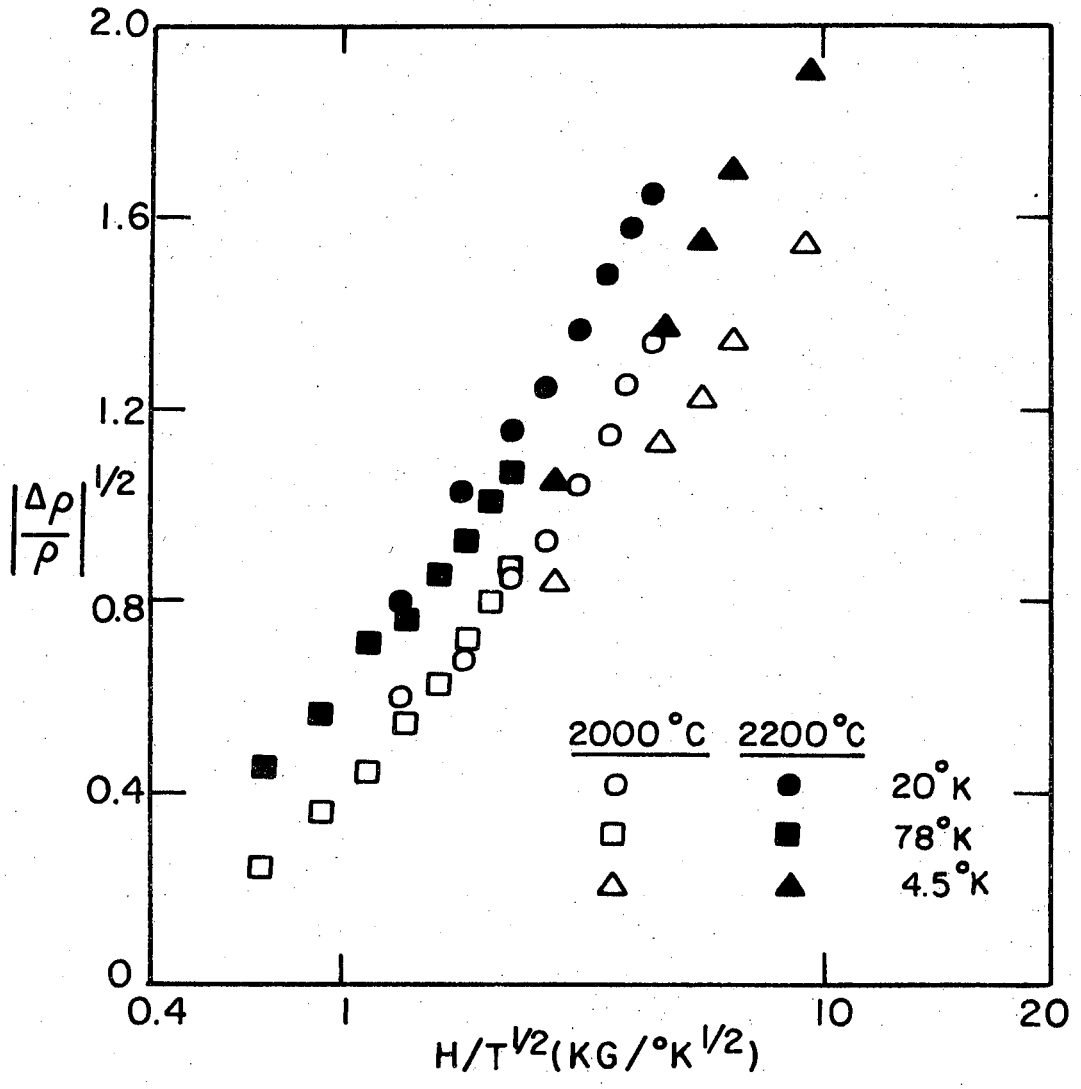

Figure X. 26

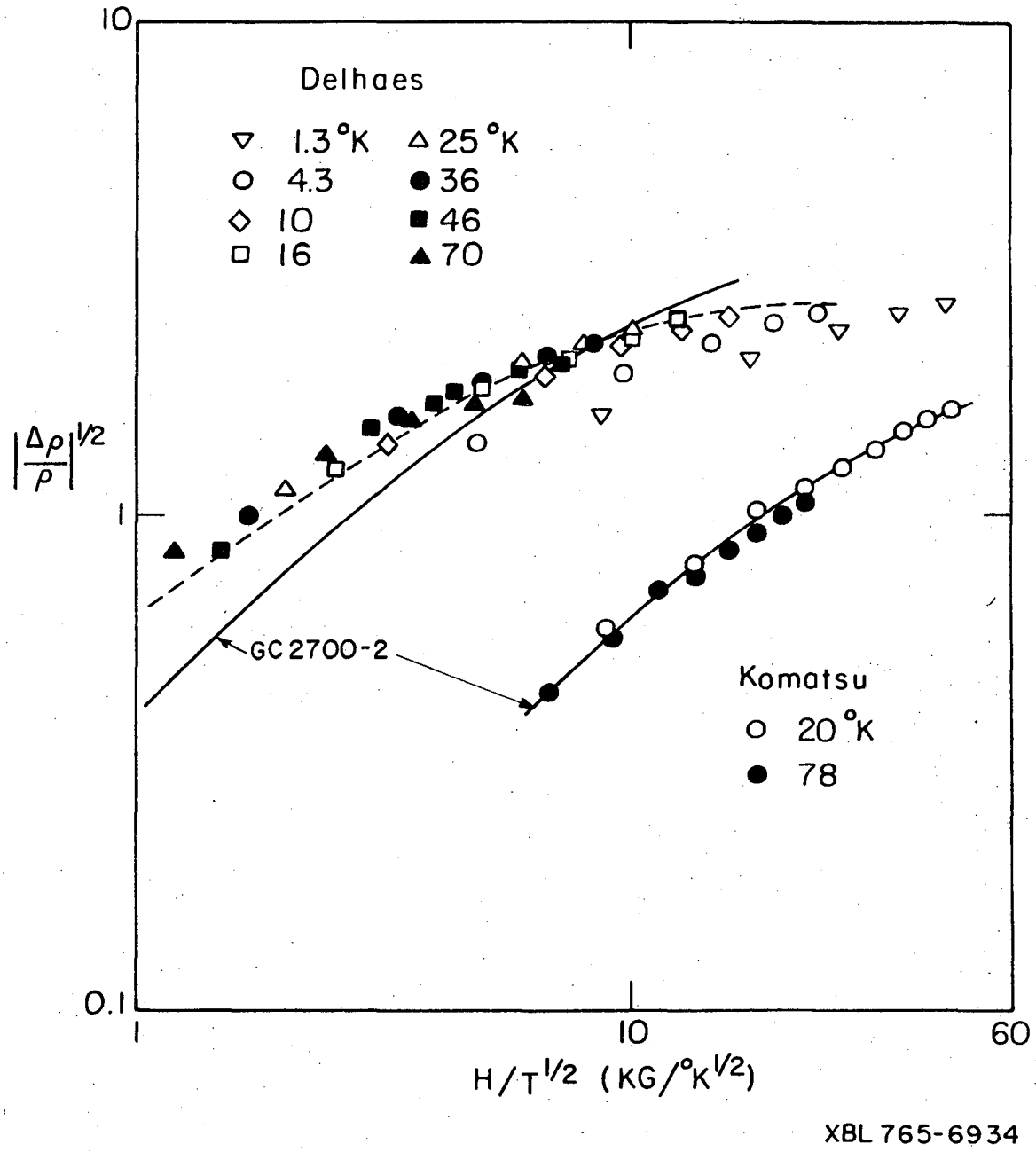
10
1
0.1
Delhaes
1.3 °K
25 °K
4.3
36
10
46
16
70
$\left|\frac{\Delta\rho}{\rho}\right|^{1/2}$
GC 2700-2
Komatsu
20 °K
78
1
10
60
$H/T^{1/2}$ (KG/°K$^{1/2}$)
XBL 765-6934

Figure X. 27

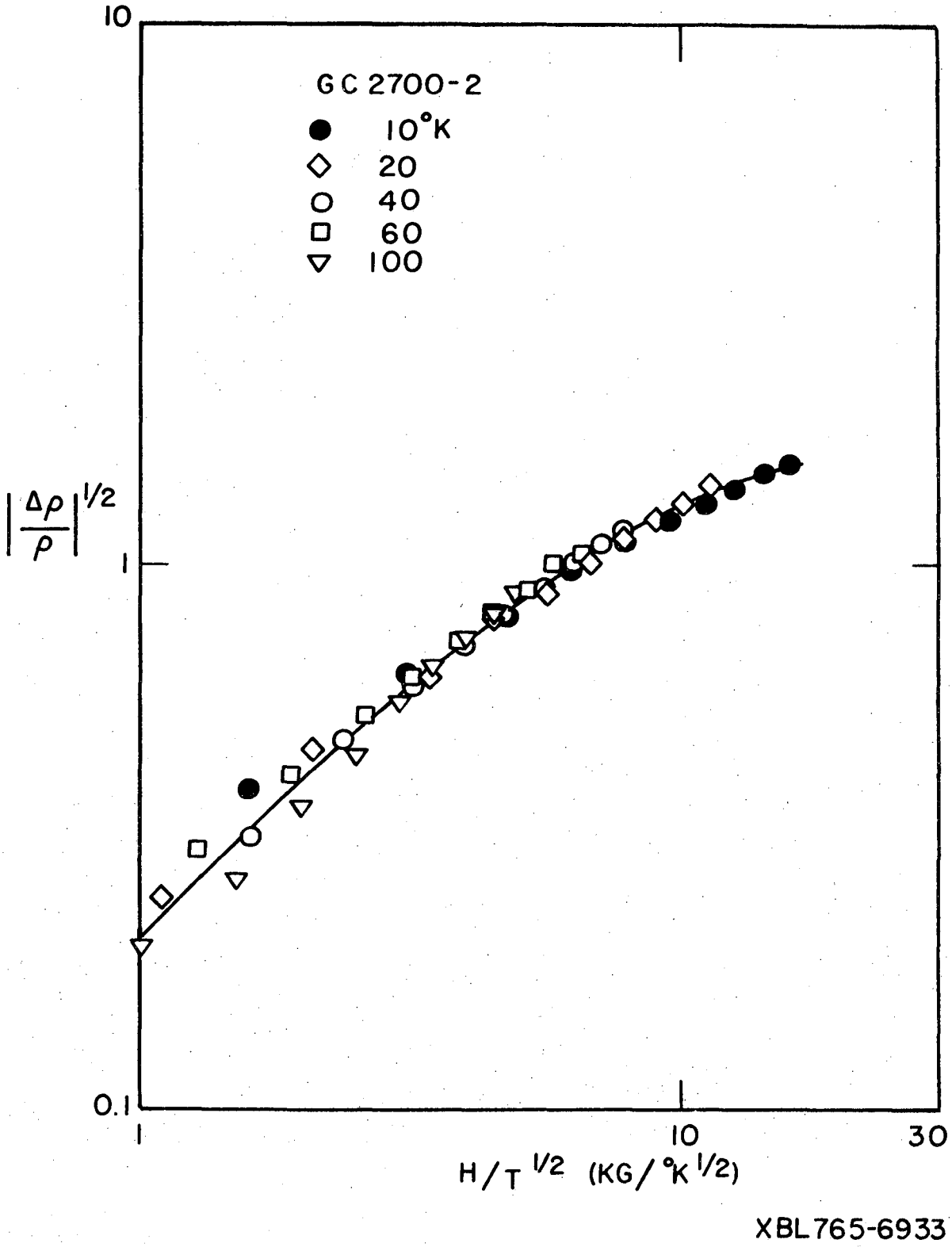

Figure X. 28

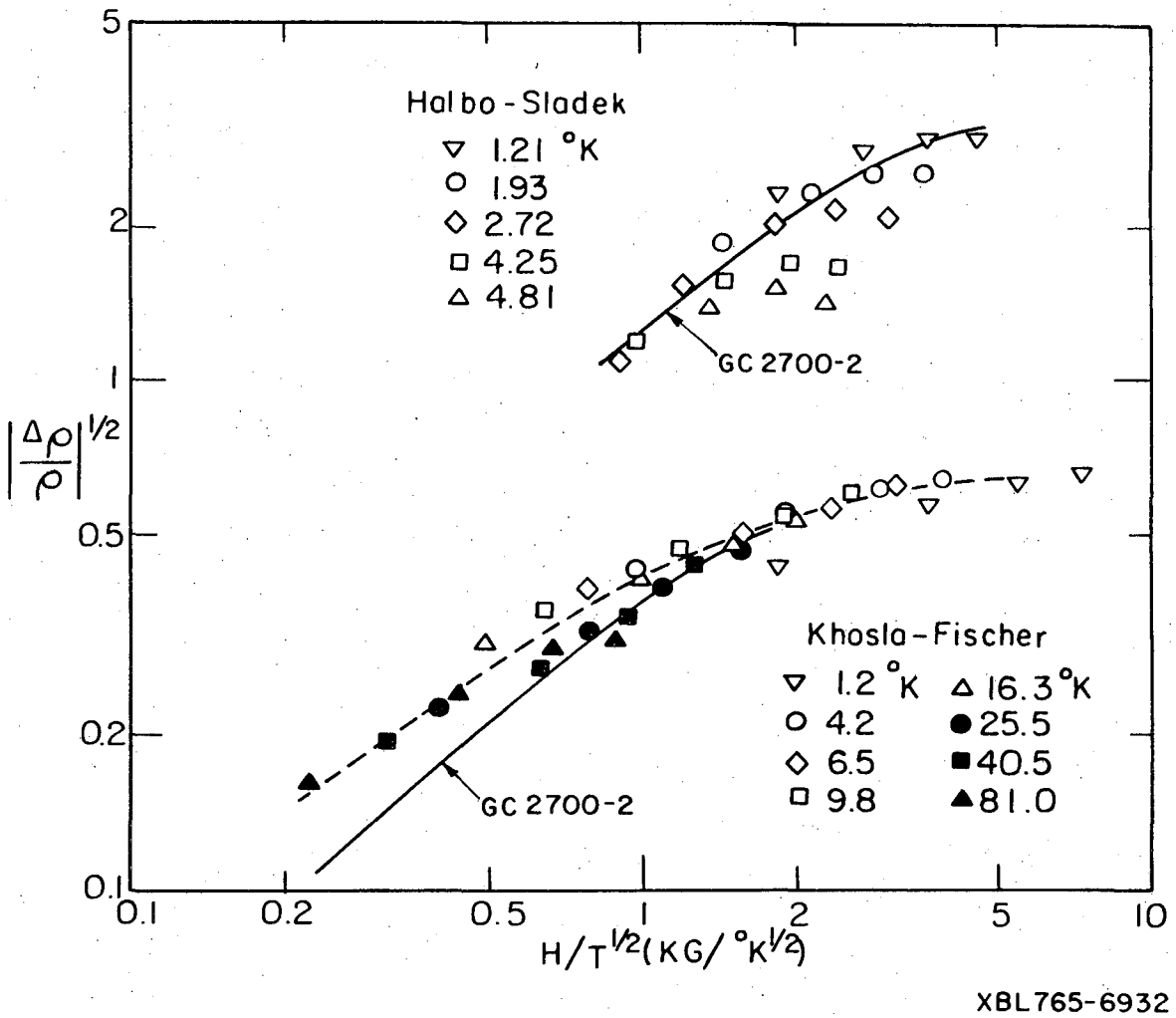
Halbo-Sladek
1.21 °K
1.93
2.72
4.25
4.81
GC 2700-2
Khosla-Fischer
1.2 °K
4.2
6.5
9.8
16.3 °K
25.5
40.5
81.0
GC 2700-2
$\left|\frac{\Delta\rho}{\rho}\right|^{1/2}$
$H/T^{1/2}$ (KG/ °K$^{1/2}$)
0.1
0.2
0.5
1
2
5
10
XBL765-6932

Figure X. 29

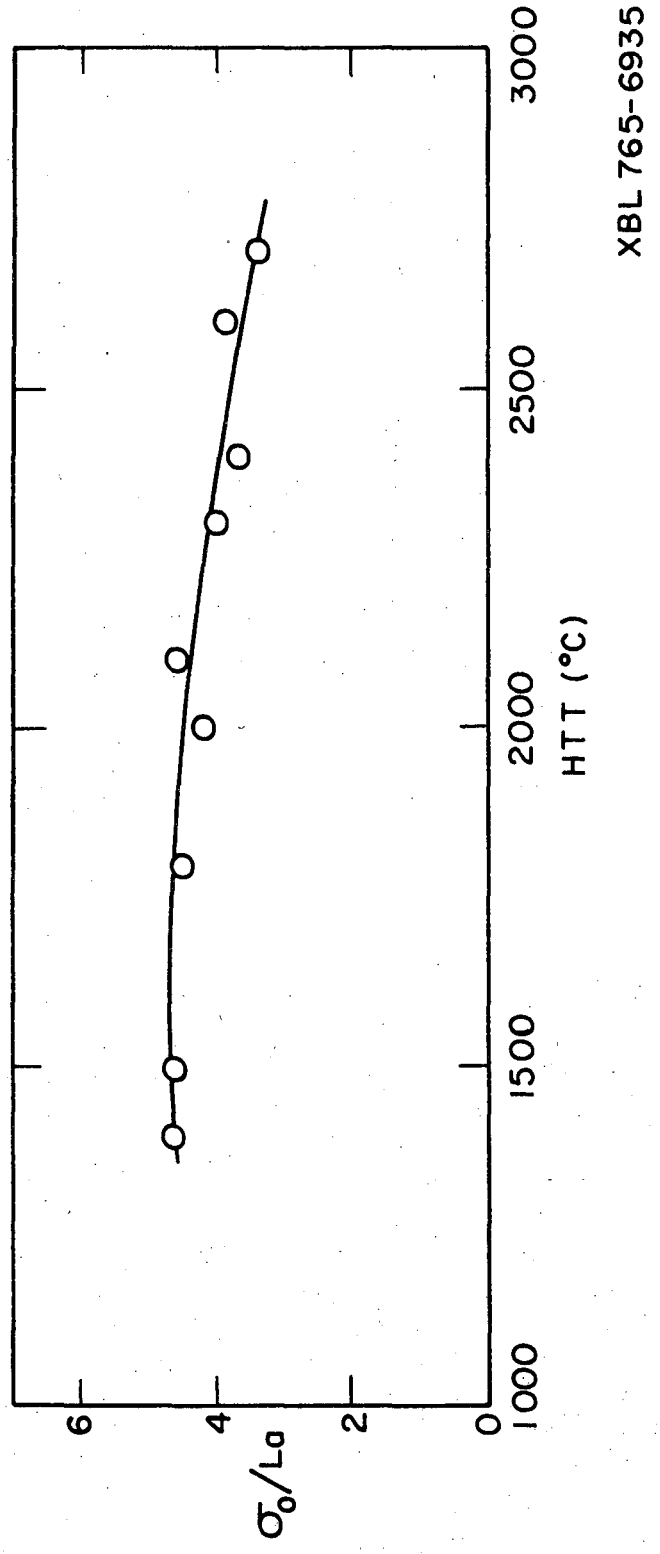

Figure X. 30

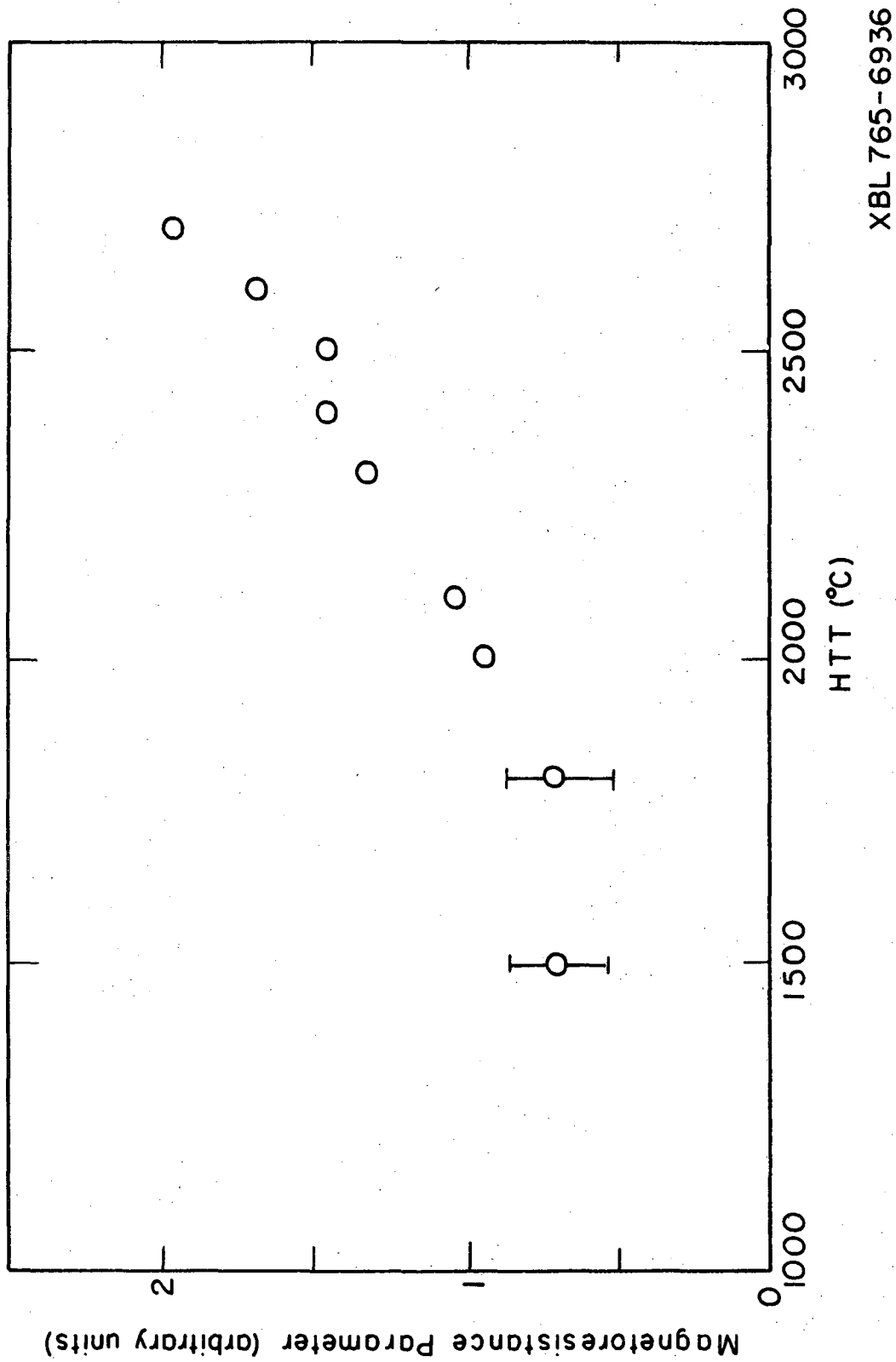
Magnetoresistance Parameter (arbitrary units)
0
1
2
1000
1500
2000
2500
3000
HTT (°C)
XBL 765-6936

Figure X. 31

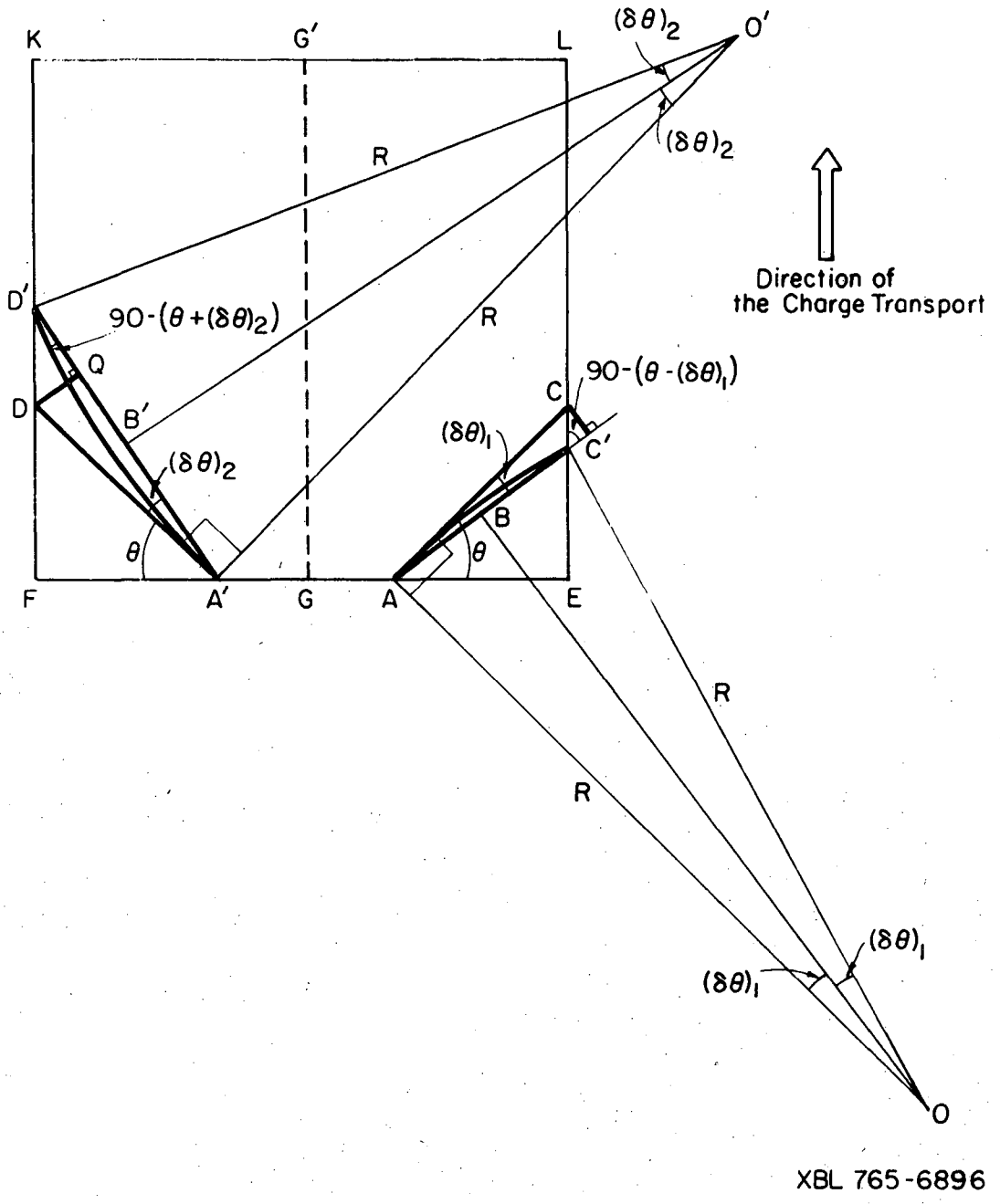

Figure A. II.1

TECHNICAL INFORMATION DIVISION
LAWRENCE BERKELEY LABORATORY
UNIVERSITY OF CALIFORNIA
BERKELEY, CALIFORNIA 94720